RADIOISOTOPE-POWERED PARALLEL ELECTRON LITHOGRAPHY: APPLICATIONS TO SOLAR CELLS, THERMO-OPTO MECHANICAL EXCITATION, INERTIAL SENSORS

A Dissertation

Presented to the Faculty of the Graduate School

of Cornell University

In Partial Fulfillment of the Requirements for the Degree of

Doctor of Philosophy

by

Yuerui Lu

August 2012

RADIOISOTOPE-POWERED PARALLEL ELECTRON LITHOGRAPHY: APPLICATIONS TO SOLAR CELLS, THERMO-OPTO MECHANICAL EXCITATION, INERTIAL SENSORS

Yuerui Lu, Ph. D.

Cornell University 2012

This thesis presents a new potentially low-cost massively parallel electron lithography system, which we term as RadioIsotope-powered Parallel Electron Lithography (RIPEL). We demonstrate its applications to solar cells, thermo-opto-mechanical excitation, inertial sensors, micro-speakers, ultrasonic mechanical DNA sensors. RIPEL utilizes the spontaneously emitted high-energy electrons from beta-emitting radioisotope thin films to parallel expose electron sensitive resist on the wafer, through a nano-stenciled mask that is placed in proximity to the wafer. This approach enables massively parallel e-beam lithography, with the possibility to expose very large areas concurrently as the source of electrons can be made very large. This method potentially eliminates the need for vacuum systems and the electron focusing column as needed in the existing electron beam lithography systems because the electrons emitted are not focused and are emitted close enough to the substrate. This technology will greatly simplify the overall electron lithographic system and reduce the cost of deep-sub nanometer lithography.

RIPEL has been demonstrated to show promising applications to various fields, including solar energy harvesting, photonic crystal based NEMS and inertial sensors. Ordered nanostructure arrays, with large-area controllable spacing, orientation and size,

are promising for high-efficiency solar cells, due to the strongly enhanced light trapping, high carrier collection efficiency and potential low cost. Available top-down lithography approaches to fabricate large-area ordered nanostructure arrays are challenging due to the requirement of both high resolution and high throughput. We have used RIPEL to fabricate ordered silicon nano-conical-frustum array structures, leading to high-efficiency (up to 10.8%) thin-film (5 μm thick) solar cells. Furthermore, these photonic crystal nano-structure arrays have been integrated onto a thin membrane, enabling high-efficiency opto-thermo-mechanical remote excitation for MEMS systems. The membrane structure has been used for an optically excited micro-speaker and optically transduced mass sensor. The same structure demonstrates an ultra-low threshold for chaotic motion due to a very large air-damping, which is due to the large effective surface area. RIPEL has also been used to fabricate inertial sensors, which show small device variations due to the high manufacturing precision of RIPEL system.

BIOGRAPHICAL SKETCH

Yuerui Lu received his B.S. degree in Applied Physics from the University of Science and Technology of China, P. R. China in 2004. He will receive his Ph.D. degree in Electrical and Computer Engineering from Cornell University in 2012. During his Ph.D. studies, he focused on high-throughput nano-lithography system for nano-scale device precise manufacturing, NEMS (Nano Electro-Mechanical System) bio-sensing and actuation as well as solar energy harvesting with nano-structured thin film.

ACKNOWLEDGMENTS

First of all, I would like to thank my advisor Professor Amit Lal. His experience and broad vision helped develop the directions of this project. His careful guidance and warm encouragement played an important role in helping me to pass all the difficult stages.

Also, I would like to thank the rest of my committee members. Their criticism, evaluation and encouragement helped me significantly to solve problems better and improve the thesis. Moreover, I would like to thank all my current and previous course instructors. They gave me various instructions on how to learn knowledge and how to develop the abilities to solve problems. These knowledge and abilities are fundamental to my Ph.D. research work.

Next, I would like to thank my lab mates from *Sonic*MEMS laboratory: Serhan Ardanuc, Manoj Pandey, Kwame Amponsah, Yue Shi, Hadi Hosseinzadegan, Sarvani Piratla, Po-Cheng Chen, Jason Thomas Hoople, Ved Vishwas Gund, June Ho Hwang, Sachin Prakash Nadig, Justin C Kuo, Kyu Jun Cho and former group members Hengky Chandrahalim, Norimasa Yoshimizu, Alper Bozkurt, Steven Tin, Abhishek Ramkumar, Janet Shen, Siva Prasad. They gave me very useful training, collaboration, discussion and so on. I really appreciate the time living and working with them. And I would like to acknowledge our collaborators outside of *Sonic*MEMS lab. Moreover, I need to thank all the staff members from CNF and NBTC. They gave me nice trainings and good suggestion to improve my fabrication processes. I would like to thank our funding agencies, DARPA MTO and NSF, for their financial support.

I am grateful to all my friends, for their warm encouragement and great support. Finally and importantly, I would like to thank my beloved family for the great and long-

term support.

TABLE OF CONTENTS

LIST OF FIGURES

LIST OF TABLES

CHAPTER 1

INTRODUCTION

1.1 History of lithography

Lithography is a method to create a pattern image using chemical processes. It was first invented by Alois Senefelder in Bohemia in 1796, using a smooth piece of limestone (the name "lithography" means stone in the ancient Greek) to print ink-based image onto the surface of another substrate [1]. Lithography was used to print text or artwork onto paper or other suitable materials, in the beginning of its development. So this is the original version of contact lithography or imprint lithography.

In the 19th century, tin cans were popular packaging materials and transfer technologies were required to print on the tin. In 1843, Richard March Hoe invented rotary printing press, using a metal cylinder for press instead of a flat stone. In 1875 in England, Robert Barclay created the first rotary offset lithographic printing press [1]. The offset cylinder was covered with specially treated cardboard to transfer the printed image.

Figure 1.1: Lithography: stone and mirror-image print of a map using lithography [2].

Later, rubber was used to replace the cardboard to cover the offset cylinder, and rubber is still the most commonly used material.

In the beginning of 20th century, many lithographic firms went out of business [3], including Ira Washington Rubel of New Jersey in 1901, Potter Press Printing Company in New York in 1903, Rubel Offset Press in San Francisco in 1907, and so on. Compared to other printing methods, offset printing is best suited for cost-effectively producing large volumes of posters, maps, books, and newspapers.

In mid-20th-century, photolithography [4] became a commonly used method in semiconductor micro-fabrication. Photolithography uses light to transfer a geometric pattern from a photo-mask to a light-sensitive chemical photo-resist on the substrate. Photolithography has played a very important role in the development of semiconductor technology, which enables the integration of large numbers of micro-/nano-scale transistors for integrated circuits (ICs), and other chip based technologies such as micro-electro-mechanical systems (MEMS) devices onto a small chip.

1.2 Photolithography

1.2.1 Basic photolithography procedures

In optical lithography [4], the photons are delivered to the photo-resist by projecting from a distant lamp source passing through an optical mask with opaque and clear sections on a glass plate. The delivered photons will modify photo-resist polymer, by changing its chemical reactivity with a chemical developer. The basic procedure of photolithography combines following several steps in sequence (Fig. 1.2).

Photo-resist Coating: A photo-resist is a light-sensitive material used in photolithography to form a patterned coating on a surface. Photoresists are classified into two groups: positive resists and negative resists. For a positive resist, the portion that is exposed to light becomes soluble to a special solution, called "developer" and the unexposed portion remains insoluble. For a negative resist, the light-exposed portion becomes insoluble to the photoresist developer and the unexposed portion is dissolved by the photoresist developer. Before photo-resist coating, the wafer will be cleaned to remove the organic or inorganic contaminations present on the wafer surface. After

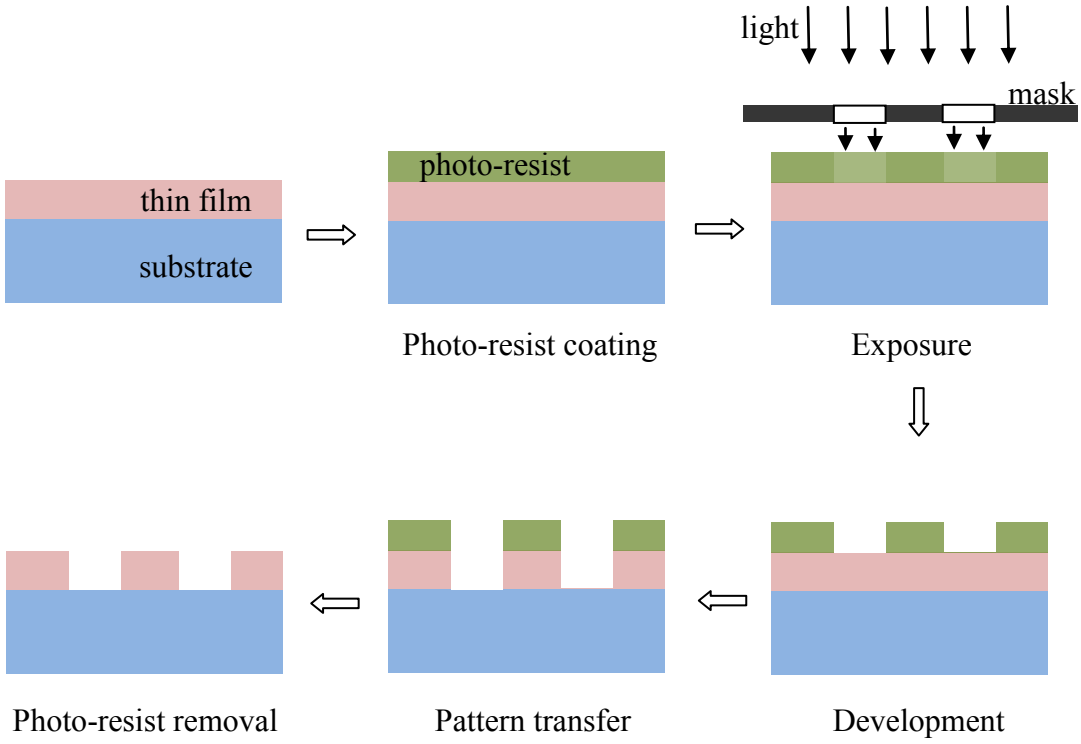

Figure 1.2: Schematic plots for the basis procedures of photolithography.

cleaning, a liquid solution of photo-resist is dispensed onto the wafer, and the wafer is spun rapidly at to produce a uniform film layer. The thickness of the film is a function

of the spin speed and time, which normally ranges from 1000 to 5000 rpm for 30 to 60 seconds, and produces a layer between 3 and 0.5 micrometers thick. The uniformity of the film is high, with a roughness of around 5 to 10 nm. Finally, the photoresist-coated wafer is then prebaked, typically at 90 to 115 ℃ for 30 to 90 seconds on a hotplate, to drive off excess photoresist solvent.

Exposure and Development: After prebaking, the photoresist is exposed by projecting intense light photons from a distant lamp source passing through an optical mask. Optical lithography typically uses ultraviolet light. A photo-mask typically consists of transparent fused silica blanks covered with a pattern defined with a chrome metal absorbing film. The opaque plate with transparencies allows light to shine through in a defined pattern. Normally, photo-masks are used at optical wavelengths of 193 nm, 248 nm, and 365 nm, depending on the requirements. Normally, after exposure, a post bake process for the photoresist, typically at 90 to 115 ^{o}C for 30 to 120 seconds, is performed to trigger the “exposure” reaction (creating acid, making the positive resist polymer soluble in the basic developer). Then, a special solution, called "developer", will be used to remove the exposed (or unexposed) portion of the positive (or negative) photoresist. A developing time normally ranges from 30 to 120 seconds. Metal-ion-free developers such as tetramethylammonium hydroxide (TMAH) are commonly used.

Pattern Transfer: After exposure and development, the desired pattern is formed on the photoresist layer. This pattern needs to be transferred to the wafer substrate. For micro-fabrication, two techniques are commonly used for pattern transfer: etching and lift off. Etching is an important module used in micro-fabrication to chemically remove layers from the surface of a wafer. For many etch steps, part of the wafer is protected

from the etchant by a "masking" material, such as photoresist that is patterned using photolithography. Etching can be divided into two fundamental types: wet etching and dry etching, depending on the types of etchants used. Wet etching uses liquid-phase ("wet") etchants. For instance, buffered hydrofluoric acid (BHF) is used commonly to etch silicon dioxide over a silicon substrate. Normally, liquid-phase etching undercuts the masking layer and forms sloping sidewalls. Dry etching uses plasma-phase ("dry") etchants. For example, SF_6/O_2 plasma can be used to etch silicon. Dry etching can be anisotropic, exhibiting a much larger downward etch rate than its lateral undercut rate. The sharp and well-controlled features are greatly preferred by modern micro-machining processes. When pattern is transferred by etching, the remaining photoresist is no longer needed and it must be removed from the substrate. Resist removal usually requires wet etching by a liquid "resist stripper", or alternatively, dry etching by oxygen plasma to oxidize it.

Lift-off process is another important method in micro-machining technology to create target patterns onto substrate surface, using a sacrificial material such as photoresist. It is an additive pattern transfer technique as opposed to etching. For lift-off, firstly, a sacrificial layer, such as photoresist, is deposited on the surface of the substrate and an inverse pattern is created in this layer. Then the target material is directionally deposited onto the wafer over the whole area. The target material can reach the surface of the substrate in the area where the sacrificial layer is etched, otherwise the target material will stay on the top of the sacrificial layer. Then the sacrificial layer can be washed away by a special solvent solution and the target material on the top is lifted-off and washed together. After the lift-off, only the target material that has a direct contact with the

substrate remains.

1.2.2 Photolithography resolution

Critical dimension (CD) is a very important parameter for photolithography and it is a function of the wavelength of the light used in the projection system. The CD value of a projection system can be given approximately by [4]:

$$CD = k_1 \cdot \frac{\lambda}{NA} \tag{1.1}$$

Where λ is the wavelength of the light used, k_1 is a coefficient that encapsulates process-related factors (commonly called k_1 factor, typically equals 0.4 for production) and NA is the numerical aperture of the lens as seen from the wafer. According above equation, the CD value can be decreased by using smaller light wavelength, and increasing the numerical aperture (higher numerical aperture, tighter focused beam and smaller spot size). However, there is a trade-off between the CD value and another important parameter of the system, depth of focus. The depth of focus determines the depth of the topography and the thickness of the photoresist. The depth of focus (D_F) is given by [4]:

$$D_F = k_2 \cdot \frac{\lambda}{(NA)^2} \tag{1.2}$$

where k_2 is another process-related coefficient.

1.2.3 Light sources for photolithography

In the early stage of photolithography, single spectral line that was selected from ultraviolet light from gas-discharge lamps by filters, was used as the light source. From the early 1960s through the mid-1980s, spectral lines at 436 nm ("g-line"), 405 nm ("h-line") and 365 nm ("i-line") from Hg lamps had been commonly used in photolithography. In order to produce denser and faster chips, higher resolution photolithography is required for semiconductor industry requiring smaller wavelengths. Excimer laser lithography, was created and commonly used since 1980s. Krypton fluoride laser at 248-nm wavelength and the argon fluoride laser at 193-nm wavelength were normally used in the excimer laser lithography system. Excimer laser lithography [5] has played an important role in the continued advance of Moore's Law, enabling photolithography resolution to reduce from 500 nanometers in 1990 to 45 nanometers and below in 2010. In order to achieve high photolithography resolution below 50 nm, 193 nm ArF excimer laser and liquid immersion techniques were used, which is termed immersion lithography. It typically uses ultra-pure, deionized water, which provides for a refractive index above that of the usual air gap between the lens and the wafer surface, enabling the use of optics with numerical apertures exceeding 1.0, and decreasing effective wavelength λ' ($\lambda' = \lambda / \nu$), where λ is light wavelength in vacuum and ν is the refractive index of the deionized water.

1.3 Available and in-development nanolithography technologies

Typically, features smaller than 10 micrometers are considered to be made by microlithography, and features smaller than 100 nanometers are considered to be made by nanolithography. Optical lithography, is capable of producing sub-100 nm features, by

using very short wavelengths, such as 193 nm, and liquid immersion techniques. Here, other available nanolithography technologies will be discussed.

1.3.1 Electron beam lithography

Electron beam lithography uses a beam of high-energy electrons in a patterned fashion to expose electron-sensitive resist on a substrate. In quantum mechanics, the concept of matter waves or de Broglie waves reflects the wave-particle duality of matter. The wavelength (λ_e) of high-energy electron beam can be given by the de Broglie equations [6],

$$\lambda_e = h / \sqrt{2mE} \tag{1.3}$$

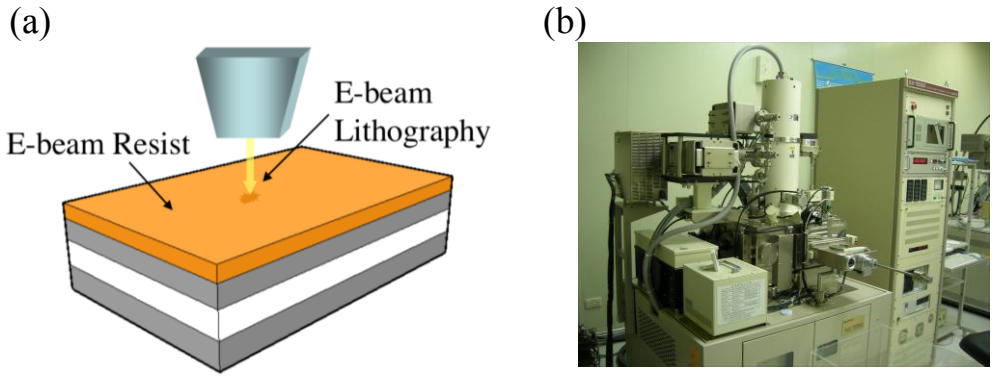

Figure 1.3: (a) Schematic plots for the raster scanning exposure mechanism of electron beam lithography. (b) A photo image of electron beam lithography system. Images are cited from web.

where *h* is Planck's constant, *m* is electron mass and *E* is the energy of the electron beam. For example, for an electron beam with energy of 15 keV, its wavelength is calculated to

be 0.01 nm. Therefore, electron beam lithography can beat the diffraction limit of light easily. For electron beam lithography, its resolution is limited by electron scattering in resist. Sub-20 nanometer resolution has been demonstrated by electron lithography. Due to its serial exposure mechanism, the key limitation of electron beam lithography is its ultralow throughput due to its raster scanning (Fig. 1.3). For example, it will take a very long time to expose an entire four inch silicon wafer, depending on the pattern density. The system is also expensive. For example, the charge rate of electron beam lithography system is around $250 per hour (academic rate in 2012), in Cornell Nanofabrication facility. Therefore, electron beam lithography has been limited in mask-making for photolithography, low-volume production of semiconductor components, and in research and development.

The exposure time T over a given area A for a constant dose D can be calculated by the following formula [7]:

$$T = \frac{D \cdot A}{I} \tag{1.4}$$

where I is the beam current.

For example, assuming an exposure area of 1 cm^2, a dose of 1000 $\mu C/cm^2$, and a beam current of 1 nA, the resulting minimum write time would be 10^6 seconds (about 12 days). Shorter times can be achieved by using lower dose e-beam resists, but some other values might be trade off, such as resolution.

Alternative approaches for electron lithography are SCALPEL [8] at Lucent Technologies and PREVAIL [9] at IBM brought projection EBL within the range of use in integrated circuit production, which uses the projection of sections “subfields” (~1 mm^2 size subfields, small compared to the size of a wafer, but large compared to pattern

features) on a four times mask onto a wafer, followed by accurate stitching of the subfields to complete the entire chip pattern. However, both SCALPEL and PREVAIL must use the step-and-scan writing strategy due to size limitation from the shaped square beam (2 mm), which is still two orders magnitude less than the pattern subfield size. Fundamentally, these technologies are still not wafer-scale massively parallel-like optical lithography, and their throughputs are still too low for commercialization.

1.3.2 X-ray lithography

X-ray lithography (Fig. 1.4) uses X-rays (photons of very high energy from 120 eV to 120 keV) to transfer a geometric pattern from a mask to a light-sensitive chemical

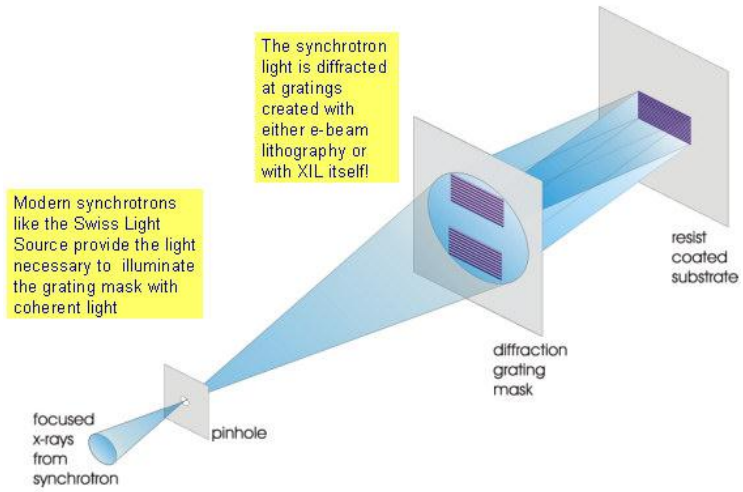

Figure 1.4: Schematic plot for the set-up of a conventional X-ray lithography. Image is cited from the website of Laboratory for Micro- and Nanotechnology.

photoresist on the substrate [10]. X-rays have short wavelengths (below 1 nm), allowing smaller feature sizes. In order to minimize the diffraction effect, the mask is placed in

proximity of a resist-coated substrate. The mask consists of an X-ray absorber, typically of gold or tungsten, on a membrane that is transparent to X-rays, such as diamond or silicon carbide. The pattern on the mask is written by electron beam lithography.

X-rays can generate secondary electrons and Auger electrons. Secondary electrons have energies of 25 eV or less, while Auger electrons have energies of hundreds of electron volts. The image exposure contrast *(max-min)/(max+min)*, the sidewall roughness and slopes can be influenced by these secondary electrons as they can travel few micrometers in the area between the mask and the resist, depending on exposure X-ray energy [11]. Moreover, X-ray scattering within the photoresist limits the resolution [10].

1.3.3 Extreme ultraviolet lithography

Extreme ultraviolet (EUV) lithography (Fig. 1.5) is another advanced under-developing optical lithography technology, using an extreme ultraviolet wavelength, currently expected to be 13.5 nm (photon energy 92 eV). For matter to emit EUV, ionization must take place first. EUV light can only be emitted by electrons which are bound to multi-charged positive ions, such as +3 charged carbon ion (three electrons already removed). It needs much more energy to remove such electrons than to remove typical valence electrons. For example, state-of-the-art 193 nm excimer laser offer intensity [12] of 200 W/cm^2, while the laser for producing EUV-generating plasma requires much more intensity [13], on the order of 1 kW/cm^2. In order to switch from generating 193 nm light to generating EUV light, the power requirement will increase dramatically. As of 2008, with a 120 W source, the developed tools had a throughput of 4 wafers per hour. But in

order to get a 100 WPH throughput, a 3 kW source would be required, which is challenging in the foreseeable future. Another

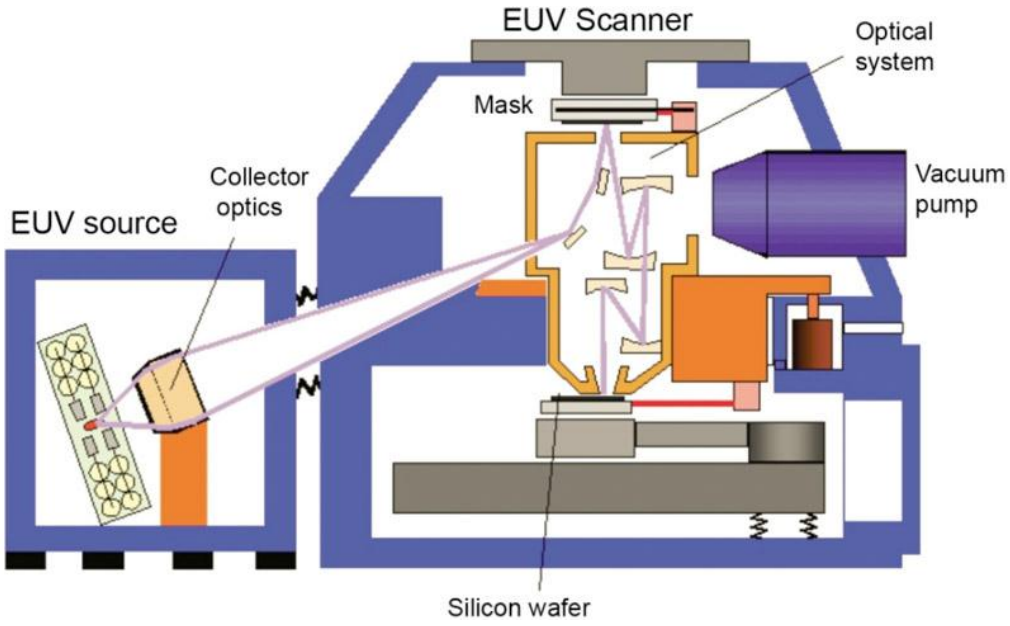

Figure 1.5: EUV lithography tool. Image is cited from website: http://blog.dac.com/post/2012/07/18/Extreme-Ultra-Violet-(EUV)-the-Great-Hope.aspx

challenge of EUV lithography is the specific defect issues, which are attributed to the inherently ionizing energy of EUV radiation. All matter absorbs EUV radiation. Hence, EUV lithography needs to take place in a vacuum. The EUV radiation will lead to ejection of photoelectrons freed from the top resist surface. This could lead to electrostatic discharge or particle contamination as well as the device damage [14-16].

In April 2009, IMEC acknowledged that EUV would not be ready when companies start using 22 nm. In 2010, KLA-Tencor, Global Foundries and Lawrence Berkeley National Labs published a paper together showing the stochastic behavior of EUV-generated secondary electrons in EUV resists [17]. In particular, 32 nm half-pitch trenches showed significant edge roughness, width roughness and critical dimension

(CD) variability [18].

1.3.4 MAPPER maskless nanolithography

MAPPER Lithography [19] is a company developing a mask-less lithography technology based on massively-parallel electron-beam writing with high speed optical data transport for switching the electron beams. In this way optical columns can be

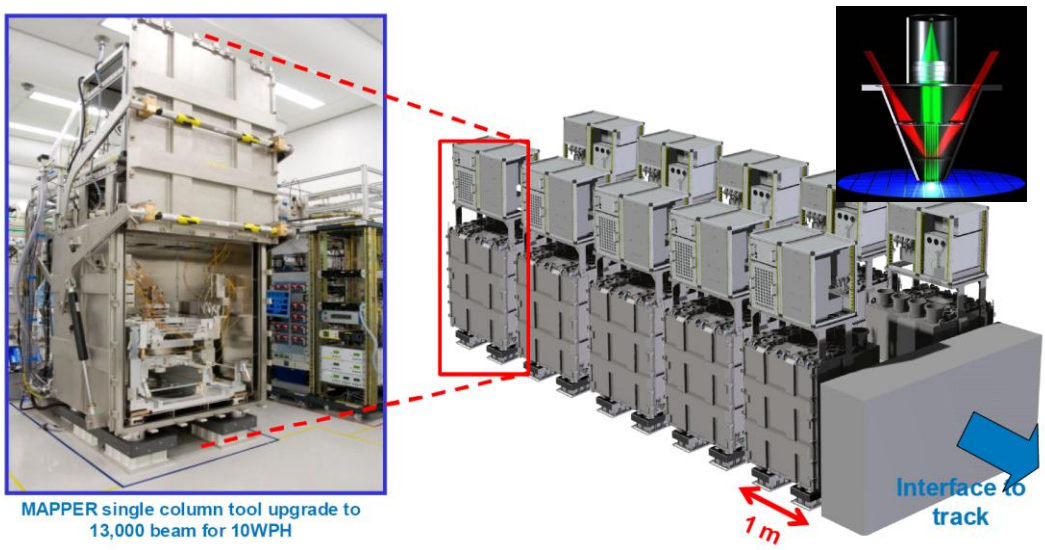

Figure1.6: Photo images of MAPPER's massively parallel electron beam lithography. Inset shows its schematic of concept [19].

made with a throughput of 10-20 wafers per hour. By clustering several of these systems together high throughputs can be realized in a small footprint. This enables a highly cost-competitive alternative to double patterning and EUV alternatives. The goal of MAPPER is to scale the current system to a 10 WPH machine and finally it can be used in a cluster configuration to enable 100 WPH throughputs. Each beam gun [19] has a current of 0.3 nA and acceleration voltage of 5 kV.

1.3.5 Nano-imprint lithography

Nano-imprint lithography (NIL) is a method of fabricating nanometer scale patterns by mechanical deformation of imprint resist and subsequent processes (Fig. 1.7). Thermoplastic NIL and photo NIL are the two most important types of NIL. In a standard thermoplastic NIL process [20], a thin layer of thermoplastic polymer imprint

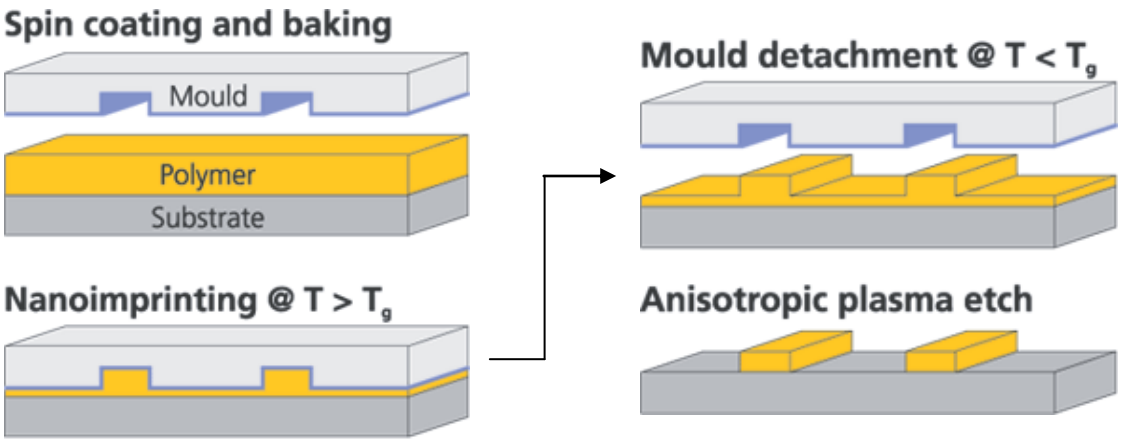

Figure 1.7: Schematic plot for the process flow of a Nano-Imprint Lithography. Image is cited from the website of Micro Resist Technology.

resist is spin coated onto the wafer. Then a mold with predefined topological patterns, is brought into contact with the wafer under certain pressure. When heated up above the glass transition temperature, the polymer resist film will be softened and the patterns on the mold are pressed into film. After being cooled down, the mold is separated from the wafer and the patterns are left on the resist film. In a standard photo NIL [21], a photo (UV) curable liquid resist is used. When the transparent mold and the substrate are pressed together, UV light is used to shine through the mold and cure the resist to turn it to solid. After that, mold will be slowly separated from the resist.

A key merit of NIL is its simplicity, leading to low cost. There is no need for complex optics or high-energy radiation sources in a nano-imprint tool. Moreover, NIL is free of diffraction effect limitation, resulting in high resolution down to sub-10 nm. However, the main concerns for NIL are overlay, defects, template patterning and template wear, since the mask needs to be in contact with the resist.

1.3.6 Self-assembly lithography

Self-assembly lithography [22] is a bottom-up method to fabricate nanoscale patterns on substrate. This self-assembly based nanolithography has the potential to overcome the

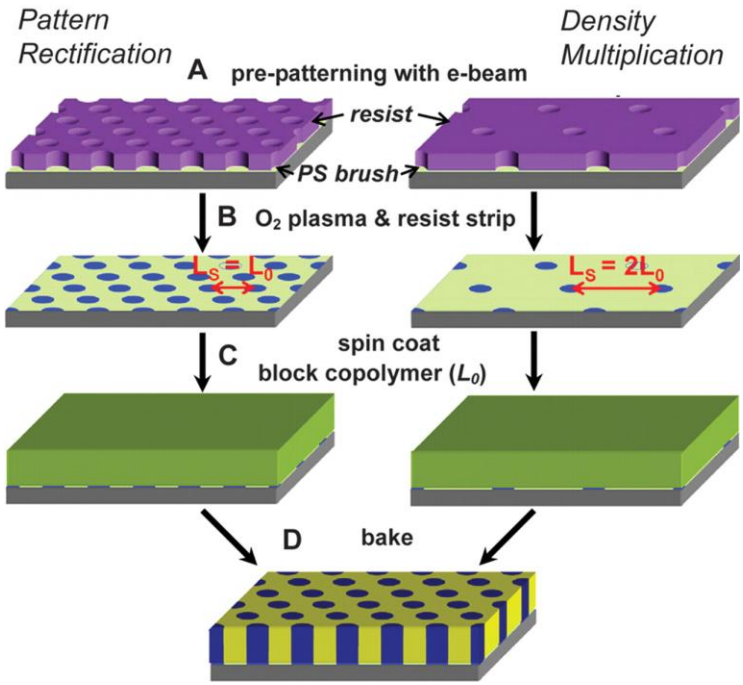

Figure 1.8: Schematic for a directed block copolymer self-assembly lithography [23].

intrinsic resolution limit of conventional photolithography (Fig. 1.8). For example, block

copolymers [23, 24] are self-assembling materials that can form densely packed periodic arrays of nano-dots, nanowires, and interconnected networks. Their characteristic length scales are typically ranging from 5 to 50 nm. This self-assembled morphology of block copolymer thin films can be used as a lithographic mask for large-area, scalable nano-patterning. Currently, challenges need to be addressed. For example, it is still difficult to realize good control on the degree of dimension and orientation as these are controlled by thermally stochastic processes. Also, the line edge roughness of the pattern is often an issue.

1.3.7 Radioisotope-powered parallel electron lithography

We designed and developed a new low-cost massively parallel electron lithography system, called radioisotope-powered parallel electron lithography. It utilizes the spontaneously emitted high-energy electrons from beta-emitting radioisotope thin films to parallel expose nano-stenciled mask that is placed in proximity to electron sensitive resist on the wafer. This approach enables massively parallel e-beam lithography, with possibly no theoretical limit on the concurrently exposed surface area. This method potentially eliminates the need for vacuum systems and the electron focusing column as needed in the existing electron beam lithography systems because the electrons emitted are not focused and are emitted close enough to the substrate such that the scattering with air molecules is insignificant for the total flux of electrons. This will greatly simplify the overall lithographic system and reduce the cost of deep-sub nanometer lithography.

1.4 Comparison of lithography techniques

Table 1.1: Comparison of lithography techniques.

Techniques	Resolution	Throughput	Comments	Ref.s
Contact photo-lithography	~ 0.5 μm	Ultra-High	Defect is an issue, due to contact.	[25]
Projection photo-lithography	~0.1- 0.5 μm	High	NA	[26]
Immersion photolithography	< 100 nm	High	resists with high refractive indices.	[27]
E-beam lithography	< 20 nm	Ultra-low	Expensive	[28]
EUV lithography	22 nm~32 nm	High	In development	[13, 18]
X-ray lithography	< 50 nm	High	NA	[11, 30]
Nano-imprint lithography	< 15 nm	High	Defects and mask wear are issues.	[20, 21, 29, 31]
SCALPEL /PREVAIL	20~50 nm	Low	Step-and-exposure mode	[9, 32]
Self-assembly lithography	5 ~ 50 nm	Low	No good control over large area.	[23]
RIPEL	< 20 nm	Potentially high	Vacuum-free, low-cost	[33, 34]

1.5 Organization of thesis

In this thesis, it presents a novel nanolithography system named as RadioIsotope-powered Parallel Electron Lithography (RIPEL) and its applications to solar cells, thermo-opto-mechanical excitation and inertial sensors. Chapter one gives an introduction for lithography, including the history of lithography and the comparison among available and in-development nanolithography technologies. Chapter two to chapter four present our RIPEL lithography system, including simulation (chapter two) and proof-of-concept experimental demonstration (chapter three and four) for RIPEL. Chapter five to chapter eight present RIPEL applications to various fields, including solar energy harvesting (chapter five), photonic crystal based NEMS (chapter six), self-powered ion gauge and ion pump of for potential MEMS packaging (chapter seven), and NEMS inertial sensors (chapter eight).

CHAPTER 2

RADIOISOTOPE-POWERED PARALLEL ELECTRON LITHOGRAPHY MODELING

2.1 Radioisotope-powered parallel electron lithography structure

RadioIsotope-powered Parallel Electron Lithography [33] (RIPEL) utilizes the spontaneously emitted high-energy electrons from beta-emitting radioisotope thin films (such as ^{63}Ni) to parallel expose nano-stenciled mask that is placed in proximity to electron sensitive resist on the wafer. This approach enables massively parallel e- beam lithography, with possibly no theoretical limit on the concurrently exposed surface area. This method potentially eliminates the need for vacuum systems and the

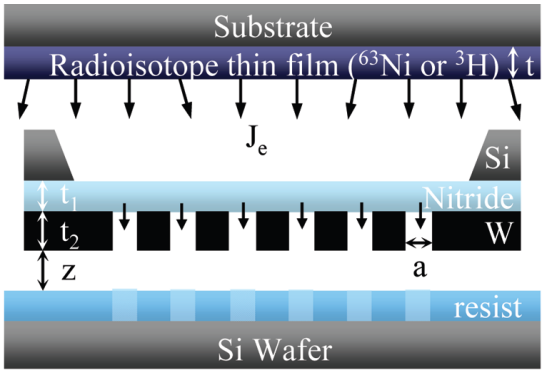

Figure 2.1: Cross section schematic drawing for RIPEL simulation and experimental setting up: a is the width of the line holes in tungsten mask; t is the thickness of the radioisotope thin film source; t_1 is the thickness of the supporting nitride layer; t_2 is the thickness of the tungsten layer needed to fully block particles in the non-hole region; Z is the mask-resist gap; J_e is the current flux density, emitted from the radioisotope thin film source.

electron focusing column as needed in the existing electron beam lithography systems because the electrons emitted are not focused and are emitted close enough to the substrate such that the scattering with air molecules is insignificant for the total flux of electrons. This will greatly simplify the overall lithographic system and reduce the cost of deep-sub nanometer lithography.

2.2 Monte Carlo simulations for RIPEL system

The Monte Carlo electron trajectory simulation method has been extensively applied to electron probe micro- and nano-analysis. Here, we developed our own codes, based on several available Monte Carlo models [35-37], which have been proved to be most accurate.

2.2.1 Fermi beta decay theory

In nuclear physics, beta decay is a type of radioactive decay in which a beta particle (an electron or a positron) is emitted from an atom. There are two types of beta decay: beta minus and beta plus. In the case of beta decay that produces an electron (or a positron) emission, it is referred to as beta minus (or beta plus). Beta decay is mediated by the fundamental weak force. Here we focus on a pure beta-electron emitter that emits no other energetic particles, as often is the case for radiation decay.

From the Fermi theory of beta decay [38], the shape of the electron energy distribution for the allowed transition is given approximately by the expression:

$$N(E) = C(E^2 + 2Em_e c^2)^{1/2}(Q-E)^2(E+m_e c^2)F(Z,E) \qquad (2.1)$$

where c is speed of light, m_e is electron rest mass, Z is the nuclear charge on the daughter

nucleus, E is the kinetic energy of the emitted electrons, Q is the upper bound on the kinetic energy of the electrons. The Fermi function $F(Z,E)$, accounts for the nuclear coulomb interaction that shifts this distribution toward lower energies due to the coulomb attraction between the daughter nucleus and the emitted electron. It is given by [39]:

$$F(Z,E) = 2\pi\left(\frac{Ze^2c}{\hbar}\sqrt{\frac{m_e}{2E}}\right)\Bigg/\left[1-\exp(-2\pi\left(\frac{Ze^2c}{\hbar}\sqrt{\frac{m_e}{2E}}\right)\right] \tag{2.2}$$

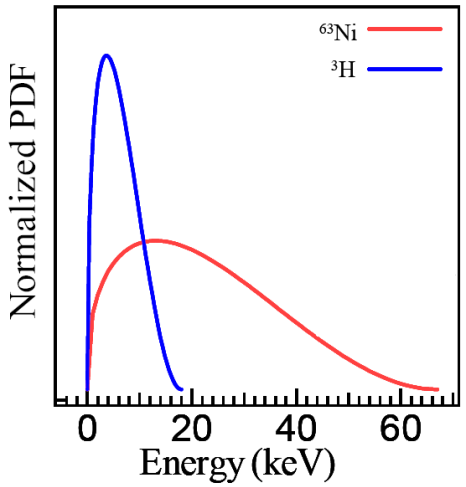

Figure 2.2: The energy distribution Probability Density Function (PDF) of beta particles emitted from nickel radioisotope ^{63}Ni and tritium ^{3}H, calculated from beta decay theory.

2.2.2 Elastic scattering

We used Mott cross section to describe elastic scattering. The Mott cross section describes the scattering of a high energy electron beam from an atomic nucleus-sized positively charged point in space. The Mott scattering separates the two spin states of an electron beam by scattering the beam off the Coulomb field of heavy atoms. In lay terms,

Mott Scattering is similar to Rutherford scattering but electrons are used instead of Alpha particles as they have much lower mass [40]. The differential Mott cross section of any chemical element, such as Au, is a function of the incident angle and the energy of the electron (Fig. 2.3).

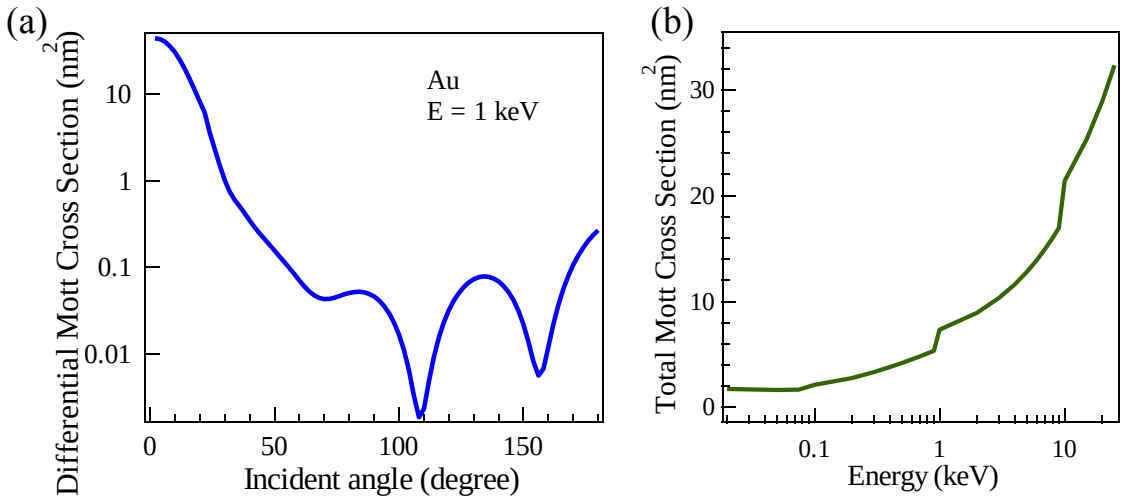

Figure 2.3: (a) Calculated Differential Mott Cross Section of element Au, as a function of the Incident Angle of the electron (at energy 1 keV). (b) Calculated Total Mott Cross Section of element Au, as a function of the incident electron energy.

For a compound material, with n elements, its total elastic mean free path (EMFP) λ_e is determined by:

$$\lambda_e^{-1}(E) = \rho N_0 \sum_{i=1}^{n} \frac{C_i \sigma_e^i(E)}{A_i} \tag{2.3}$$

Where E is the kinetic energy of the incident electron, ρ is the density of the region, N_0 is the Avogadro's constant, A_i, C_i are the atomic weight and number fraction of element i, respectively. The Mott cross section value σ_e^i of chemical element i is

determined using the pre-calculated and tabulated value [41, 42].

2.2.3 Inelastic scattering

Inelastic scattering is another fundamental scattering process in which the kinetic energy of an incident particle is not conserved, in contrast to elastic scattering. In an inelastic scattering process, some of the energy of the incident particle is lost or gained. During an inelastic scattering process, secondary electrons could be produced. Some of these secondary electrons might have high enough energy to further generate more secondary electrons, leading to a cascade process. When an electron is the incident particle, the probability of inelastic scattering, depending on the energy of the incident electron, is usually smaller than that of elastic scattering.

We used dielectric response theory to describe inelastic scattering. The electron inelastic differential cross section can be expressed by [43]:

$$\frac{d^2\sigma}{d(\hbar\omega)dq} = \frac{1}{\pi a_0 E}\,\mathrm{Im}[-1/\varepsilon(q,\omega)]\frac{1}{q} \tag{2.4}$$

Where a_0 is the Bohr radius, $\hbar\omega$ is the energy loss, $\hbar q$ is the moment transfer, E is the kinetic energy of the incident electron and $\varepsilon(q,\omega)$ is the dielectric response function.

The stopping power and the inelastic mean free path (IMFP) λ_{in} are given by [37]:

$$-\frac{dE}{dS}(E) = \frac{1}{\pi a_0 E}\int_0^{E/2}(\hbar\omega)\,\mathrm{Im}[-1/\varepsilon(\omega)]In\{\frac{\sqrt{E}+\sqrt{E-2\hbar\omega}}{\sqrt{E}-\sqrt{E-2\hbar\omega}}\}d(\hbar\omega) \tag{2.5}$$

$$\lambda_{in}^{-1}(E) = \frac{1}{2\pi a_0 E}\int_0^{E/2}\mathrm{Im}[-1/\varepsilon(\omega)]In\{\frac{1-\hbar\omega/2E+\sqrt{1-2\hbar\omega/E}}{1-\hbar\omega/2E-\sqrt{1-2\hbar\omega/E}}\}d(\hbar\omega) \tag{2.6}$$

The optical dielectric constant $\varepsilon(\omega)$ is related to the refractive index n and the extinction coefficient k by:

$$\varepsilon(\omega) = (n + ik)^2 = (n^2 - k^2) + i(2nk) \tag{2.7}$$

The optical properties of materials in the photon energy range above about 30 eV can be described by the atomic scattering factors. The index of refraction of a material is related to the scattering factors of the individual atoms by:

$$n = 1 - \frac{r_e}{2\pi}\lambda^2 \sum_i n_i f_1^i \tag{2.8}$$

$$k = \frac{r_e}{2\pi}\lambda^2 \sum_i n_i f_2^i \tag{2.9}$$

where r_e is the classical electron radius, λ is the wavelength of the incident electron, and n_i is the atom number volume density of element i. f_1, f_2 are the real and imaginary part of atomic scattering factor, respectively [30].

2.2.4 Monte Carlo procedure and programming

First we used three uniform random numbers [0, 1], R_i to determine the beta particle coordinates x_i^0, initially generated in radioisotope thin film source with dimension size D^i (i =1, 2, 3):

$$x_i^0 = R_i \cdot D_i \tag{2.10}$$

The initial energy of the beta particle is determined by another uniform random number R_4 by:

$$R_4 < \int_0^E N(E')dE' \Big/ \int_0^Q N(E')dE' \tag{2.11}$$

The initial angle distribution of the beta particle is assumed to be isotropic. So its initial moving direction angle θ^0 and azimuthal angle ϕ^0 are determined respectively by another two uniform random numbers R_5 and R_6:

$$\theta^0 = \pi R_5, \qquad \phi^0 = 2\pi R_6 \tag{2.12}$$

The total mean free path λ_m is related to the corresponding elastic mean free path λ_e and the inelastic mean free path λ_{in} by:

$$\lambda_m^{-1} = \lambda_e^{-1} + \lambda_{in}^{-1} \tag{2.13}$$

The travel distance between two successive collisions is evaluated by another uniform random number R_7:

$$s = -\lambda_m In(R_7) \tag{2.14}$$

After passing distance *s*, uniform random number R_8 is used to determine the type of next individual scattering event, elastic or inelastic, by:

if $R_8 < \lambda_e^{-1} / \lambda_m^{-1}$ is true, it is elastic, otherwise, it is inelastic.

For elastic scattering, we used uniform random number R_9 to determine the i^{th} element atom, which would be responsible for this individual elastic scattering:

$$\frac{\sum_{j=1}^{i-1} \frac{C_j \sigma_e^j}{A_j}}{\sum_{j=1}^{n} \frac{C_j \sigma_e^j}{A_j}} < R_9 < \frac{\sum_{j=1}^{i} \frac{C_j \sigma_e^j}{A_j}}{\sum_{j=1}^{n} \frac{C_j \sigma_e^j}{A_j}} \tag{2.15}$$

The elastic scattering angle θ_e is determined by random number R_{10}:

$$R_{10} < \int_0^{\theta_e} \sigma_e \sin\theta' d\theta' \Big/ \int_0^{\pi} \sigma_e \sin\theta' d\theta' \tag{2.16}$$

The azimuthal angle ϕ^e is assumed to be isotropic and be determined by random number R_{11}:

$$\phi^e = 2\pi R_{11} \tag{2.17}$$

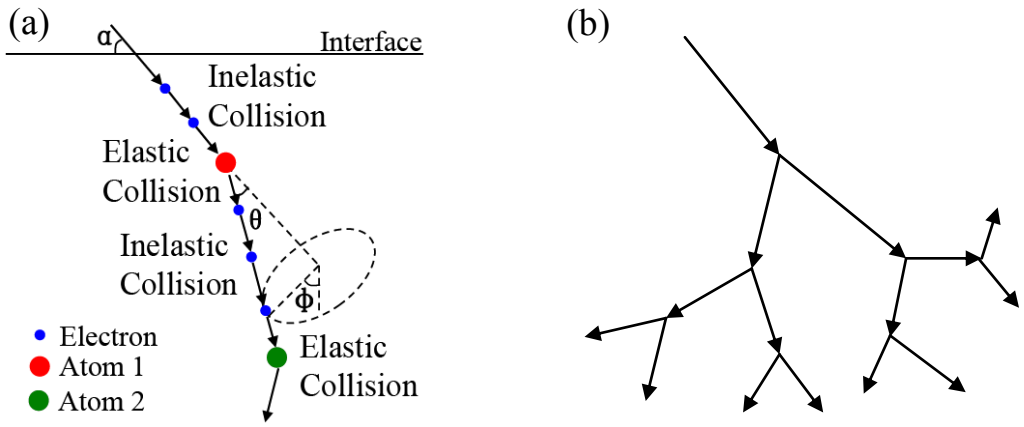

Figure 2.4: (a) Schematic image of MC model for electron trajectory simulation in solids. Both elastic scattering and inelastic scatterings for primary electrons, as well as for cascade secondary electrons, are considered.(b) Schematic for the cascade process of the secondary electron generation inelastic scattering process. All these secondary electrons have been tracked in the MC simulation.

For inelastic scattering, the energy loss ΔE for this individual event is given by:

$$\Delta E = -\frac{dE}{dS} \cdot s \tag{2.18}$$

The inelastic scattering angle θ^{in} is predicated by a classical binary collision model:

$$\theta^{in} = \sin^{-1}(\Delta E / E)^{1/2} \tag{2.19}$$

The azimuthal angle ϕ^{in} is also assumed to be isotropic and be determined by

random number R_{12}:

$$\phi^{in} = 2\pi R_{12} \tag{2.20}$$

The energy loss ΔE is considered to be transferred to the generated secondary electron, which will have initial energy $E_0^s = \Delta E + E_F$ for valence electron excitation or $E_0^s = \Delta E - E_B$ for ionization where E_B is the binding energy [35]. Some of ehe secondary electrons might have high enough energy so that they would create more secondary electrons, leading to a cascade process of secondary electron generation (Fig. 2.4b). In the MC simulation, all these secondary electrons will be tracked.

2.3 Monte Carlo simulation results

2.3.1 Electron in solid parameters

The elastic mean free path (EMFP) and the inelastic mean free path (IMFP) of high-energy incident electrons in solid are dependent on the energy of electron and the material properties of these solids. EMFP and IMFP can be calculated by equation 2.3 and equation 2.6, respectively. Another important property parameter of the material, stopping power, is defined as the average energy loss of the particle per unit path length, measured for example in keV/nm. Stopping power can be calculated by equation 2.5. Here, our Monte Carlo simulation code is able to calculate these parameters for various materials, such as metal Au, W, Ni, resist NEB31A, etc. These results are shown in figure 2.5.

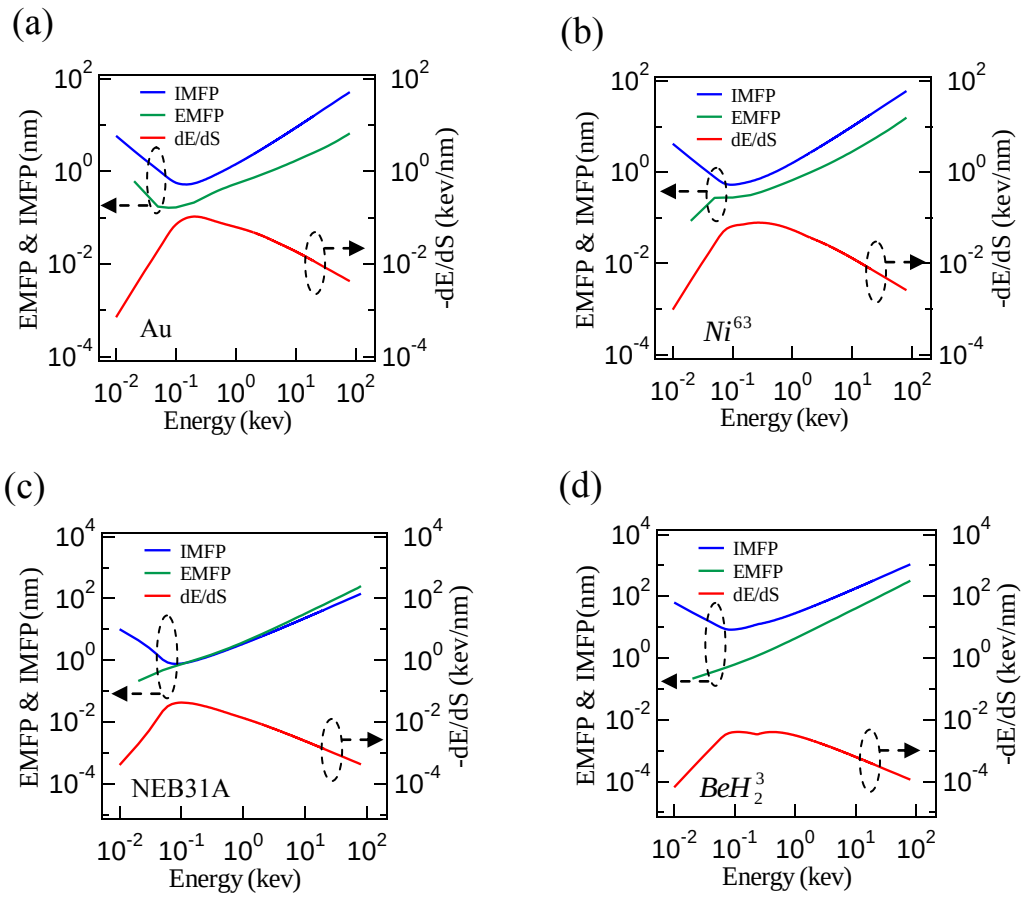

Figure 2.5: Elastic Mean Free Path (EMFP) vs. Energy, Inelastic Mean Free Path (IMFP) vs. Energy, Stopping Power vs. Energy curves for meat Au (a), metal ^{63}Ni (b), e-beam resist NEB31A (c) and beryllium tritide (BeH_2^3) (d), respectively.

2.3.2 RIPEL mask parameter simulation

We can use Monte Carlo simulation code to calculate the optimized thickness of the supporting layer nitride film of the mask, in order to make sure enough number of the high-energy electrons penetrate this supporting nitride layer. Following images showed our Monte Carlo simulation. The penetration depth in nitride film for 14.9 kev electron beam is around 2920 nm and the penetration depth for 10 keV beam is around 1410 nm

(Fig. 2.6).

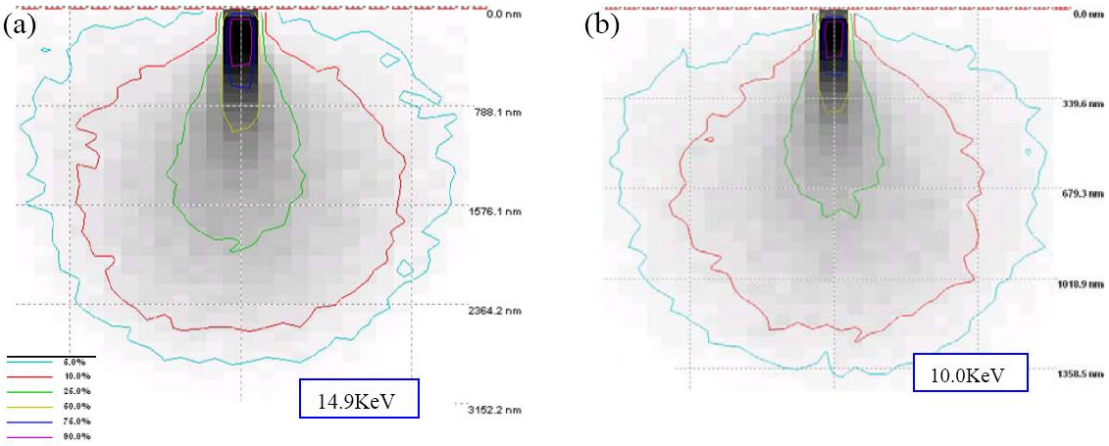

Figure 2.6: Monte Carlo simulated contour plot of the energy absorbed by nitride films, irradiated by an electron beam with various energies, 14.9 keV and 10.0 keV, in (a) and (b), respectively.

2.3.3 RIPEL critical dimension

3D Monte Carlo (MC) simulation was used to determine the theoretically limiting critical dimension achievable with RIPEL. In this method, the trajectories of primary and secondary electrons are tracked within the radioisotope thin films, metal mask, and the resist (Fig. 2.1). Both elastic scattering and inelastic scattering of the electrons are considered in the MC simulations. Nickel isotope ^{63}Ni or tritium ^{3}H thin films are used as the beta-particle sources in the simulations, whose half-lives are 100.1 years and 12.3 years, respectively. Based on decay theory, ^{63}Ni (^{3}H) has upper bound kinetic energies of 67 keV (18 keV) and average kinetic energies of 14.9 keV (5.9 keV) (Fig. 2.2), which are similar to the electron energy range used in a traditional EBL system. The energy transferred to the resist from the primary electrons and the generated secondary electrons

is recorded, and the energy contour images are shown in figure 2.5a top. For development

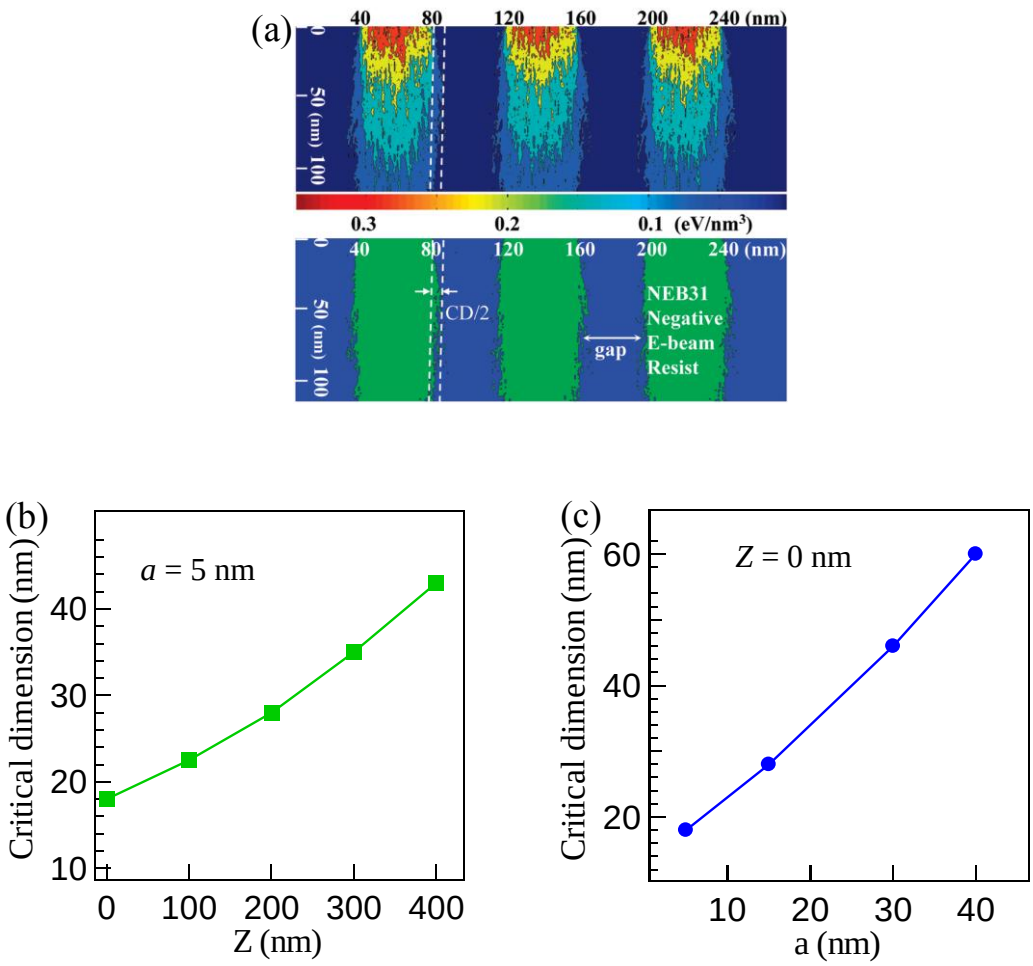

Figure 2.7: 3D Monte Carlo simulation for the critical dimension in RIPEL system. (a) 3D MC simulation for exposure and development processes, using a ^{63}Ni thin film (t = 10 μm) source to expose negative tone electron beam resist NEB31A (100 nm), with tungsten mask, a = 40 nm, t_1 = 1500 nm, t_2 = 150 nm. 500000 electrons, emitted from ^{63}Ni thin film (300 nm ×150 nm area size selected), were used. Top image is for exposure process, showing the cross section contour plot of the energy density deposited to the NEB31A resist; bottom image shows the resist profile after development process. (b) MC simulated critical dimension *vs* gap Z curves, for ^{63}Ni thin film source, when the mask feature size a (Fig. 2.1) is set to be 5 nm. (c). MC simulated critical dimension *vs* mask feature size a curves, for ^{63}Ni thin film source, when the gap Z is set to be zero.

process simulation, we used the model that if the resist absorbed a threshold energy density value J_0, it would be exposed. The threshold value J_0 could be determined by previous experimental dosage data for this resist. The simulated resist pattern profile, after a simulated development process, is also shown (Fig. 2.7b bottom), correspondingly. For ideal proximity contact between mask and resist (Z = 0 nm), the lateral CDs for 63Ni source exposure could be down to sub-20 nm (Fig. 2.7b). The small CD values could be understood to mean that the elastic mean free path and the inelastic mean free path of electrons in NEB31A resist are long enough that most of the electrons go right through the thin resist film without significant scattering. The CD increases with increasing the mask-resist gap (Z in Fig. 2.7b), since the source electrons are not intentionally focused in the RIPEL system. In order to achieve CD values less than 45 nm, we need to make mask-resist gap Z no larger than 400 nm, which is technically challenging but is a solvable engineering challenge. Since the CD is a weak function of mask-resist gap, variations in the gap will not affect the achieved pattern significantly.

2.3.4 RIPEL throughput

Based on MC simulation, the exposure time of RIPEL can be as short as 2 min (Fig. 2.7b) for each large area (10000 cm^2 or even more) parallel exposure, with *CD* less than 20 nm (Fig. 2.7b). Higher activity ^{63}Ni source will need much shorter exposure times. On the basis of simulation (Fig. 2.8), we could increase the thickness of ^{63}Ni thin film, which will give higher source activity, and larger flux current density J_e, leading to shorter exposure time. However, the flux current density value for the film source will saturate when the film thickness increases to twice the self-absorption depth [44]. This leads to

the saturation of flux current density (Fig. 2.8a). In MC simulation, the maximum value emission current density for ^{63}Ni thin film is 250 pA/cm^2, which means a minimum exposure time 1.9 h is required for each exposure on NEB31A resist, even by using a thick enough (>3 μm) ^{63}Ni thin film source in our lithography system (Fig.2.8b). However, a 1.9 h exposure time for each run is still too long for industrial commercialization. Therefore, another radioactive thin film source with much higher flux current density could be used in RIPEL. Tritium (^{3}H) is a good candidate because of its

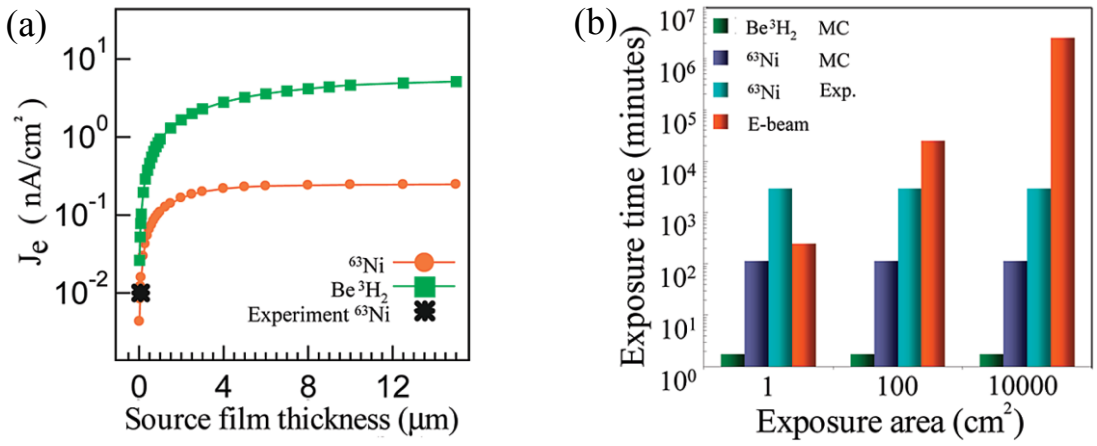

Figure 2.8: Potential better source design and exposure speed comparison with traditional e-beam system, for RIPEL system. (a) Flux current density *vs* source film thickness simulation curves (only electrons with E > 0.2 keV are counted), for ^{63}Ni and Be_3H_2 thin film. Flux current density saturates with increasing source film thickness, due to the self-absorption effect by source film. (b) Exposure time comparison among our RIPEL system with three different film sources and EBL system, for exposing different areas.

higher decay activity [45] and acceptable beta-particle energy range (average energy 5.9 keV), as well as long reasonably long half-life (12.3 years). According to our MC simulation considering the self-absorption effect, beryllium tritide (Be_3H_2) thin film source could have a very high flux current density up to 5.5 nA/cm^2 (Fig. 2.8a), due to

high specific activity of tritium, high tritium storage capacity [46, 47], and relatively small self-absorption effect of beryllium tritide (Be_3H_2). By using a beryllium tritide thin film source (J_e = 5.5 nA/cm^2) in RIPEL, the exposure times can be reduced down to approximately 2 min (Fig. 2.8b) for each large area (10000 cm^2 or even more) parallel exposure, with *CD* value not larger than 20 nm.

2.4 Analysis of RIPEL throughput

For RIPEL throughput calculation, Monte Carlo simulation is the most accurate, by tracking the trajectories of each primary electron and the generated secondary electron, although it is complicated. For RIPEL, the high energy beta electrons, emitted from the radioactive thin film source, have a continuous energy distribution (Fig. 2.2). Moreover, for our mask design, we use a thin layer of low mass density material as the supporting layer (Si_3N_4 used here) for the tungsten mask, to slow down the energy of the primary electrons as what we want. Here, we can use some simplified logical equations to do estimation calculations. The beta flux current density J_e, emitted from the radioactive thin film source, could be expressed by:

$$J_e = \frac{n \cdot \rho_s \cdot d \cdot N_0 \cdot e}{A} \cdot (1 - \exp(-0.693 / T_{1/2})) \tag{2.21}$$

where n is number of atoms of the radioisotope in molecule, N_0 is the Avogadro's constant, A is molecular weight, d is the thickness of the thin film source, ρ_s is the mass density of the source, e is the elementary charge, $T_{1/2}$ is the half live of the radioisotope. When d reaches twice of the self-absorption depth, it will lead to the maximum beta flux density value.

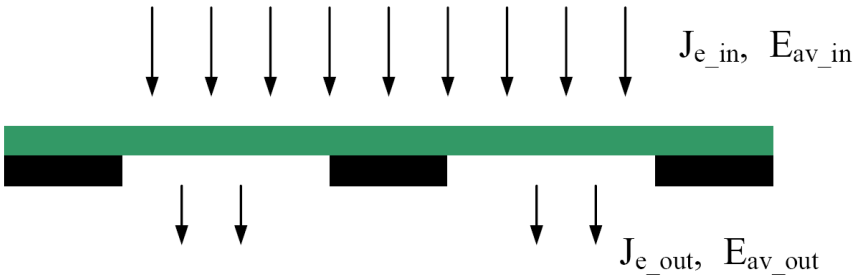

Figure 2.9: Schematic of the electrons flux through the membrane mask.

For the supporting layer of the stencil mask, most of the beta particles could penetrate. The relation between the in flux density (J_{e_in}) and the out flux density (J_{e_out}) could be given by:

$$J_{e\_out} = J_{e\_in} \cdot \exp(-\nu \cdot \rho \cdot h) \tag{2.22}$$

where ρ is the mass density of the supporting material, h is its thickness and ν is the mass absorption coefficient.

Also, the relation between the average energy of the incident beta flux E_{av_in} and the average energy of out-coming beta flux E_{av_out} could be solved by:

$$h = \int_{E_{av\_in}}^{E_{av\_out}} 1/(-\frac{dE}{dS}(E'))dE' \tag{2.23}$$

where dE/dS is the electron stopping power of the supporting layer (Equ. 2.5).

Finally, the total exposure time T needed could be given by:

$$T = \frac{\alpha \cdot J_{e\_out}}{\frac{dE}{dS}(E_{av\_out})} \tag{2.24}$$

where α is a constant related to the threshold exposure dosage needed for the specific e-beam resist. Here, dE/dS is the electron stopping power of the e-beam resist.

Table 2.1: Caparison of the properties of various e-beam resists.

E-beam Resist	Tone	Dosage Constant α ($\mu C/cm^2$)
PMMA	Positive	800-1200
NEB-31A	Negative	30-60
ZEP-520A	Positive	200-300
XR-1541	Negative	600-1200
ma-N 2403	Negative	350-450
ZEP-7000-22	Positive	40-80

2.5 Membrane shadow mask distortion for RIPEL

Mask distortion was the Achilles heel of previous attempts at electron projection and proximity printing lithography, since the irradiation energy would heat up the mask reticle locally during the exposure to cause uncorrectable membrane mask distortion, depending on the pattern density [9, 32, 48]. For all previous electron beam projection and proximity printing, they need high vacuum and expensive column to accelerate the electrons to high energy. Also the exposure process should be conducted in high vacuum. Since the exposure was conducted in high vacuum, the heating problem is circumvented, when the mask membrane is thin enough (~ 1 μm) for most of the electrons to pass through [9, 48]. Fortunately, this uncorrectable mask distortion problem does not exist in our RIPEL system, since RIPEL is a vacuum-free system. In our RIPEL system, since the beta electron emission used is independent of temperature or pressure, vacuum-free electron lithography is experimentally demonstrated for the first time. The heat on the membrane mask will be dissipated immediately by air molecules surround the membrane. Therefore the mask distortion could be ignored. Here let's do a simple calculation to confirm our statement above: Let's consider a 4-inch Si membrane mask with 1μm in thickness, with 100 mW/cm^2 power e-beam irradiating its center 1 cm X 1 cm area. Let's assume that 20% of the electron energy will be absorbed by the membrane mask. The heating up power is P = 20% *100 mW/cm^2 * 1 cm^2 = 20 mW. When it is in thermal balance, then the temperature difference between the center and the edge ΔT could be calculated as:

$$\Delta T = \frac{P}{k \cdot A / L} \tag{2.25}$$

where A is the thermal conducting area and L is the thermal conducting length.

If the exposure is conducted in high vacuum, most of the heat could only be dissipated along the membrane thin film. The thermal conducting area could be estimated as 4 cm * 1 μm and L could be estimated to be 4.5 cm. The conductivity of Si is around k = 150 W/(m*K). Therefore, we could get ΔT to be 150 K. This temperature increase will cause several microns of buckling height mask distortion, based on the calculation shown in figure 2.8 in the paper published by Bohlen [9].

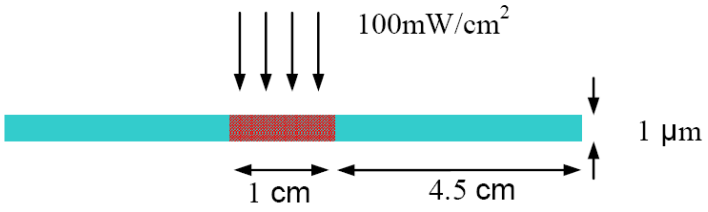

Figure 2.10: Schematic drawing for the mask heating during exposure.

If it is in air at atmosphere, most of the heat could be dissipated to air in the direction vertical to the membrane thin film. The thermal conducing area A' is 1 cm^2, and L' could be estimated to be 1 μm. The conductivity of air is around k' = 0.025 W/(m*K). Therefore, we could get $\Delta T'$ to be 0.008 K. This temperature increase for mask distortion could be fully ignored. Let's look at following calculation for the reason. The distortion ΔL can be expressed as:

$$\Delta L = L \cdot \alpha \cdot \Delta T' \tag{2.26}$$

where α is the thermal expansion coefficient. Let's take α to be 20 ppm/^{o}C and L to be 1 cm, we can get the distortion ΔL value to be around 1.6 nm, which could be ignored. This is consistent with our experiments that we did not notice any thermal mask

distortion for membrane mask, during exposure.

CHAPTER 3

PROOF-OF-CONCEPT EXPERIMENT FOR RIPEL

Proof-of-concept experiments were designed to demonstrate RIPEL using safe and low-activity ^{63}Ni thin film source. The emitted electrons are spatially blocked using a commercial transmission electron microscopy TEM grid as the mask that is placed in proximity to an electron sensitive resist on the silicon substrate. The hole size in the TEM grid is around 5 μm. The electrons that are not blocked, impact and enter the e-beam resist, along with secondary electrons generated by primary electrons impacting the sidewalls of the stencil layer.

3.1 Source flux current density measurement

The radioactive ^{63}Ni thin film was deposited by electro-less nickel plating technique [49], on a Ni substrate that was pre-polished using chemo-mechanical polishing to

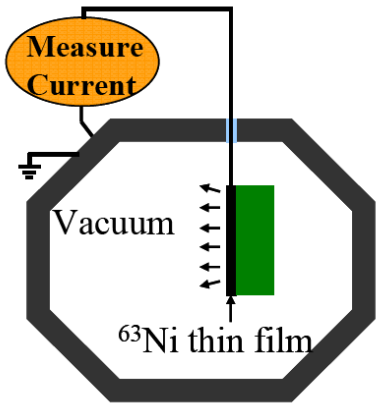

Figure 3.1: Schematic drawing of the experimental setting up, measuring flux current density J_e of our ^{63}Ni thin film source.

achieve sub-nm level smoothness. The thin film source (1 cm X 1 cm in size) flux current density J_e was measured by placing the source in a metal vacuum chamber, with pressure down to 10^{-6} mbar (Fig. 3.1). The measured J_e value for our source was 10.03 pA/cm^2.

3.2 Electron sensitive resist selection for RIPEL

Conventional electron beam resist can be used in our RIPEL system. However, since our source has low activity, we selected chemically amplified electron resists that need lower

Table 3.1: Electron resist property and process condition information.

Name		**ZEP 7000-22**	**NEB31A**
Tone		Positive	Negative
Resolution		Very high	Very high
Contract		High	High
Etch Resistance		Good	Good
White light		Sensitive	Sensitive
Company		Nagase California Corp., Sunnyvale, CA	SUMIKA Electronic Materials, Inc., Phoenix, AZ
Steps	**Spin Time**	60 seconds	60 seconds
	Pre-bake	170 ℃ hotplate, 2 minutes	110 ℃ hotplate, 2 minutes.
	Dosage	40-80 μC/cm^2 at 100 kV	30-60 μC/cm^2 at 100 kV
	Post-bake	115˚C hotplate, 2 minutes	95˚C hotplate, 2 minutes
	Develop	ZED-500 for 2 minutes	MIF 321 for 30 seconds
	Rinse	Rinse with IPA	Rinse with DI water
	Blow dry	With nitrogen	With nitrogen

dose for exposure. Chemical amplification is often used in electron-beam resists to reduce its exposure dose requirement. Normally, the chemically amplified ebeam resists require a post-exposure bake step, in which acids released by the exposure radiation diffuse during the post bake step. These acids render surrounding polymer soluble in developer. A single acid molecule can catalyze many such reactions, leading to fewer photons or electrons requirements [50]. Acid diffusion is important, because it can to increase resist sensitivity and throughput and it can also limit line edge roughness due to

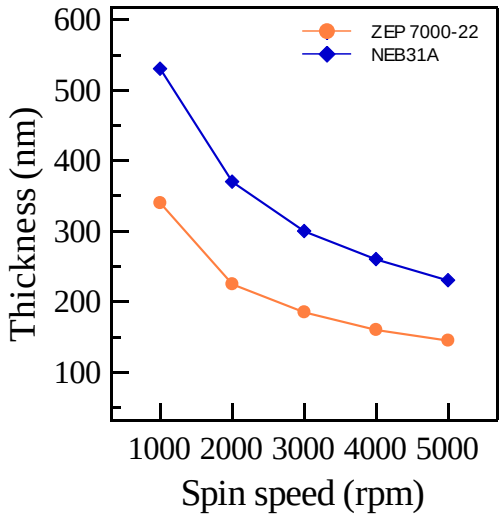

Figure 3.2: Resist spin speed curves for chemically amplified electron resist ZEP 7000-22 and NEB31A.

shot noise statistics. However, the acid diffusion length itself can potentially limit the resolution and too much diffusion reduces chemical contrast, resulting in more roughness [51]. We have two kinds of chemically amplified electron lithography resists, which are suitable for RIPEL system. Their properties and process information are list in table 3.1. The resist spin speed curves of these two electron resists are shown in figure 3.2. In order to achieve higher resolution, normally thinner resist film is needed. We can

use some chemical solution to dilute the resist, such as thinner A (anisole). For example, for NEB31A, uniform thin layer of ~20 nm can be reached by using diluted resist solution at high spin speed (eg. 8000 rpm for 60 seconds).

3.3 Proof-of-concept experiments

For the first stage experiment, we just used commercialized transmission electron microscopy (TEM) grid as the mask in RIPEL system (Fig. 3.3). These TEM grids have square-shape or circular shape holes with size around 5 μm. They are made of copper or nickel. We can use both positive and negative tone resist in RIPEL system.

3.3.1 Experiment results with positive tone resist

Experiment Details: Positive tone chemically amplified electron resist ZEP 7000-22 was spun onto silicon wafer substrate at 6000 rpm for 60 seconds, followed by post bake at 170 ^{o}C for 2 minutes. Then TEM grid was put on top of the resist film and the ^{63}Ni thin film source was placed on top of the TEM grid mask to expose the resist in air for 120 hours continuously (Fig. 3.3a). The exposure was conducted in dark room due to the high sensitivity of chemically amplified resist to white light. After exposure, the wafer was post baked at 115^{o}C for two minutes, developed it in ZED-500 solvent for 120 seconds, followed by IPA rinsing and nitrogen gun blow drying.

Results: An optical profilometer was used image the resist pattern. The height contour image of the resist pattern was achieved (Fig. 3.4), showing reasonably good pattern edges. The long exposure time 120 h is needed to get enough dosage due to the low activity of the source 10 pA/cm^2 we used. During the long time exposure, the sample

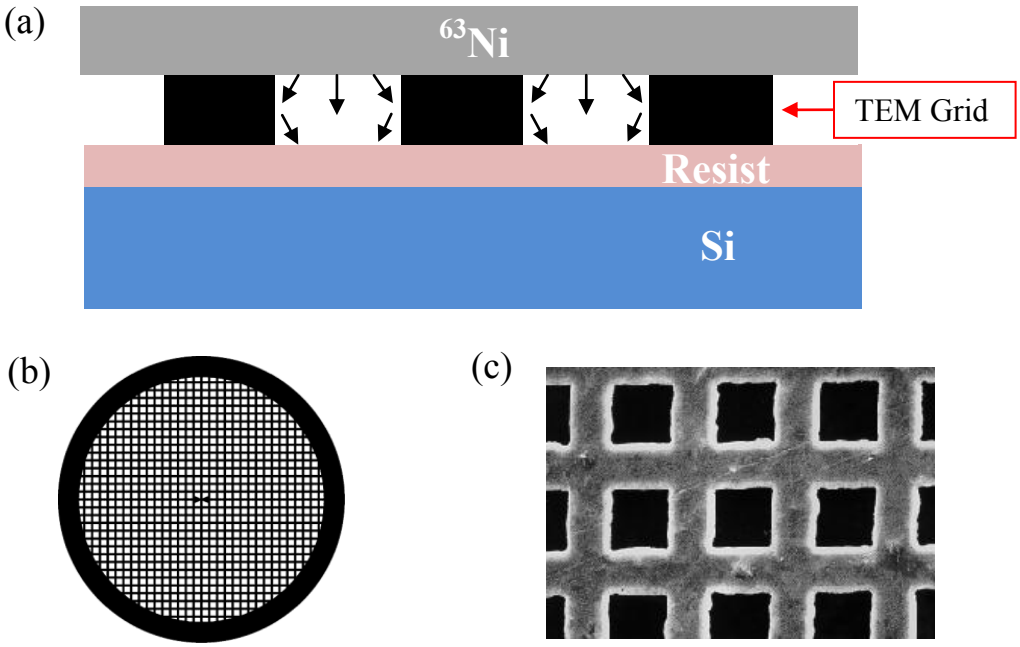

Figure 3.3: (a) Schematic of RIPEL set up for proof-of-concept experiment. (b) Photo image of the commercialized TEM grid. (c) SEM image of the TEM grid, with 5 μm square holes. Images are cited from company website (SPI).

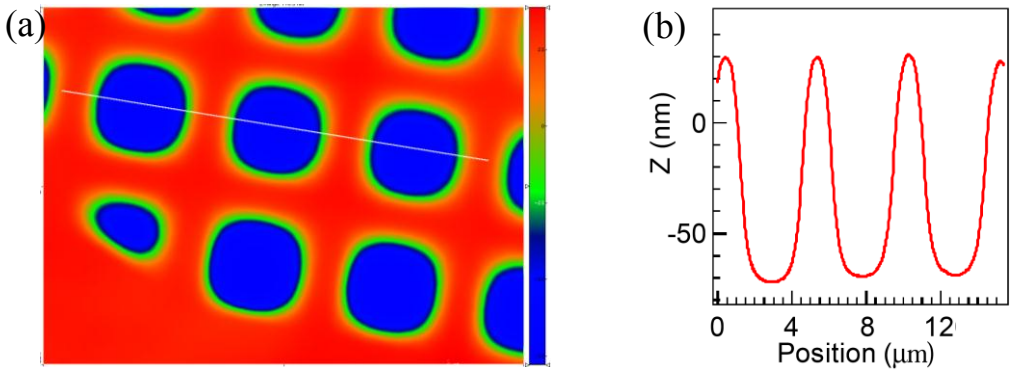

Figure 3.4: Positive resist ZEP 7000-22 (100 nm thick) patterns by RIPEL using ^{63}Ni thin film source J_e =10 pA/cm^2 to expose the commercial TEM grid as the mask (with mask hole size around 5 μm) (a) Optical profilometer height contour image of the resist pattern with RIEPL exposure, followed by normal development process . (b) Height *Z vs* position plot of the dashed line region in (a).

vibrations were controlled to achieve low enough positional drift by using vibration isolation table. By increasing the radioactively emitted electron current by using radioisotopes with much higher specific activity, much smaller exposure times can be achieved.

3.3.2 Experiment results with negative tone resist

Experiment Details: Negative tone chemically amplified electron resist NEB31A was spun onto silicon wafer substrate at 8000 rpm for 60 seconds, followed by post bake at

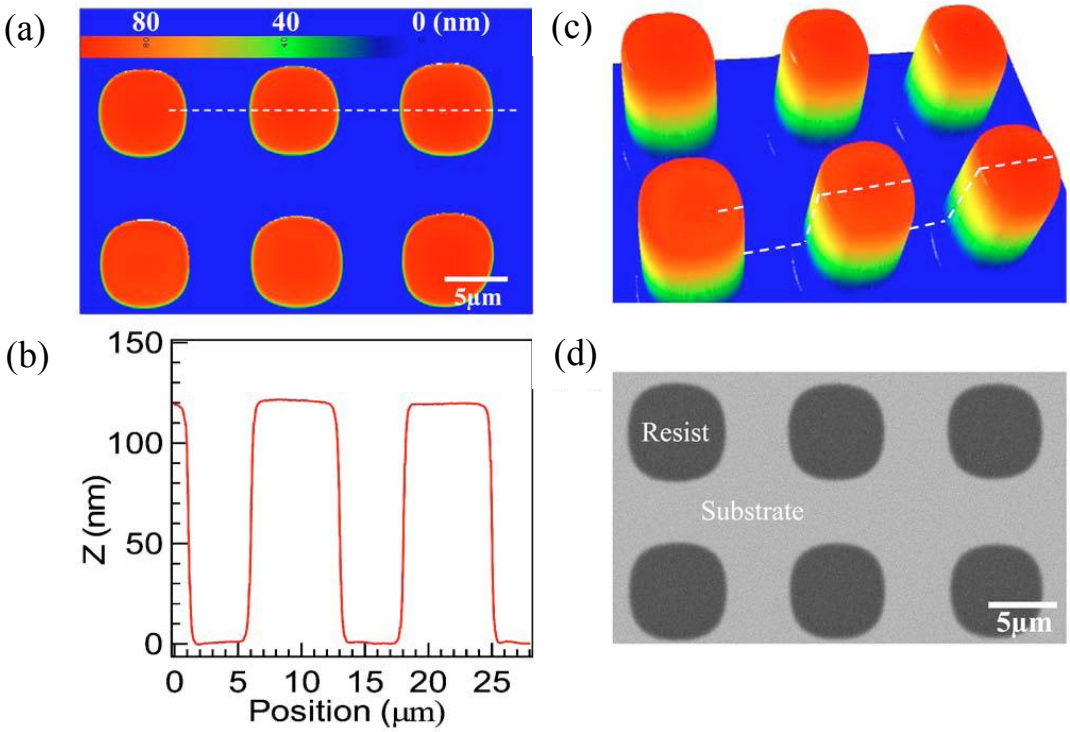

Figure 3.5: Negative resist NEB31A (120 nm thick) patterns by RIPEL using ^{63}Ni thin film source J_e =10 pA/cm^2 to expose the commercial TEM grid as the mask (with mask hole size around 5 μm) (a) Optical profilometer height contour image of the resist pattern with 90 hours continuous exposure, followed by normal development process. (b) Height Z *vs* position plot of the dashed line region in (a). (c) 3D optical profilometer scan view image of the same resist pattern in (a). (d) SEM image of the same resist pattern showed in (a).

110 ^{o}C for 2 minutes. Then TEM grid was put on top of the resist film and the ^{63}Ni thin film source was placed on top of the TEM grid mask to expose the resist in air for 90 hours continuously (Fig. 3.3a). The exposure was conducted in dark room due to the high sensitivity of chemically amplified resist to white light. After exposure, the wafer was post baked at 95^{o}C for two minutes, developed it in MIF321 solvent for 30 seconds, followed by DI water rinsing and nitrogen gun blow drying.

Results: An optical profilometer was used image the resist pattern. The height contour image of the resist pattern was achieved (Fig. 3.5), showing sharp pattern edges. The scanning electron microscopy (SEM) image of the same resist pattern was also shown.

3.4 Summary and discussion

In the first stage of proof-of-concept experimental demonstration for RIPEL, reasonably good resist patterns were created, with a feature size down to around 5 μm. The feature size is determined by the size of the TEM grid mask we used. Moreover, two types of electron resist, positive tone ZEP 7000 and negative tone NEB31A, were successfully used in RIPEL system. From the experiment data, we can see that negative tone NEB31A shows sharper pattern edges than that from ZEP 7000. Also, NEB31A needs lower dosage than ZEP 7000. Therefore, in the future RIPEL experiments, NEB31A would be more frequently used.

Currently, TEM grid was used as the mask and it has rough mask edge and low resolution. In order to achieve better resolution in RIPEL system, new mask based on micro-/nano-machining technology needs to be developed.

CHAPTER 4

SECOND-STAGE RIPEL WITH MICRO-MACHINED MASK

4.1 RIPEL with micro-machined Au stencil mask

Mask Fabrication: In order to get fine structure with smaller dimension size, a micro-machined mask was developed, instead of using TEM grids as the mask. For mask fabrication, a thin layer of low stress silicon nitride Si_3N_4 film (350 nm) was deposited on both sides of a double polished silicon wafer by low pressure chemical vapor deposition (LPCVD) at 800 ℃. The bottom side nitride film was etched down to 100 nm by nitride reactive ion etching (RIE) CHF_3 /O_2. Then, the bottom nitride film was patterned by EBL (100 keV beam energy), followed by RIE nitride etching to etch through the 100 nm nitride film. Afterward, backside-alignment optical

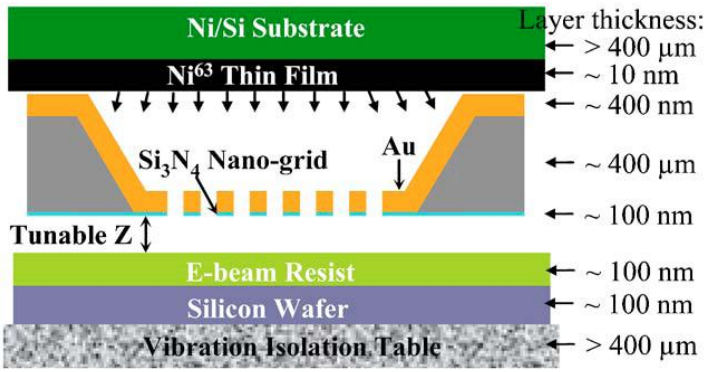

Figure 4.1: Schematic drawing of experimental setting up, using radioactive ^{63}Ni thin film source (J_e = 10 pA/cm^2) to expose the fabricated nano-stenciled mask that is placed proximity to negative e-beam resist NEB31A (120 nm).

lithography was used to pattern a resist window on the back side of the wafer, followed by nitride RIE etching through the 350 nm nitride film on the back side. Then, KOH etching at 80 ℃ temperature was used to back etch through the silicon wafer, stopping at the top side nitride layer. Finally, a layer of Au (10 nm Ti +500 nm Au) was deposited from the top side of the wafer by metal evaporator at very slow deposition rate. Therefore, the aspect ratio of the Au thickness to opening was 5:1.

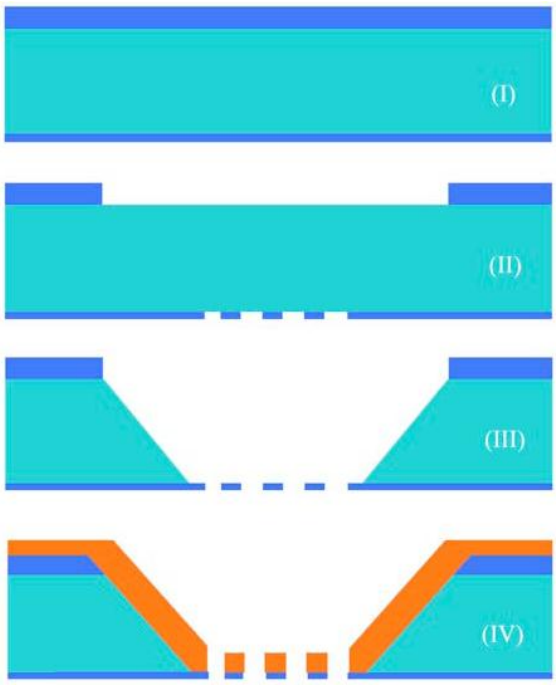

Figure 4.2: Nano-stenciled mask fabrication process: i) thin layer of low stress silicon nitride Si_3N_4 film (350 nm) was deposited on both sides of a double polished silicon wafer by LPCVD. The bottom side nitride film was etched down to be 100 nm by nitride RIE. ii) The bottom nitride film was patterned by EBL (100 keV beam energy), followed by RIE nitride etching to etch through the 100 nm nitride film. Back-side-alignment optical lithography was used to pattern a resist window on top side of the wafer, followed by nitride RIE etching through the 350 nm nitride film on the top side. iii) KOH etching of silicon was used to back etch through the silicon wafer, stopping at the top side nitride layer. iv) a layer of Au (10 nm Ti + 500 nm Au) was formed by evaporation from the top side of the wafer.

Resist and Exposure: The anisole diluted chemical amplified negative-tone e-beam resist NEB31A was spun on at high speed (10000 rpm) to a thickness of ~60nm, followed by post bake at 115 ^{o}C for 2 minutes. Then tungsten mask (made above) was put on top of the NEB31A film and the ^{63}Ni thin film source was placed on top of the mask to expose the resist in air. The exposure was conducted in dark room due to the high sensitivity of NEB31A resist to white light. After exposure, the wafer was post baked at 95 ^{o}C for two minutes, developed it in MF321 for 30 seconds, followed by DI water rinsing and nitrogen gun blow drying.

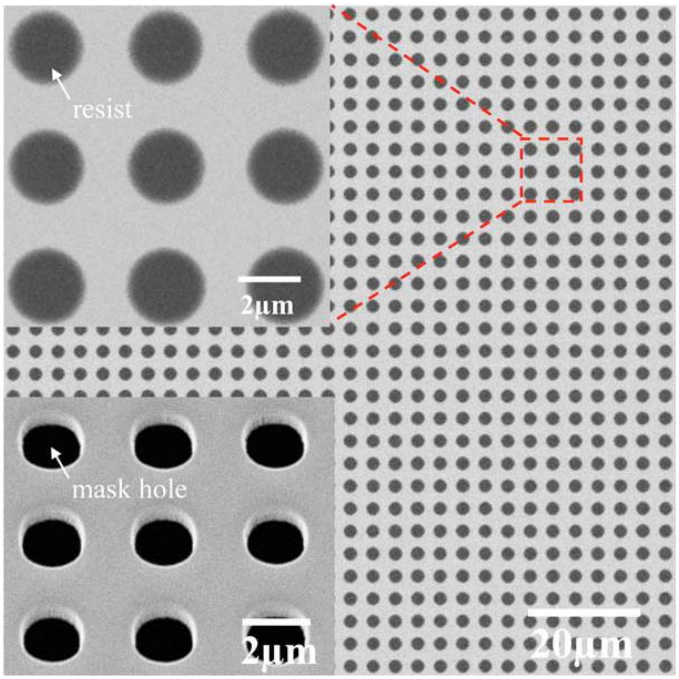

Figure 4.3: Pattern results by RIPEL using micro-machining fabricated stencil Au mask. SEM image of the resist patterns, using radioactive ^{63}Ni thin film source (J_e=10 pA/cm^2) to expose the mask that is placed proximity to negative e-beam resist NEB31A (120 nm). The left-bottom inset shows the SEM image of the Au membrane mask (500 nm in thickness).

By using the micro-machining fabricated Au mask, we achieved a uniform pattern definition across the exposed area (Fig. 4.3). Compared with previous results using TEM grids as the mask (Fig. 3.5), these patterns show smaller feature size and more smooth edges (Fig. 4.3).

4.2 RIPEL with nano-machined tungsten stencil mask

For the micro-machined Au stencil mask, nitride film was etched through, which prevents disjoint features, such as donut shapes, to be formed. Therefore, we need to a layer of continuous "opaque" supporting layer for mask. Here, we designed and fabricated a new mask technology for RIPEL. In the new mask design, the continuous silicon nitride and tungsten thin layer laminate is formed. Furthermore, the tungsten layer is etched partially to define the areas where electrons are transmitted to the resist.

Mask Fabrication: A layer of low stress silicon nitride (Si_3N_4) film was deposited on both sides of a double polished silicon wafer by Low Pressure Chemical Vapor Deposition (LPCVD) at 800 ℃. Then a thin layer of tungsten (~150 nm) was sputtered on top of the bottom nitride film, followed by 20 nm of Cr evaporation on top of tungsten. Then the Cr film will be patterned by EBL (100 keV beam energy) using ZEP520 resist. Cr was etched by Cr RIE etching, using ZEP520 as the etching mask. Then tungsten was etched by tungsten RIE (CF_4/SF_6) etching, using Cr as etching mask. Afterwards, back-side alignment optical lithography was used to pattern a resist window on back side of the wafer, followed by nitride RIE etching through the nitride film on the backside. Then KOH etching at 80 ^{o}C temperature was used to back etch through the silicon wafer, stopping at the bottom nitride layer (Fig. 4.4).

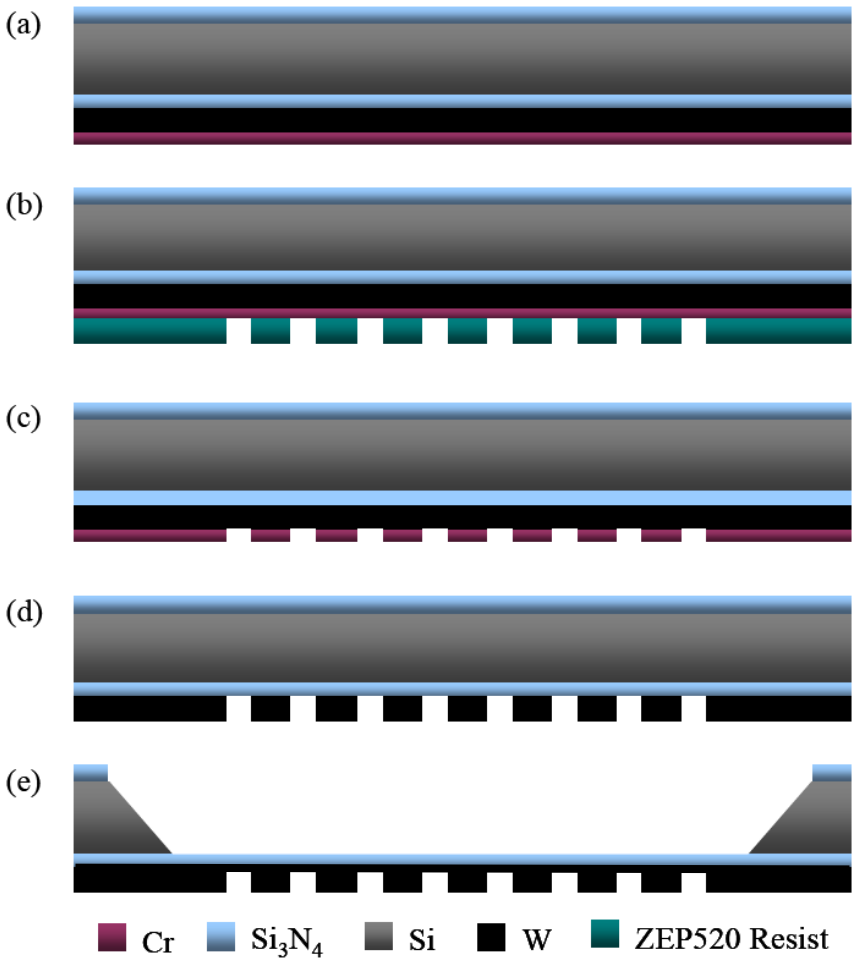

Figure 4.4: RIPEL tungsten mask nano-fabrication process. (a) Low stress LPCVD nitride deposition on double polished Si (100) wafer, followed by 150 nm of W sputtering and 20 nm of Cr evaporation on the front side. (b) E-beam lithography patterning, using ZEP520 resist. (c) Cr RIE etching, using ZEP520 as the etching mask. (d) W RIE (CF_4/SF_6) etching, using Cr as etching mask. (e) Back side nitride window patterning by optical lithography, nitride RIE etching, followed by KOH (80 ^{o}C) Si etching to etch through the Si wafer.

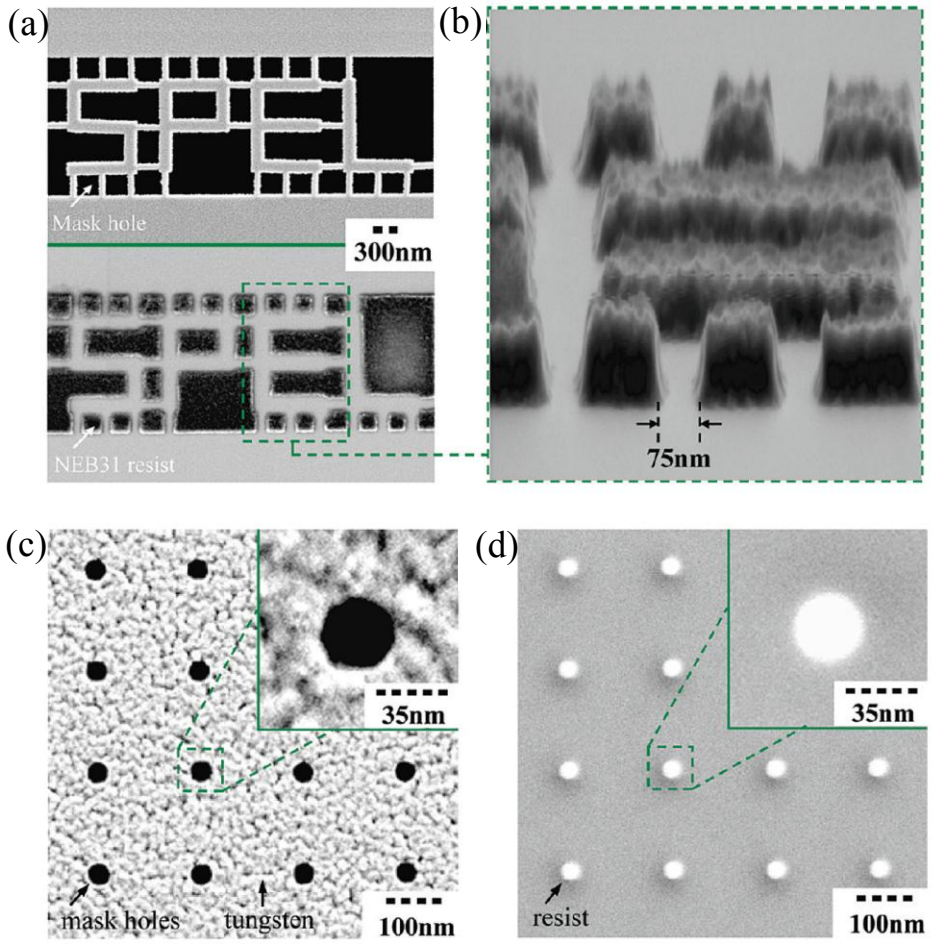

Figure 4.5: Pattern results by RIPEL using nano-machining fabricated stencil tungsten mask. (a) SEM images for the mask (upper) and corresponding NEB31A resist pattern (lower), for letters "SPEL". (B) Side view SEM image of the NEB resist pattern for the region within the dashed line square in (a). 75 nm pattern gap was achieved. (c) SEM images of the tungsten mask, with 35 nm hole arrays. (d) SEM images of the corresponding NEB31A resist pattern (60 nm in thickness), created by the mask in (d), using the RIPEL system with ^{63}Ni thin film source.

Experiments were designed to demonstrate the concept of our SPEL system, using a safe low-activity (1.5 mCi/cm^2) particle emitting ^{63}Ni thin film source with electrons emitted at average energy of 14.9 keV to expose the negative tone chemical amplified e-

beam resist NEB31A, through a nanofabricated stencil tungsten mask. Tungsten was used as the stencil mask material since it has a high stopping power to maximally absorb lateral electrons and also have good conductivity to eliminate charging of the mask layer. A layer of low stress LPCVD silicon nitride Si_3N_4 thin film (1500 nm thick) was used as the supporting layer for tungsten mask (150 nm thick). The tungsten layer was patterned by electron beam lithography (with 100 keV beam energy) and tungsten RIE etching. The primary electrons traverse the silicon nitride layer with the electron energy reduced to an average of 10 keV are then fully blocked by the tungsten layer in the non-hole region. Figure 4.5a shows the mask for letters "SPEL" and its corresponding NEB31A resist pattern. The side view in figure 4.5b shows 75 nm gap between posts. Also, hole arrays with 35 nm diameter were patterned on the tungsten mask (Fig. 4.5c) and the corresponding NEB31A resist patterns were achieved by RIPEL (Fig. 4.5d).

4.3 RIPEL with self-assembled Au nano-bead mask

It is very difficult to use e-beam lithography to create mask with feature size smaller than 20 nm, since sub-20 nm is almost the resolution limit of the e-beam lithography available at CNF. Furthermore, there is an error in the pattern transfer process from resist to tungsten layer. In order to push the resolution limit of RIPEL system, we proposed to use self-assembled Au nano-bead (with diameter less than 20 nm) as the mask (Fig. 4.6) to stop electrons.

Experiment Details: Au nano-bead solution (from NanoComposix) droplets (60 μL, Au nano-bead concentration 0.05 mg/mL) were poured on top of Si chip that had been coated with thin resist NEB31A layer (~20 nm). The solvent dried in air and the Au

nano-bead are self-assembled on the resist top surface. After that, the chip was irradiated by ^{63}Ni electrons for exposure, followed by NEB31A normal development processes.

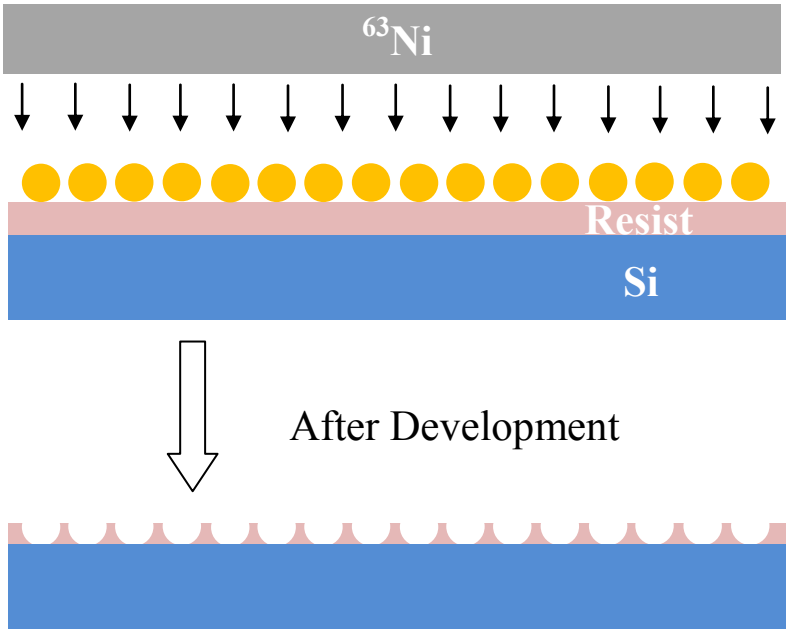

Figure 4.6: Schematic plot of the experiment set up for RIPEL with self-assembled Au nano-bead mask. Au nano-bead (< 20 nm in diameter) is self-assembled onto the negative resist NEB31A thin layer. After RIPEL exposure and development, the un-exposed resist under the nano-bead will be removed and the nano-bead will be lift off and washed away as well.

From the resist pattern SEM image (Fig. 4.7b), we can see that two kinds of patterns were created: nano-holes and nano-rings. Some nano-holes have diameters less than 20 nm, while the nano-rings show even smaller feature size, down to sub-10 nm. Figure 4.7c shows the possible reason. After exposure from ^{63}Ni electrons, the resist was exposed except the region under the Au nano-beads. Since these Au nano-beads are electrically isolated, they were all negatively charged due to exposure. Figure 4.7d shows the calculated electrical field around these Au nano-beads, with the assumption that each gold nano-bead has a total charge of 10 electrons. The particle with smaller diameter

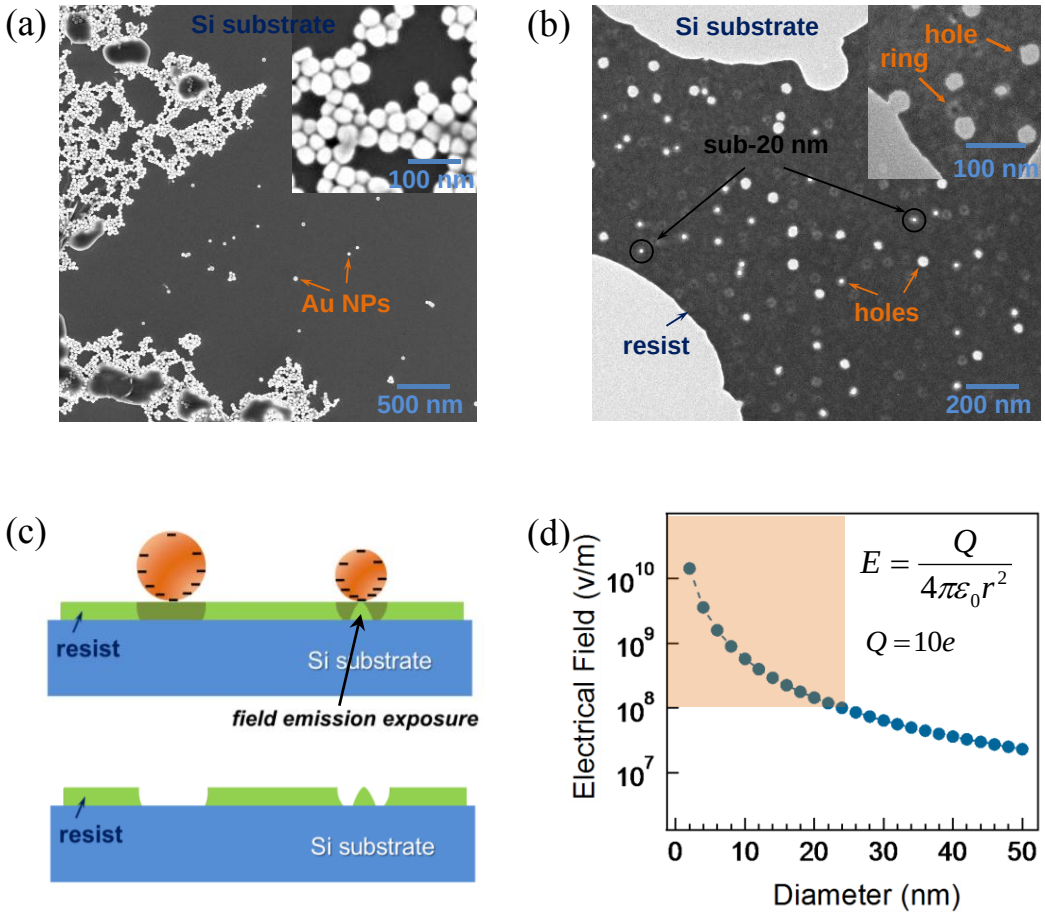

Figure 4.7: (a) SEM image of the Au nano-bead on Si substrate. (b) SEM image of the resist patent, created by RIPEL using Au nano-bead as the mask. Insect shows its zoom-in image. There are two kinds of patterns created: nano-holes and nano-rings. (c) Schematic plots showing the reason for these two kinds of patterns. Top shows the pattern after exposure. The nano-bead with smaller diameter is more likely to have a field emission due to higher electrical field (d), leading to emission exposure for the resist underneath.

shows higher electrical field value, which could reach the threshold value of field emission. The field emission caused the exposure for the resist underneath, leading to the nano-ring shaped resist pattern (Fig. 4.7c). By this technique, we demonstrate that RIPEL has the capability to realize high resolution, less than 20 nm, or even less 10 nm.

4.4 RIPEL with curved source for higher throughput

In our proof-of-concept experiment for RIPEL, a radioactive ^{63}Ni thin film source was used. The ^{63}Ni thin film was purchased. The films are commercially deposited by electro-less nickel plating technique, onto a Ni/Silicon substrate that was pre-polished using chemo-mechanical polishing to achieve sub-nm level smoothness. For a planar ^{63}Ni, on

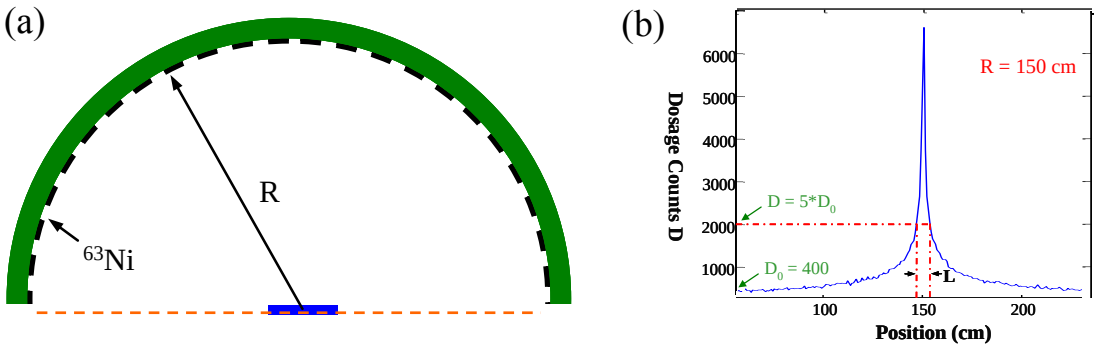

Figure 4.8: (a) Schematic of curved source for flux enhancement. Small pieces of ^{63}Ni sources were placed on curved semi-sphere and the sample (with stencil mask on top) will be put on the center of the semi-sphere, for exposure. (b) Monte Carlo simulated Flux vs. Position, with curved sources. The position is shown in the dashed line in (a). In the center position of the semi-sphere, the flux is highly enhanced.

the basis of simulation (Fig. 2.7a), we could increase the thickness of ^{63}Ni thin film to get larger flux current density J_e, leading to shorter exposure time. However, the flux current density value for the film source will saturate when the film thickness increases to twice the self-absorption depth. For the self-absorption effect, it means that the high energy electrons emitted at the bottom of the radioactive thin film cannot escape the film and will be absorbed by the film itself. This leads to the saturation of flux current density (Fig. 2.7a). In MC simulation, the maximum value emission current density for ^{63}Ni thin film is 250 pA/cm^2.

In order to further enhance the flux for RIPEL, small pieces of ^{63}Ni sources were placed on the inner surface of a hemisphere, with fabricated holders to expose the sample (with stencil mask on top) that is placed on the center of the semi-sphere. We demonstrated a new RIPEL system, using curved source for focused flux, leading to further enhanced lithography throughput (Fig. 4.8a). Our 3D Monte Carlo simulation shows that the flux on the center can be enhanced by a factor of ten, using a radius of 150

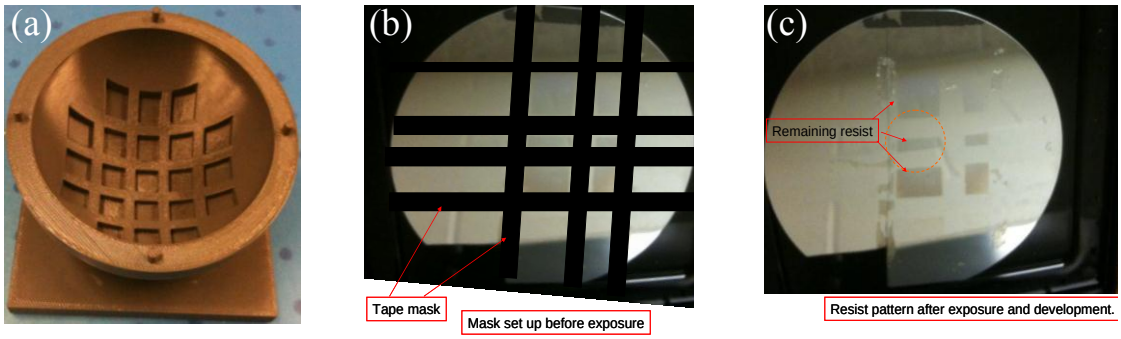

Figure 4.9: Proof-of-concept demonstration of curved source for flux enhancement. (a) Photo image of the semi-sphere source holder. (b) mm scale size tape was put on a 4-inch wafer, which has negative e-beam resist on. (c) Small pieces of ^{63}Ni sources were placed on curved semi-sphere, to expose the 4-inch wafer. After exposure, the tape was removed and normal e-beam resist development was carried out. Only the central part shows remaining resist, indicating that the central part has enough dosage.

cm semi-sphere holder. In order to prove this concept, experiments were conducted using a plastic semi-sphere source holder (Fig. 4.9a), carrying 22 pieces of low-activity (10 mCi/cm^2) beta particle emitting ^{63}Ni thin film source (1x1 cm^2 size each), to expose a 4-inch wafer that was coated with uniform negative e-beam resist NEB31A. After exposure and resist development, we can see that the resist on the center remained due to enough dosage for focused flux, while the resist on the edge region was removed due to much

lower dosage (Fig. 4.9c). This flux enhancement can be optimized and used for RIPEL, to further increase its throughput.

4.5 RIPEL alignment technology

Alignment of a mask to alignment marks on a wafer from a previous lithography steps is crucial. We develop a method of using grating alignment marks as shown in Figure 4.10a. The reflected diffraction pattern will be imaged by a CCD. If the alignment and the wafer gratings are aligned, the diffraction pattern will be ideal with well-defined nulls for intensity on different diffraction orders. For example, symmetric light measurement on the two +1 and -1 lobes of the diffracted pattern being balanced on a quad-photodiode would provide a very accurate assessment of symmetrical placement of the two gratings.

Working mechanism of gratings for alignment: The lamellar gratings can be treated as two sets of mirrors, where each set of strip mirrors consist of 1D photonic crystal with identical rectangular, long apertures. The two reflected waves from the two identical arrays of strip mirrors, only have a phase difference φ between them. This phase relationship is manifested as an intensity change in the zeroth-order diffracted light. Figure 4.10b shows the optical sensing mechanism. For normal incidence, the optical intensity of a selected diffraction beam can be obtained by [52]:

$$I \propto \left(\frac{\sin K}{K}\right)^2 \left[\frac{\sin(2NK}{\sin(2K)}\right]^2 \cos^2(\frac{\varphi}{2}) \tag{4.1}$$

where $K = (\pi d / 2\lambda)\sin\alpha$, λ is the incident wavelength, d and N are the grating period and the number of illuminated periods, respectively. The diffraction angle α and the phase difference φ are given as follows:

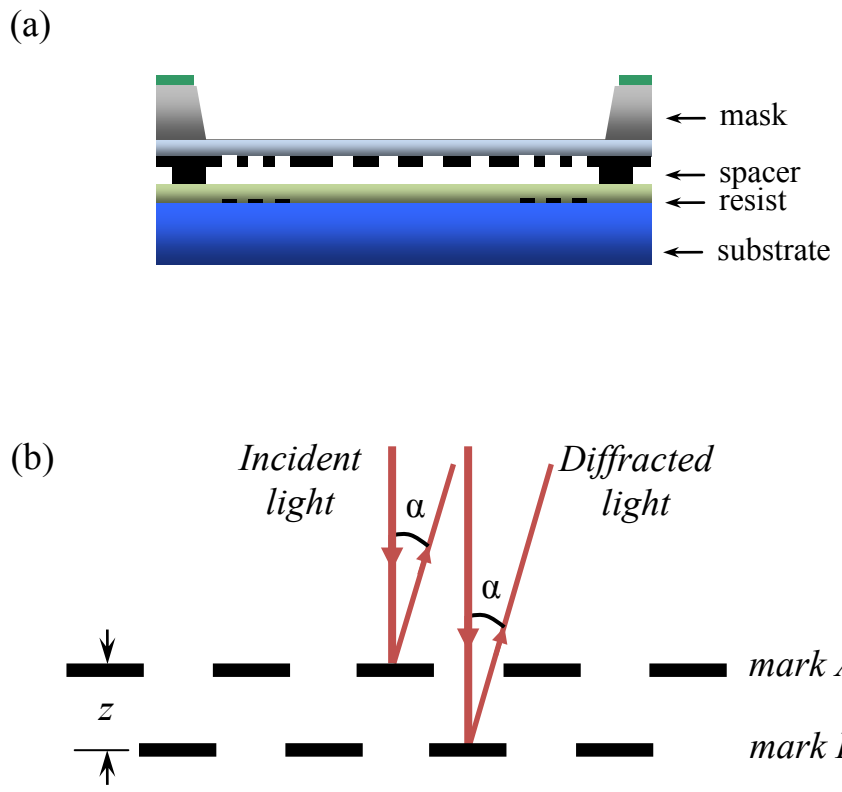

Figure 4.10: (a) Schematic drawing for mask alignment process, using spacer to determine the gap between the mask and the resist. (b) Schematic drawing for the alignment mechanism, using lamellar gratings to determine the gap.

$$\alpha = \arcsin\left(\frac{m\lambda}{d}\right), \qquad \varphi = \frac{2\pi}{\lambda}\delta \tag{4.2}$$

where m is the diffraction order, and

$$\delta = z\left(1+\cos\alpha+\frac{d}{2z}\sin\alpha\right) \tag{4.3}$$

is the optical path difference due to the facet offset z between two sets of light-reflecting beams. If we consider the zeroth order, i.e. $m = 0$ and $\alpha = 0$, the optical intensity is then proportional to

$$I \propto N^2 \cos^2\left(\frac{2\pi z}{\lambda}\right) \tag{4.4}$$

From equation 4.4, the optical intensity is highly sensitive to the grating offset z. For instance, if we use a laser beam of wavelength 680 nm, a small displacement of 170 nm (one quarter of the wavelength) is enough to turn the sensor output from maximum to minimum.

An incident laser beam onto the lamellar gratings will result in multiple diffracted beams reflected back. Picking out only the zeroth-order diffracted beam involves the use of an appropriately placed aperture. An amplitude modulated intensity profile is obtained which corresponds to the gap distance between mask A and mask B (Fig. 4.10b).

Alignment marks fabrication: 3-inch Si wafer was used. Photoresist buffer layer LOR3A was spun onto the wafer, with spinning rate of 4000 RPM for 30 seconds, followed by a prebake at 180 ^{o}C for 5 mins. Then the photoresist layer S1805 was spun on top, with spinning rate of 3000 RPM for 60 seconds, followed by a prebake at 115 ^{o}C for 60 seconds. ABM contact aligner was used for optical lithography exposure (12 seconds), followed by a normal development process in MIF 321 solution for 30 seconds. Then a thin layer of Ti/Ni (5nm / 25nm) was deposited by metal evaporator, followed by a lift off process in acetone. Finally, the LOR layer was removed by MIF 321 solution for 90 seconds.

Experiments: 4-inch RIPEL mask was fabricated using micro/nano machining technology (Fig. 4.4). Then a 3-inch Si wafer, which has pre-defined alignment marks, was coated with a thin layer (~70 nm) of negative e-beam resist NEB31A. The experimental set up for RIPEL with alignment was shown in figure 4.11. The mask-wafer

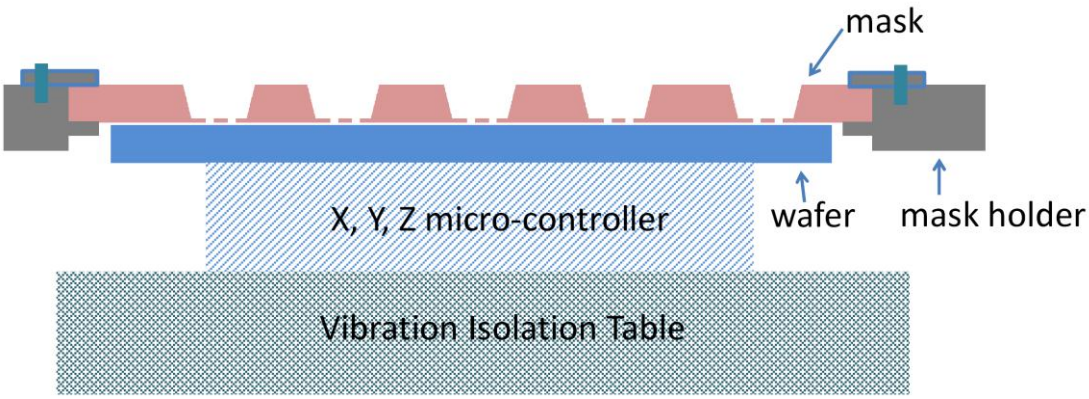

Figure 4.11: Schematic plot for experimental set up.

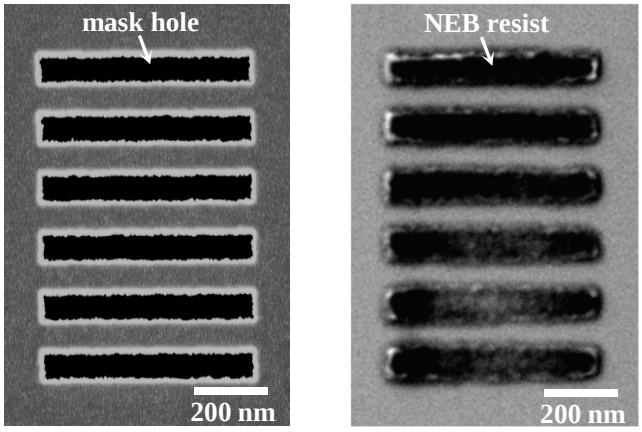

Figure 4.12: SEM images of the mask (left) and its corresponding NEB resist pattern by RIPEL.

gap was determined by a pre-defined spacer on the mask (Fig. 4.10a). This spacer (~100 nm thick) was formed by an optical lithography and tungsten RIE etching step. After this spacer fabrication, then e-beam lithography was used to define the tiny feature size patterns on the mask. The alignment process was similar to an optical contact aligner. Optics was used to locate the cross-marks (Fig. 4.1) on the membrane mask. Then the 3-

inch substrate wafer sitting on the stage was carefully moved and adjusted by the X, Y, Z micro-controllers, to make sure that the cross-marks on substrate wafer (the same shape with the cross-marks on mask) overlay with those on the membrane mask. After ^{63}Ni

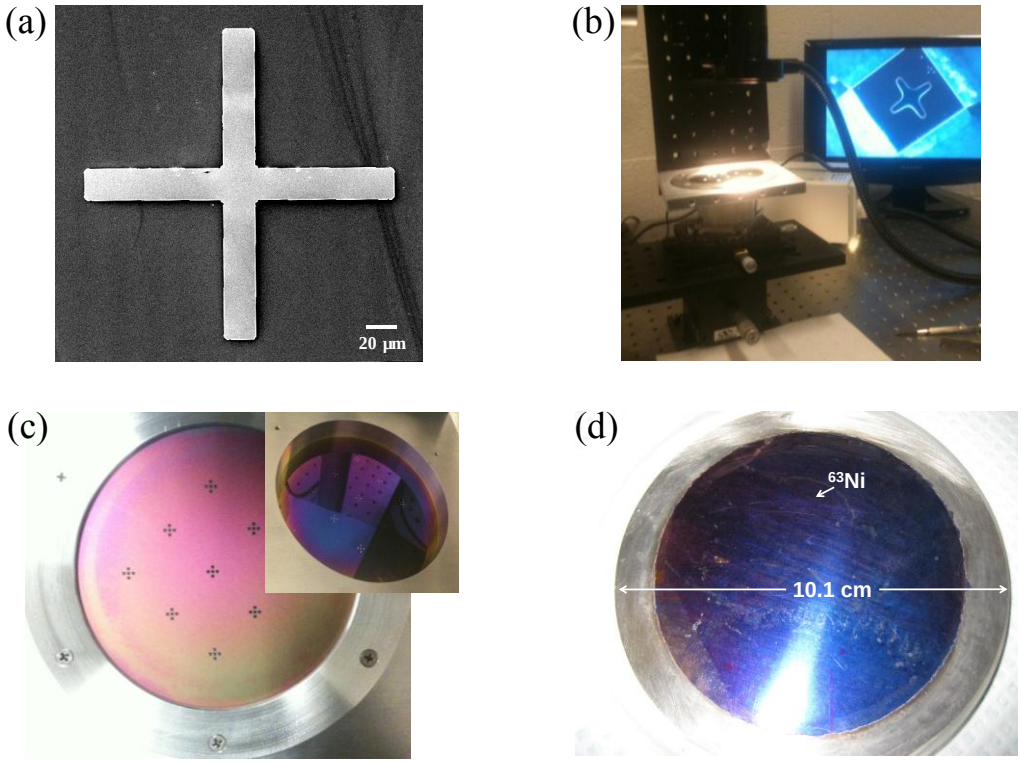

Figure 4.13: (a) SEM image of the alignment marks used in RIPEL. (b) Photo image of the set-up of RIPEL with alignment. (c) Photo image of the 4-inch mask (back side) in mask holder. Inset shows the photo image of its front side. (d) Photo image of the 4-inch ^{63}Ni source.

Table 4.1: Parameters for RIPEL experiments with alignment.

mask size	wafer size	Mask-wafer gap spacer	Simulated resolution (70 nm line mask)	Exp. resolution	Lateral Align. Error
4 inch	3 inch	100 nm	90 nm	110 nm	1~5 μm

continuous exposure for 96 hours, the resist was developed using normal NEB31A resist development recipe. From the SEM images (Fig. 4.12), the smallest feature size of 110

nm was achieved by a 70 nm line-featured mask.

Potential future improvements: This was the preliminary experimental demonstration for RIPEL with alignment. The alignment and exposure could be improved by following methods:

1). Nano-positioning stage with 6-axis controlled movement would improve the wedge compensation for in the alignment. Currently, 100-nm spacer was used to determine the gap between mask and wafer. The spacer will contact with both the mask and the wafer, leading to potential wafer bending errors due to the contact force. The wafer bending would introduce non-uniform mark-wafer gap. Therefore, in current preliminary exposure experiment, only a small portion of area showed expected resist pattern, while the rest areas showed blurred patterns due to the diffraction effect from the not-well-controlled wafer-mask gap.

2). Lateral alignment error value in Table 4.1 could also be improved by using more accurate nano-positioning stage. This alignment error was estimated by mismatched position values of the second alignment marks read from the CCD image.

3). Clean room environment is needed to improve the reusability of the mask for RIPEL. The diameters of air dust particles are typically in the range of hundreds of nanometers to several micrometers. These particles could be attached to the mask, when the mask is kept in air environment for more than several days. These particles are large enough to block some of the tiny features (less than 100 nm) on the mask. Moreover, if some large particles are attached to the front side of the mask, they could affect the gap between the mask and the resist in the alignment process.

CHAPTER 5

RIPEL APPLICATION IN SOLAR ENERGY HARVESTING

5.1 Background and motivation

A solar cell [53] (or photovoltaic cell) is a device that converts the energy of light directly into electricity by the photovoltaic effect. Assemblies of solar cells are able to capture energy from sunlight. The photovoltaic effect is the creation of voltage or electric current in a material upon exposure to light. In a photovoltaic effect process, electrons are transferred between different bands (i.e., from the valence to conduction bands) within the material, leading to the buildup of voltage between two electrodes. For example, a p-n junction solar cell works in three steps. First, incident sunlight is absorbed by semiconducting materials, such as silicon. Second, the absorbed photons will generate a large number of free electrons and holes, which will diffuse inside the materials. Third, the built-in electric field of the depletion region of the p-n junction will separate the generated free electrons and holes, leading to built-up voltage[53].

Currently, the big challenge of solar sell application is how to further reduce its cost. Solar cells with lower material cost are of interest to decrease the cost of solar energy. By far, the mostly used bulk material for solar cells is crystalline silicon (c-Si). Manufacturers of wafer-based cells have responded to high silicon prices in 2004-2008 prices with rapid reductions in silicon consumption. Therefore, thin-film solar cell that can reduce material cost, is becoming next generation technology to enable low-cost solar energy harvesting.

Nano-structured silicon thin film solar cells are promising, due to the strongly

enhanced light trapping, high carrier collection efficiency, and potential low cost. Solar cells with Si nanowire (Si NW) arrays incorporating radial p-n junctions not only have antireflective, broad band optical absorption properties but also offer the advantage of orthogonalizing the light absorption and carrier collection processes, which is the challenging problem for bulk Si solar cells [54-57]. Previously, single SiNW radial p-n junction solar cells, using vapor-liquid-solid NW growth, were reported [58]. This single NW solar cell had a low open circuit voltage (V_{oc}), possibly due to the p-i-n structure, resulting in low overall solar cell efficiency of less than 3.4%. Large-area solar cells based on Si NW were reported using Au catalytic chemical vapor deposited (CVD) p-type Si NW, followed with a plasma-enhanced CVD conformal n-type amorphous silicon (a-Si:H) layer to create the photoactive p-n junction [59]. These solar cells showed very low conversion efficiency (~0.1%), particularly due to the geometry of the NWs with random and uncontrolled NW orientation and varied NW diameter distribution. Recently, large-area solar cells from arrays of silicon NW with radial p-n junctions were shown[60, 61], using an aqueous suspension of silica beads to get a close-packed monolayer, followed by deep reactive ion etching to form NW and boron diffusion to form the radial p-n junction. By reducing surface roughness and improving the NW diameter and density control, the solar cell efficiency was enhanced significantly from initially 0.5% to as high as 5.3%. But its overall efficiency is still not high for practical application, probably due to the imperfect NW spacing, and absence of any surface passivation. Calculations have showed that with optimized wire spacing, diameter, and wire height, vertical Si NW array solar cells with photonic crystal architecture could offer conversion efficiency as high as 24% or more [62], due to photonic crystal optical absorption enhancement effect with the

presence of optical guided resonance modes [62-64]. Moreover, theoretical study also shows that ordered Si NW structures with small variations in the radius of the wires could create additional resonant modes at other frequencies not present in the perfectly ordered structures, leading to broad band solar-energy harvesting [65]. Amorphous silicon nanocone arrays were demonstrated to have enhanced optical absorption in the 400-700 nm wavelength range [66], but they are hard to apply to high-performance thin film solar cells due to the random nanocone spacing and wide cone size distribution.

The fabrication of large-area ordered controllable Si nanostructure arrays needs top-down planar lithography with both high throughput and high resolution. Conventional optical lithography has high throughput, but its critical dimension is limited to a fraction of the wavelength. Traditional electron beam lithography has the highest resolution <10 nm, but it suffers from high cost and low throughput due to the required electron beam raster scanning serial exposure. Nanoimprint lithography could be used to achieve nano-structured arrays, but the prospect of mask mechanical contact to substrate leads to a large number of defects and short mask life [31]. Our recently reported nanolithography system RIPEL [34, 67], using large-area planar radioactive beta-electron thin film emitters to parallel expose e-beam resist through a stencil mask, demonstrated sub-35 nm resolution. Using naturally emitted high-energy beta particles, the RIPEL system can be compact as the electron focusing column needed in electron beam lithography is no longer needed. Elimination of vacuum in RIPEL will significantly simplify the overall lithography system and greatly reduce the cost, while enabling large area massively parallel high-throughput electron lithography with high resolution. Here, we successfully used RIPEL to fabricate a novel ordered Si nano-conical-frustum (NCF) array structure,

which exhibits an impressive absorbance of ~99% (upper bound) over wavelengths 400-1100 nm with a thickness of only 5 μm. Moreover, high-efficiency (up to 10.8%) solar cells have been demonstrated, by using these ordered Si NCF arrays.

5.2 Nano-structure array fabrication by RIPEL

Figure 5.1 shows the schematic illumination of the fabrication processes for ordered NCF arrays. A thin layer of plasma-enhanced chemical vapor deposition (PECVD) silicon dioxide (200 nm thick) was deposited on a silicon on insulator (SOI) (Si (5 μm)/SiO_2 (2 μm)/Si stack) wafer substrate. RIPEL was used to pattern the e-beam resist, and the pattern was transferred to SiO_2, using SiO_2 reactive ion etching (RIE). Ordered Si NCF arrays were formed, using silicon angled RIE etching recipe, with SiO_2 as the etching mask. Ordered Si NCF arrays with different slant angles can be obtained, depending on the reactive ion etching conditions (Supporting Information). Figure 5.2 shows the scanning electron microscopy (SEM) images of two types of NCF arrays, with different slant angles, using the same ordered SiO_2 post arrays as the etching mask. The first NCF arrays (Fig. 5.2 a, b) have 170 nm of top radius (r_1), 400 nm of base radius (r_2), 3.5 μm of height (h), 3.8 ° of slant angle (θ), and 800 nm of lattice constant. The second (Fig. 5.2 c, d) type have 170 nm of equal top and base radii, height of 3.5 μm, 0 ° slant angle, and 800 nm lattice constant, which we name ordered quasi-nanowire (QNW) arrays. In experiments, the top radii and the lattice constant were controlled by RIPEL mask design. The slant angle and height are determined by the silicon RIE etching condition and etching time, respectively. The bases of all the adjacent NCFs were connected (Fig. 2b right), while the bases of the adjacent QNWs were apart from each other (Fig. 2d).

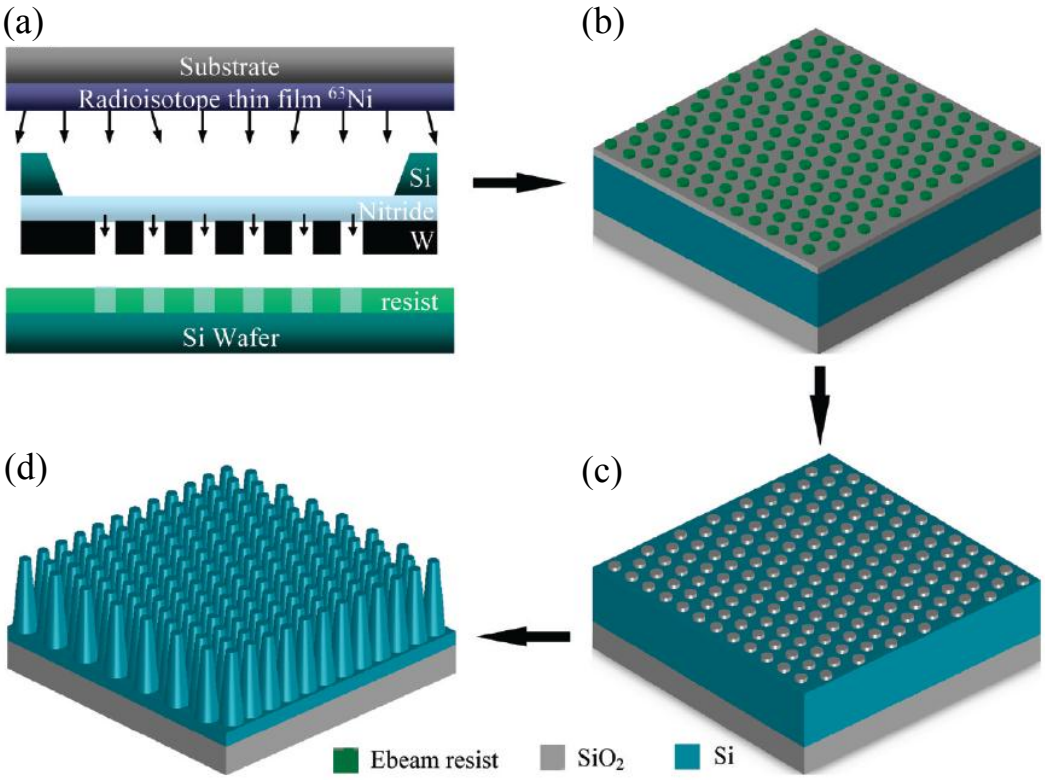

Figure 5.1: Schematic drawings for ordered Si NCF arrays, fabricated by RIPEL. (a) Cross section schematic drawing for RIPEL experimental setting up, using large-area planar radioactive beta-electron thin film emitters (top) to parallel expose e-beam resist (bottom) through a stencil mask (middle). Using nature's high-energy particle, RIPEL potentially enables large-area massively parallel high throughput electron lithography with low cost, while maintaining sub-35 nm resolution. (b) Electron resist is patterned on stack substrate SiO_2 (0.2 μm)/Si(5 μm)/SiO_2(2 μm)/Si, by RIPEL. (c) Pattern is transferred to SiO_2 layer by oxide RIE etching, using ebeam resist as the etching mask. (d) Ordered Si NCF arrays are formed by Si RIE etching, using SiO_2 as the etching mask. The bottom Si substrate of the SOI wafer is not shown here.

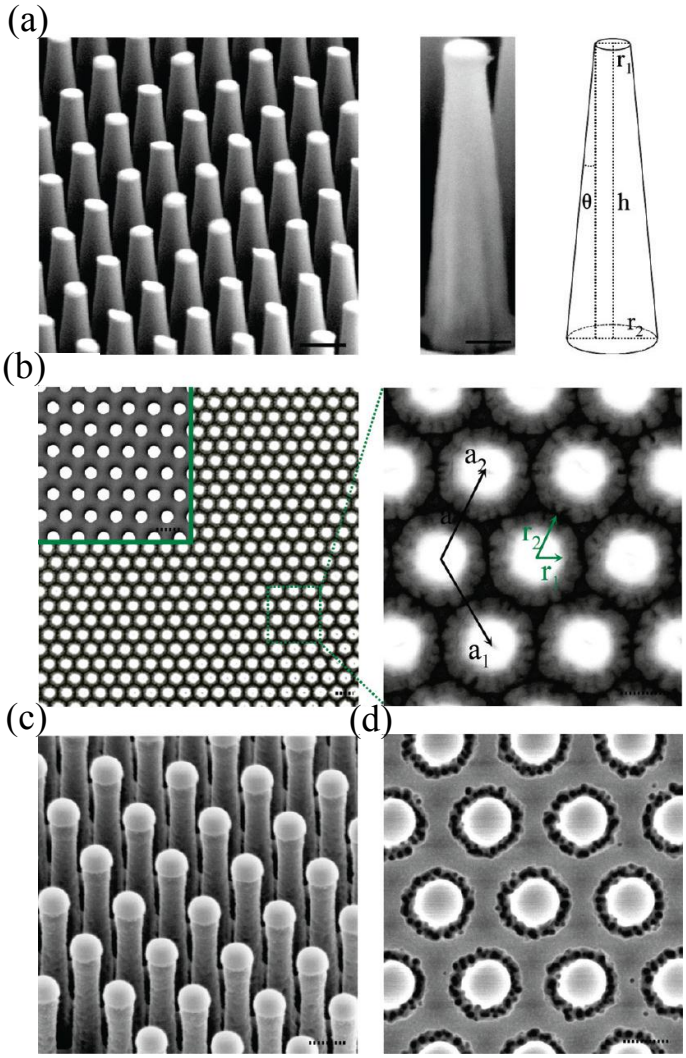

Figure 5.2: Microscopy images of ordered Si NCF arrays and the ordered quasi-nanowire (QNW) arrays. (a) Left part shows the side view (45 °) SEM image of the ordered Si NCF arrays, with scale bar 800 nm. The zoom in SEM image (45 ° side view) of a single NCF is shown on right, with 170 nm of top radius (r_1), 400 nm of base radius (r_2), 3.5 μm of height (h), and 3.8 ° of slant angle (θ). The scale bar is 400 nm. (b) Top view SEM images of the ordered Si NCF arrays (left, 800 nm scale bar) and the zoom in SEM image (right, 400 nm scale bar). Inset shows the SEM image of the corresponding etching mask SiO_2 post arrays (800 nm scale bar). a_1 and a_2 are the lattice vectors, with lattice constant a. The bases of the adjacent NCFs are connected, with 800 nm of lattice constant and 400 nm of NCF base radius. (c) Side view (45 °) SEM image of the ordered Si QNW arrays, with scale bar 400 nm. (d) Top view SEM image of the ordered Si QNW arrays in (d), with scale bar 400 nm.

5.3 High-efficiency light-trapping for nano-structure array

The transmitted diffraction pattern of the ordered Si NCF arrays (800 nm lattice constant) using λ = 609 nm laser (Fig. 5.3 a), shows the high periodicity and uniformity of the nanostructures. The reflection and transmission spectra are shown in parts c and d of figure 5.3, respectively. In order to get the membrane window for transmission measurements, the SOI wafer was backside etched through, by Si deep reactive ion etching (DRIE), using 4 μm of PECVD SiO_2 as the etching mask and the buried oxide (2 μm) as an etch stop. The window membranes consist of 3.5 μm of ordered Si NCF arrays (or QNW arrays), 1.5 μm of planar Si layer underneath and 2 μm of the SOI buried oxide. The control sample made of bare silicon membrane has a thickness of 5 μm planar Si and 2 μm of the SOI buried oxide. We obtained absorption (*A*) spectra (Fig. 3e) after acquisition of reflection (*R*) and transmission (*T*) spectra, by $A = 100\% - R - T$. The ordered Si NCF arrays exhibit maximal absorbance of ~99% (upper bound) over wavelengths 400-1100 nm. A small part of diffusely reflected light was not included in the reflection measurements, due to the experimental setup limitation. Therefore, the absorption spectra represent an upper limit.

In order to investigate the light trapping properties as a function of lattice constants, we fabricated three kinds of ordered NCF arrays with the same height (3.5 μm) and constant slant angle ($\theta = 3.8°$), but with different lattice constants, 600 nm (r_1 = 69 nm, r_2 = 300 nm), 800 nm (r_1 = 170 nm, r_2 = 400 nm), and 1000 nm (r_1 = 273 nm, r_2 = 500 nm) on the same SOI wafer. The reflectance spectra are shown in figure 5.4 a. The ordered NCF arrays with 600 nm lattice constant give the lowest reflectance

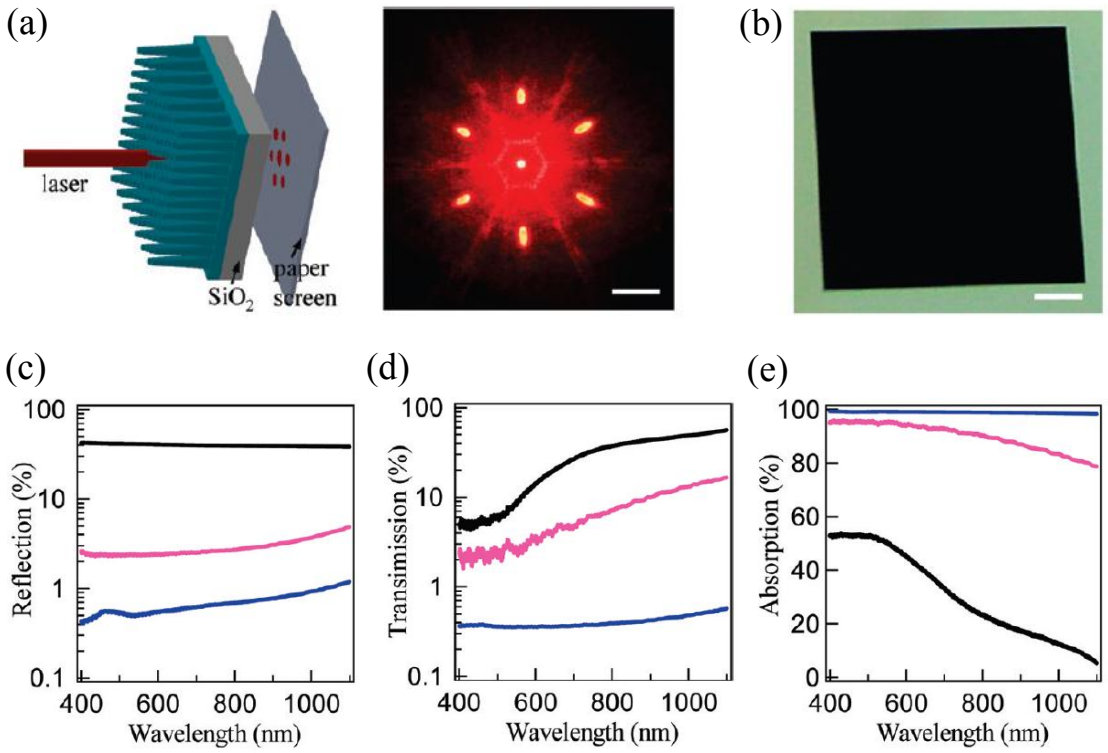

Figure 5.3: Light trapping measurements. (a) Transmitted diffraction pattern of the NCF arrays (800 nm lattice constant) using a λ = 609 nm laser, projected onto a white paper screen and taken by digital camera. The paper screen is 4 mm away from the SiO_2 substrate. Scale bar is 3 mm. The window membranes consist of 3.5 μm of ordered Si NCF arrays, 1.5 μm of planar Si layer underneath and 2 μm of the SOI buried oxide. (b) Photograph of the ordered Si NCF arrays, with scale bar 1 mm. Parts c, d, and e show the measured reflection, transmission, and absorption spectra, respectively, for light normally incident on the ordered Si NCF arrays (blue), ordered Si QNW arrays (pink), and control bare silicon (black). The window membranes consist of 3.5 μm of ordered Si NCF (or QNW) arrays, 1.5 μm of planar Si layer underneath and 2 μm of the SOI buried oxide. The control bare silicon has a thickness of 5 μm.

(< 0.5%), due to the smallest top radius for minimal reflectance, which are consistent with expectations from theoretical predictions. All these three NCF samples show strong antireflective properties throughout the spectral range, which are consistent with the "black surface" (Fig. 5.3b). Both the ordered NCF arrays with lattice constants of 800 nm

and of 1000 nm show ultralow transmittance spectra (Fig. 5.4 b) throughout the spectral range 400-1100 nm, while the ordered NCF arrays with 600 nm lattice constant show slightly increasing transmittance for the wavelength near the band gap region 800-1100 nm.

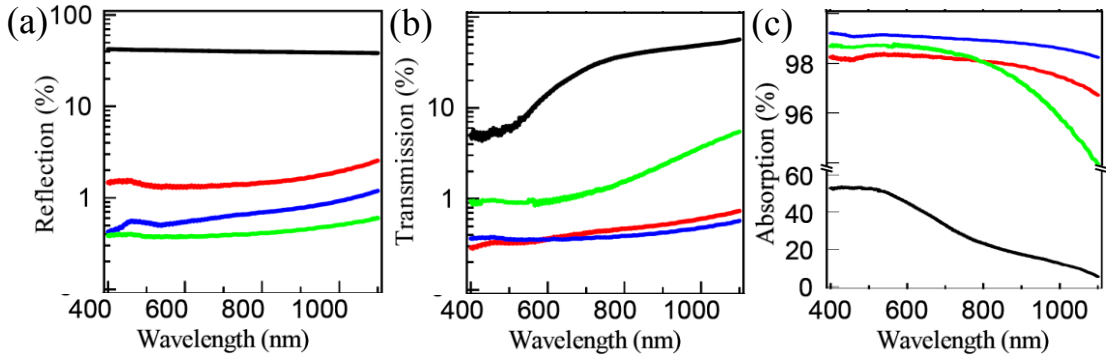

Figure 5.4: Experimentally measured reflection (a), transmission (b) and absorption (c) spectra for light normally incident on the ordered Si NCF arrays. Four types of samples were measured: bare silicon (5 μm thick) (black), NCF arrays with lattice constants of 600 nm (r_1 = 69 nm, r_2 = 300 nm, green), 800 nm (r_1 = 170 nm, r_2 = 400 nm, blue), and 1 μm (r_1 = 273 nm, r_2 = 500 nm, red). All the window membranes consist of 3.5 μm of ordered Si NCF arrays, 1.5 μm of planar Si layer underneath and 2 μm of the SOI buried oxide.

5.4 High-efficiency nano-structured solar cells

Due to the maximal absorption throughout the spectra range, the ordered Si NCF arrays with 800 nm lattice constant were selected for solar cells fabrication, to see the solar energy conversion efficiency. The radial p-n junction was formed via boron ion implantation (E = 10 keV), starting with n^+-type ordered Si NCF arrays fabricated using SOI top silicon (resistivity 0.015 Ω·cm, doping concentration 2×10^{18} cm^{-3}). Ion implantation offers the advantage of precise control over the total dose of dopants, depth profile, and most importantly works well also for high doping levels of the order of 10^{19}-

10^{21} cm^{-3}. Considering the slant angle (3.8 °) of the NCF, the sidewall implantation depth was estimated to be 20 nm, using the lateral straggling depth value calculated from SRIM ion implantation simulator. The initial doping concentration on the NCF sidewall surface was controlled to be 1×10^{20} cm^{-3} during the ion implantation. Rapid thermal annealing (RTA) at 900 ℃ for 60 s was used directly after implantation to activate the dopants and remove the implantation damage. In order to minimize the loss from the surface recombination coming from the large total surface area increased by NCF array geometry, a thin layer (~20 nm thick) of SiO_2 wet oxide was formed as the outside passivation layer for the p-n junction, at 900 ℃ for 6 min. During the RTA and wet oxidation high temperature processes, the boron dopants diffused toward the core by approximately 80 nm more, estimated from literature [68], offering a final junction depth of 100 nm and final boron doping concentration of 2×10^{19} cm^{-3} after the diffusion. From

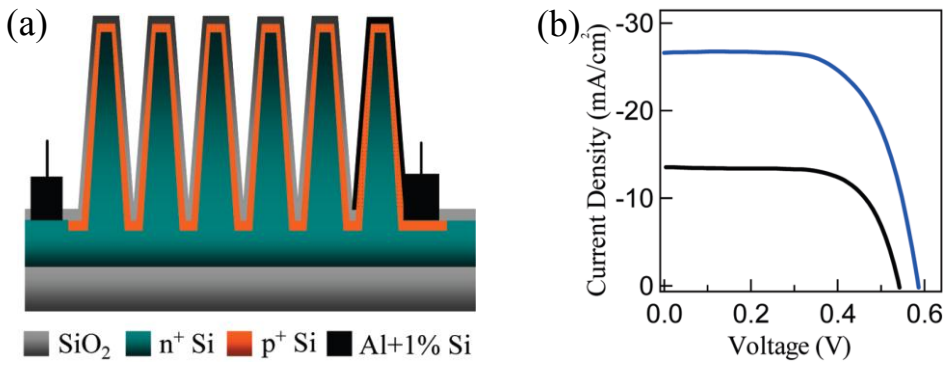

Figure 5.5: Solar cell output characteristics. (a) Cross section schematic drawing of the solar cell structures. (b) Current density vs. voltage curves for the solar cells consisting of bare silicon (black), Si NCF arrays with 800 nm (blue), under AM 1.5G normal illumination.

outer surface to the core center, the radial p-n junction consists of 20 nm of outside passivation SiO_2, 100 nm of quasi-neutral boron-doped p^+ type shell region, 25 nm of

depletion inter shell region, and 45 nm top radius (275 nm base radius) of quasi-neutral n^+ type Si core region (in radii). It is important to use both heavily doped n^+ and p^+ quasi-neutral region to make a small depletion region in each NCF, so that the NCF is not fully depleted, since the quasi-neutral core region should exist to conduct carriers down to the bottom contact. The schematic solar cell structure plot is shown in figure 5.5a.

Figure 5.5b shows representative current density versus voltage measurements of the individual solar cells, under AM 1.5G normal illumination of 100 mW/cm^2 at room temperature. For the solar cells with only controlled bare Si and with ordered Si NCF arrays (800 nm lattice constant), they had short circuit current densities (J_{sc}) of 13.6 and 26.4 mA/cm^2, open circuit voltages (V_{oc}) of 0.54 and 0.59 V, fill factors (FF) of 0.71 and 0.69, and efficiencies (η) of 5.2 and 10.8%, respectively. The high energy conversion efficiency of the ordered Si NCF arrays is due to the strong light trapping and absorption properties throughout the spectra range, with the presence of both photonic crystal enhancement effect and radii-variation-induced broad band absorption. Although these NCF structure arrays have high light absorption efficiency, the solar cell efficiency is still less than half of that for bulk crystalline Si solar cells [69] and the open circuit voltage and fill factor are lower too. This is probably due to the high surface recombination losses, which are introduced by the highly enhanced surface area from the nanostructures, although a thin passivation oxide layer was used.

5.5 Summary

In summary, a novel large-area ordered silicon NCF array structure, exhibiting an impressive absorbance of ~99% (upper bound) over wavelengths 400-1100 nm with a

thickness of only 5 μm, is demonstrated by using the RIPEL technique that has the potential for very high lithography throughput, high resolution, and low cost. High-efficiency solar cells have been achieved using these ordered Si NCF arrays. Moreover, this novel high light-trapping structure array and the RIPEL fabrication technique can be also used for low-cost substrate solar cells, using poly-silicon or other semiconductors [70].

CHAPTER 6

RIPEL APPLICATIONS IN PHOTONIC CRYSTAL BASED NEMS

6.1 Introduction for photonic crystal

Photonic crystals are composed of periodic dielectric or metallo-dielectric nanostructures that affect the propagation of electromagnetic waves, which is in the similar way as the periodic potential in a semiconductor crystal affects the electron motion by defining allowed and forbidden electronic energy bands [71]. Photonic crystals contain periodic

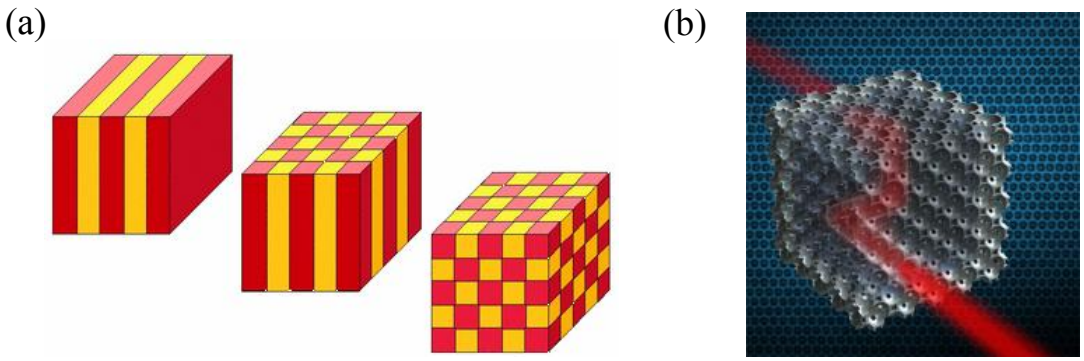

Figure 6.1: Schematic for photonic crystals. (a) Photonic crystals are arrangements of two or more dielectric media, periodic along one, two, or three dimensions. This is depicted schematically here by "red" and "yellow" materials arranged in simple 1d/2d/3d lattices from left to right. (b) A three-dimensional silicon structures that can manipulate and trap light could lead to all-optical integrated circuits. (Images are cited from websites: http://www.core.org.cn/OcwWeb/Mathematics/18-325Fall-2005/CourseHome/index.htm and http://www.technologyreview.com/Infotech/20036/?a=f).

internal regions of high and low dielectric constant, periodic along one, two, or three dimensions (Fig. 6.1a). Photons propagate through this structure - or not - depending on their wavelength, leading to guiding of light (Fig. 6.1b). The groups of light wavelengths

that are allowed to travel, form bands spectrum in the photonic crystal, whole disallowed bands of wavelengths are called photonic band gaps.

Photonic crystal Si nanowire (NW) arrays vertically aligned to the substrate demonstrate broad-band optical absorption due to strong light trapping by multiple scattering of the incident light [55]. The optical properties of the photonic crystal Si NW structures are highly dependent on the typical geometric factors, including wire diameter, length, and periodicity. In particular, photonic crystal nano-cone (NC) array (tapered nanowires) further suppresses the Fresnel reflection over a broad wavelength range at various angles of incidence, due to the gradual transition in the effective refractive indexes across the air-to-wire interface [66, 72]. Figure 6.2 show an effective refractive index profile calculated by averaging the refractive indices of air (n = 1) and a-Si:H (n = 4.23) weighted by volume at the interface between air and an a-Si:H thin film (Fig. 6.2a), between air and a-Si:H NW arrays (Fig. 6.2b), and between air and a-Si:H NC arrays (Fig. 6.2c). The effective refractive index changes immediately from 4.23 to 1 across the flat film interface (Fig. 6.2a), leading to large reflection of light. For a-Si:H NW arrays (Fig. 6.2b), the refractive index of the a-Si:H NW array depends on the density of the NWs, but they always provide an intermediate refractive index step, leading to reduced reflection over a broad range of wavelengths and angles of incidence. Interestingly for the a-Si:H NC arrays, the diameter of these NCs shrinks gradually from the root to the top, resulting in a graded transition of the effective refractive index. For this reason, the a-Si:H NC arrays would demonstrate the best antireflective properties and so the greatest absorption enhancement [66].

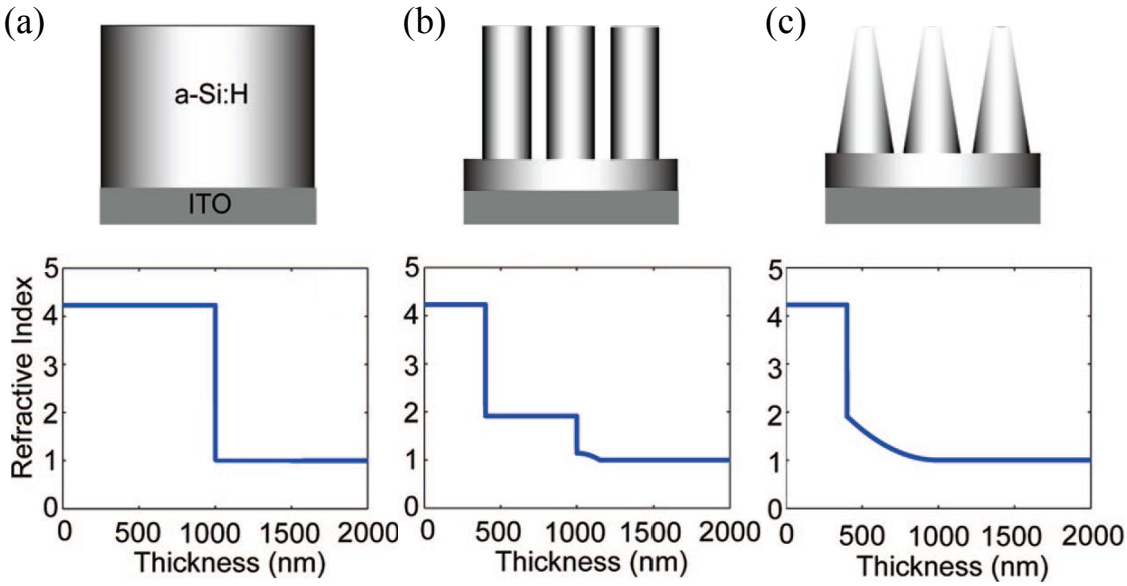

Figure 6.2: The effective refractive index profiles of the interfaces between air and (a) 1 μm thick a-Si:H, (b) 600 nm a-Si:H nanowire (NW) arrays and (c) 600 nm a-Si:H nano-cone (NC) arrays, on ITO-coated glass substrate. Results are cited from previous report [66].

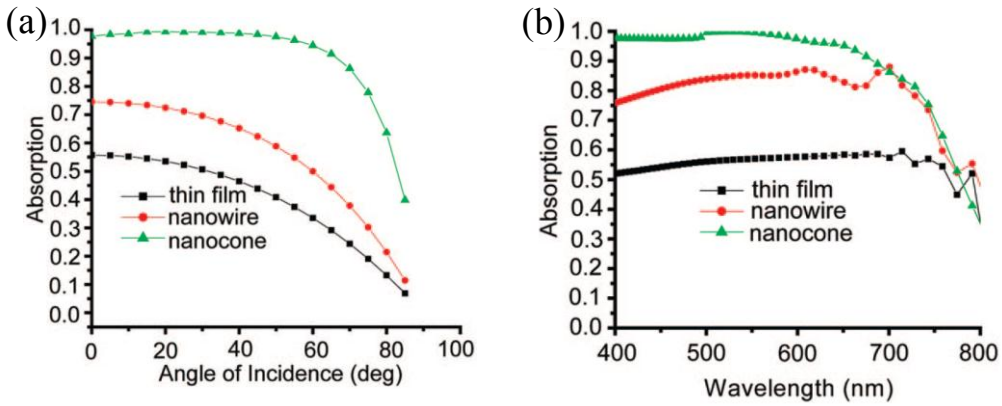

Figure 6.3: (a) Simulated value of absorption on samples with a-Si:H thin film, NW arrays, and NC arrays as a top layer over different angles of incidence (at wavelength λ = 488 nm).(b) Calculated value of absorption on a-Si:H thin film, NW sample, and NC sample over a large range of wavelengths at normal incidence. Image results are cited from previous report [66].

From previous report [66] regarding the numerical comparison, the Maxwell equation was solved with rigorous coupled-wave analysis (RCWA) method. This frequency-domain method is able to simulate the dispersive materials with tabulated dielectric constant data from experiments. In the simulation, a plane wave was incident on the periodic nano-patterned a-Si:H structure. The transmitted and reflected waves were calculated, from which the absorption of the structures was derived.

6.2 Photonic crystal based all-optical pressure sensor

An all optical pressure sensor has several advantages of being able to be used in harsh environments where wiring and electronics cannot be used. Optical pressure sensors can be interrogated at large distances using optical imaging and waveguide. To date, optical pressure sensors use air-gaps made using sacrificial etching under poly-silicon or dielectric films [73, 74]. Such sensors result in a gap that is also a function of temperature and has dynamic range limited by the gap. Most importantly, they are designed to be used with a specific wavelength of interrogating light.

Here, we realize an all-optical pressure sensor by fabricating controllable vertical silicon nanowire arrays on a Si/SiO_2 membrane. Vertical nanowire array acts as a photonic crystal and can affect the propagation of electromagnetic waves in the same way as the periodic potential in a semiconductor crystal affects the electron motion by defining allowed and forbidden electronic energy bands [75]. In our design, the light absorbing photonic crystal is formed laterally on a membrane with ordered vertical nanowires array. This eliminates the need for under-etching, and very high accuracy array can be formed using RIPEL. The photonic-crystal absorbs light over a wide wavelength

range enabling white-light interrogation. Higher dynamic range is realized as the nanowires can be moved out as the membrane is pressurized.

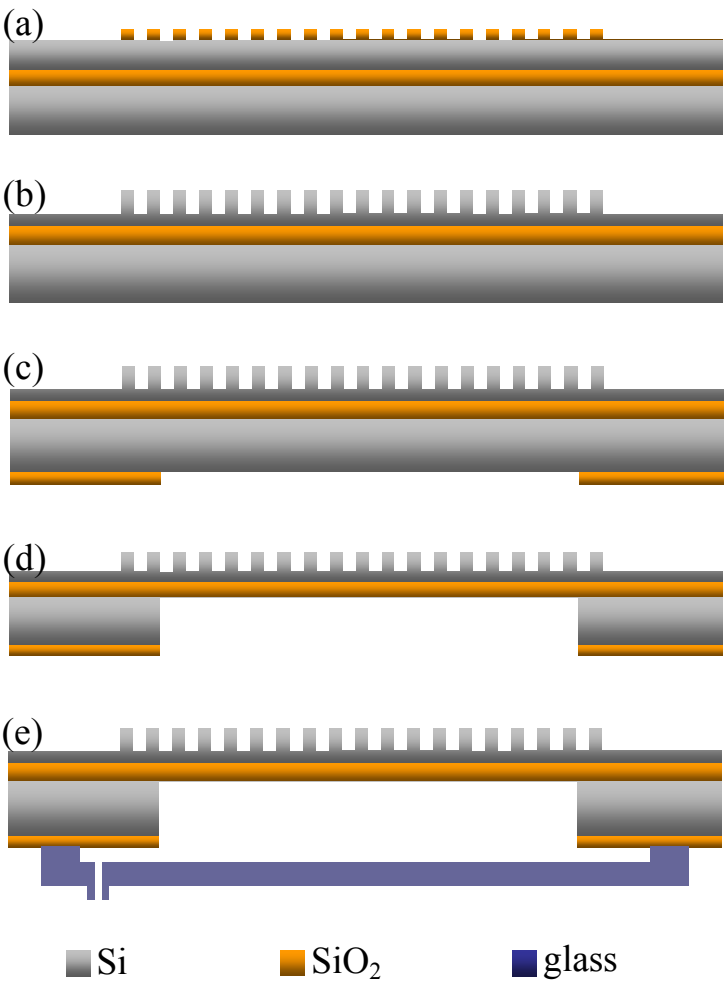

Figure 6.4: Photonic crystal based all-optical pressure sensor fabrication process schematic drawings. (a) A thin layer (~ 300 nm) of PECVD SiO_2 was deposited on SOI wafer (3 μm Si/ 2 μm SiO_2). The PECVD SiO_2 layer was patterned by electron beam lithography, followed by oxide RIE etching. (b) Vertical Si nanowire arrays were formed by Si RIE etching, using SiO_2 as the etching mask. (c) A thick layer (~ 4 μm) PECVD SiO_2 was deposited on back side of the SOI wafer. Then it was patterned by optical lithography EV620 using backside alignment, followed by SiO_2 RIE etching. (d) The SOI wafer Si substrate was etched through by Si deep RIE, using the back PECVD SiO_2 layer as the etching mask and the SOI buried oxide as the stopping layer. (e) A glass pressure controller adapter was mounted to the back by superglue.

We can use RIPEL to pattern the vertical silicon nanowire arrays, on a SOI wafer, by silicon reactive ion etching (RIE) using SiO_2 nano-posts as the etching mask. The vertical silicon nanowire array has 100 nm diameter wires, 1 μm pitch and 1.5 μm height (Fig. 6.4 and 6.5). These nanowire arrays show uniform wire diameter, controllable wire orientation and wire pitch spacing. Optical lithography with backside alignment was used to pattern the backside circular cavity (800 μm diameter), followed by silicon DRIE to etch through the silicon substrate using the SOI buried oxide as the stopping layer. The

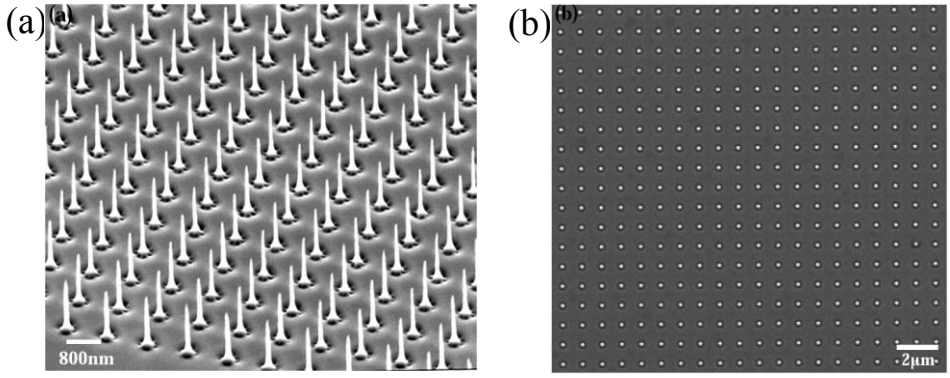

Figure 6.5: (a) SEM image (45° side view) of the vertical Si nanowire arrays, with 100 nm of wire diameter, 1 μm of nanowire pitch and 1.5 μm of nanowire height. (b)The top view SEM image of the SiO_2 posts arrays in figure 6.5a.

oxide layer on the silicon membrane has a built in compressive stress which when released after etch, results in a slightly wrinkled membrane as see in figure 6.6. The pressure sensor was mounted on a glass tube that was pressurized, applying pressure onto the membrane. By modulating the pressure, the photonic crystal nanowire structures reflect different patterns with spatially varying colors. Hence, instead of the displacement, the resulting color pattern is the pressure indicator. Our visual pressure sensor showed high sensitivity between 0 Pa up to $8x10^4$ Pa with 1-Pa resolution

determined by the cross-correlation with the CMOS imager used to measure the displacement. Given that the CMOS imagers have a sensitivity of $I_{read}[\lambda]$, we can

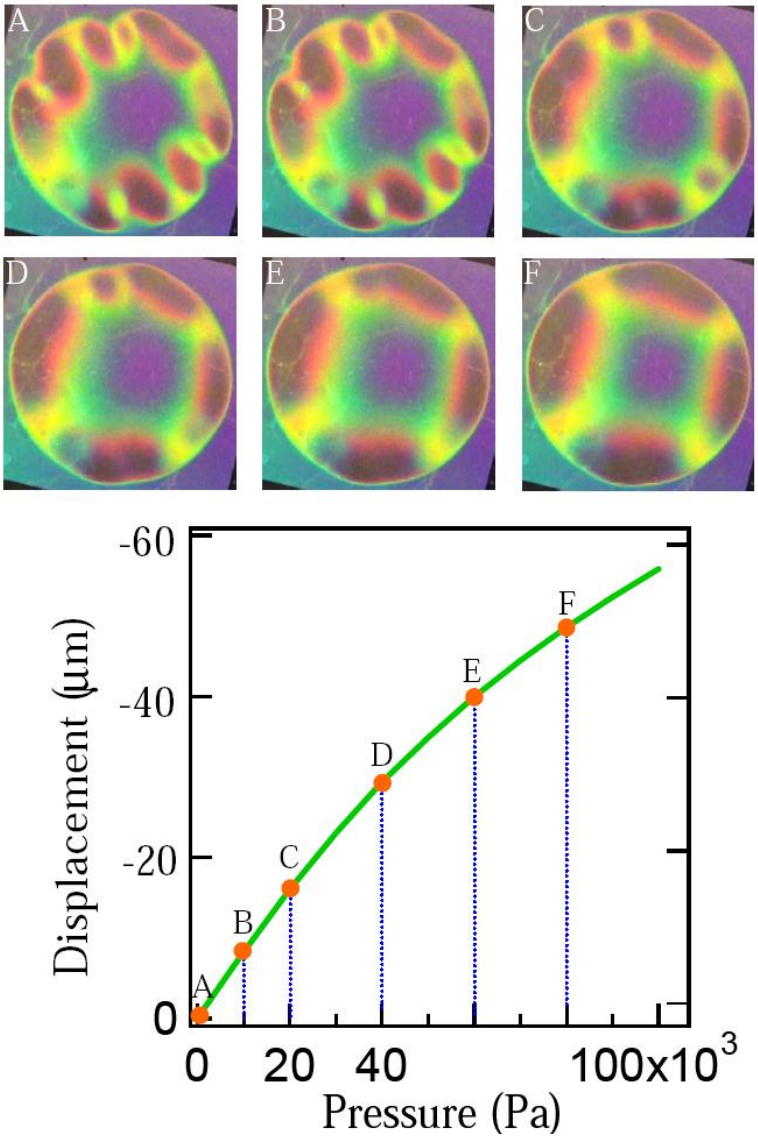

Figure 6.6: Visual pressure sensor experiment test and simulation. The circular membrane has 800 μm diameter and its load pressure is defined as the pressure difference between the outside pressure and the cavity pressure. (A)-(F) show the top-view photograph images of the nanowire membrane color change as increasing the membrane load pressure from 0 Pa up to $8x10^4$ Pa. The displacement corresponds to the maximum displacement of the center point of the circular membrane. The initial pattern is due to compressive stress in the Si/SiO_2 bilayer.

estimate $I_{read}[P]$ as 0.5 angstrom/Pa. With a current noise of 0.5 angstrom per pixel, we can estimate the pressure sensitivity of this sensor to be 1 Pa.

For a uniform circular membrane geometry, with a uniform pressure load p, the plate's deflection $z(r, p)$ in z direction as a function of radial position, r, plate radius, r_0, and the plate material's flexural rigidity, D, can be expressed as [76]:

$$z(r,p) = \frac{p \cdot r_0^4}{64 \cdot D}\left(1 - \frac{r^2}{r_0^2}\right)^2 \tag{6.1}$$

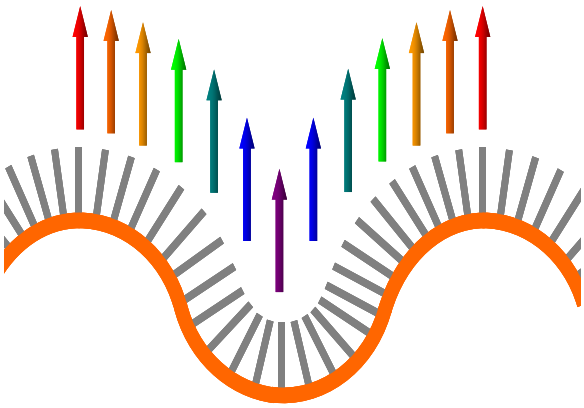

Figure 6.7: Schematic mechanism explanation for the light reflection from these photonic crystal vertical nanowire structures on deformed membrane. The bending of the membrane modulates the view angle of the nanowire arrays, resulting in wavelength dependent reflection. The arrows with different color correspond to the reflecting visible lights with different wavelengths.

Flexural rigidity is given by [77], where t is the plate effective thickness, and E and υ are the plate material's effective Young's modulus and Poisson ratio, respectively.

$$D = \frac{E \cdot t^3}{12 \cdot (1 - \upsilon^2)} \tag{6.2}$$

From equation 6.1, we see that the maximum plate deflection, which occurs at the plate's center (r = 0), can be expressed as：

$$z(p)_{\max} = \frac{p \cdot r_0^4}{64 \cdot D} \tag{6.3}$$

As the pressure changes, the membrane is deformed, and the nanowire deflection angle are changed leading to a nanowire reflectance modulation. The reflection wavelength shift $\Delta\lambda$ should be a function of the radial position, *r*, and the pressure load, *p*. It can be given by,

$$\begin{aligned} \Delta\lambda(r, p) &= a \cdot \sin[\tan^{-1}(-\frac{\partial(z(r, p)}{\partial r})] \\ &= a \cdot \sin[\tan^{-1}(\frac{p \cdot r_0^2 \cdot r}{32 \cdot D}(1 - \frac{r^2}{r_0^2}))] \end{aligned} \tag{6.4}$$

where *a* is the lattice constant of the photonic crystal nanowire arrays, and *p* is the membrane pressure load.

6.3 High-efficiency opto-thermo-mechanical MEMS excitation

The pulses of light, incident on a sample of matter, can be absorbed and converted to heat, leading to local thermal excitation and detectable acoustic waves. This kind of photo-acoustic effect continues to be applied in an increasing number of fields, such as photo-acoustic imaging in biomedicine [78], photo-acoustic spectroscopy in trace gas monitoring [79], optical actuation for MEMS devices [80], etc. Optical actuation for MEMS takes advantage of directly coupling photonic energy into selected device areas without any electrical interconnects as required in integrated electrostatic and piezoelectric actuation [81]. In opto-thermo MEMS actuation, light incident onto the structures is absorbed and converted to heat via photon absorption. Hence, the optical actuation efficiency is highly dependent on the material optical absorption efficiency.

Different materials and molecules will absorb photons to different extents at different optical wavelengths. For example, silicon has a reasonably high optical absorption efficiency in the visible light spectrum, while it is almost transparent to infrared (IR)

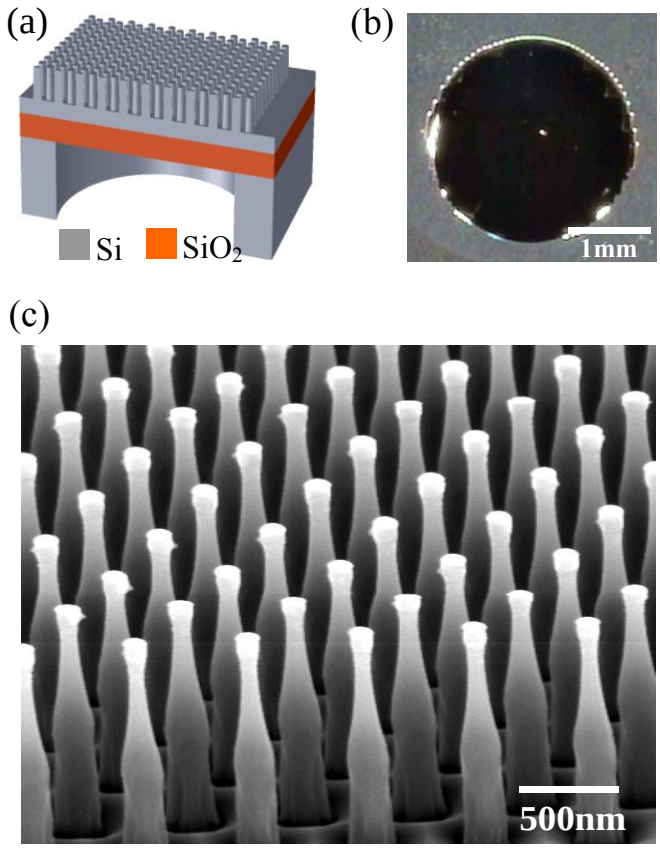

Figure 6.8: (a) Schematic of the Si/SiO_2 (1.5 μm / 2 μm) membrane with vertical Si nanopillar array. (b) Photo image (top view) of the backside circular cavity. (c) SEM image (60^o view) of the nanopillar arrays, with 1.5 μm height, 250 nm base diameter, 100 nm top diameter, at a 600 nm pitch.

light. Therefore, a system that could enhance light absorption at broad band wavelengths is required for high-efficiency broad-band optical MEMS actuation. Thin film vertical silicon nano-pillar arrays with photonic crystal structure has been demonstrated to have highly enhanced light trapping and broad-band (from UV to near IR) optical absorption

efficiency [66, 82]. Here, we present the first-ever opto-thermal-mechanical MEMS actuation for membrane resonator, using photonic crystal nanopillar arrays on top of membrane as the optical absorbers. This optical actuation for MEMS takes advantage of

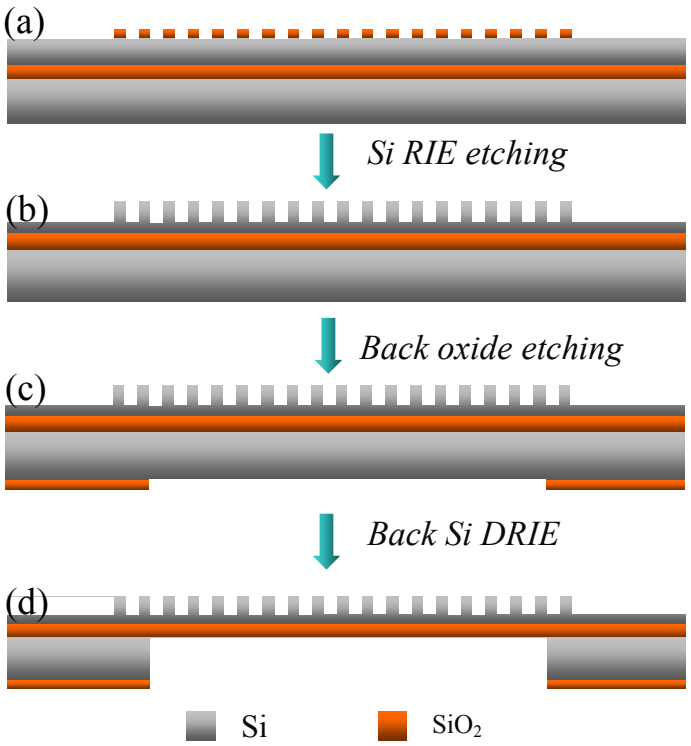

Figure 6.9: Photonic crystal based all-optical pressure sensor fabrication process schematic drawings. (a) A thin layer (~ 300 nm) of PECVD SiO_2 was deposited on SOI wafer (3 μm Si / 2 μm SiO_2). The PECVD SiO_2 layer was patterned by electron beam lithography, followed by oxide RIE etching. (b) Vertical Si nanowire arrays were formed by Si RIE etching, using SiO_2 as the etching mask. (c) A thick layer (~ 4 μm) PECVD SiO_2 was deposited on back side of the SOI wafer. Then it was patterned by optical lithography EV620 using backside alignment, followed by SiO_2 RIE etching. (d) The SOI wafer Si substrate was etched through by Si deep RIE, using the back PECVD SiO_2 layer as the etching mask and the SOI buried oxide as the stopping layer.

directly coupling of energy into selected device areas without any electrical interconnects. More importantly, we can use various lasers with different wavelength (from UV to near IR), or even modulated white light with continuous spectra, to actuate

our resonator, since the vertical silicon nano-pillar arrays with photonic crystal structures and wavelength comparable lattice constant, have been demonstrated to have highly enhanced broadband optical absorption efficiency (Fig. 6.10). Therefore, this realizes a high-efficiency broad-band optical actuation. Most interestingly, a nanopillar membrane acoustic speaker was demonstrated, by using a closely located microphone to detect the vibration response in the frequency range from 1 kHz to 20 kHz.

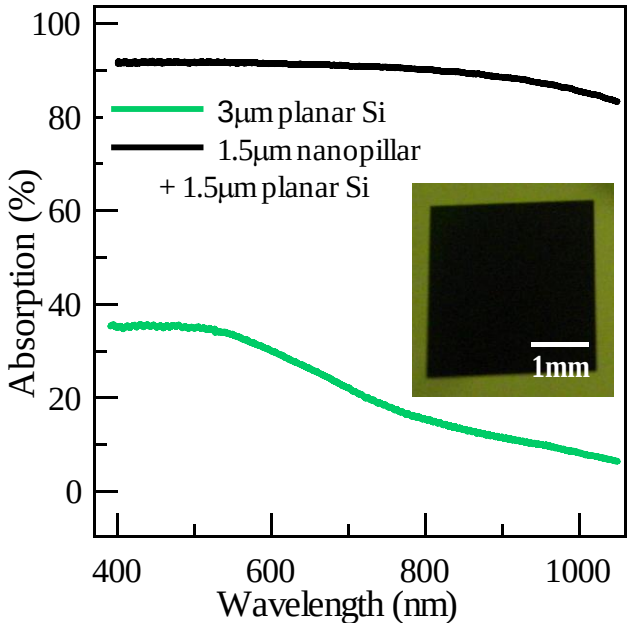

Figure 6.10: Measured light absorption spectra of the membrane with nanopillar arrays in figure 6.9, with that of planar Si for compare. Inset shows optical photograph of device top surface with nanopillar arrays (black).

Fabrication and experiments: Electron beam lithography was used to pattern the vertical silicon nano-pillar arrays, on a SOI wafer, followed by silicon RIE etching, using SiO_2 nano-posts as the etching mask. The vertical silicon nano-pillar array has conical pillars with 1.5 μm height, 250 nm base diameter, 100 nm top diameter, at a 600 nm pitch

(Fig. 6.8). As the photons enter the nano-pillar array they encounter an infinitum of reflective boundary conditions forming equivalent optical resonators at different wavelengths, resulting in light trapping. The measured optical absorption efficiency on these ordered nano-pillar arrays were more than 90% over broad-band wavelengths 400~1000 nm (Fig. 6.10), consistent with the "fully black" surface (Fig. 6.9 inset). Optical lithography with backside alignment was used to pattern the backside circular cavity (Fig. 6.8, 2.5 mm diameter), followed by silicon DRIE to etch through the silicon substrate using the SOI buried oxide as the stopping layer. A thin 50 nm layer of nitride was deposited to compensate the compressive stress in the SiO_2 layer.

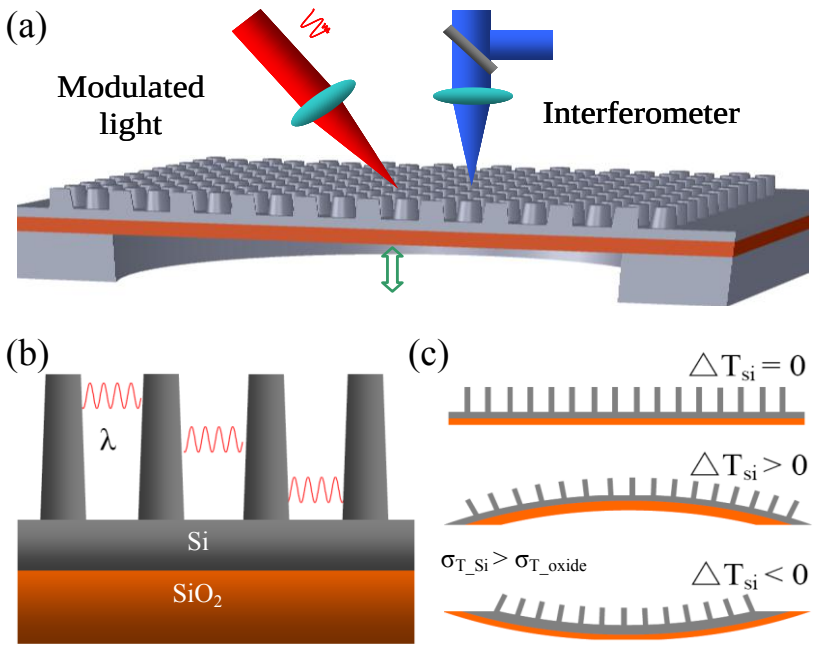

Figure 6.11: (a) Schematic for experiment set up in vacuum. The vibration response of the membrane resonator was measured using PolyTec interferometer. The laser diode was controlled by laser diode driver, with modulation input from a function generator. (b) Schematic of light trapping and absorption in the photonic crystal nano-pillar arrays. The light is absorbed and converted to heat. (c) Schematic for Si/SiO_2 bending moments, due to the local heating from the modulated laser.

For optical excitation, the irradiation of the modulated laser diode was focused onto the center of the membrane with nano-pillar arrays. The local heating from the incident modulated laser leads to Si/SiO_2 bending movements (Fig. 6.10 b&c). Since the top Si layer was thermally isolated by the SiO_2, convection losses are negligible. In order to

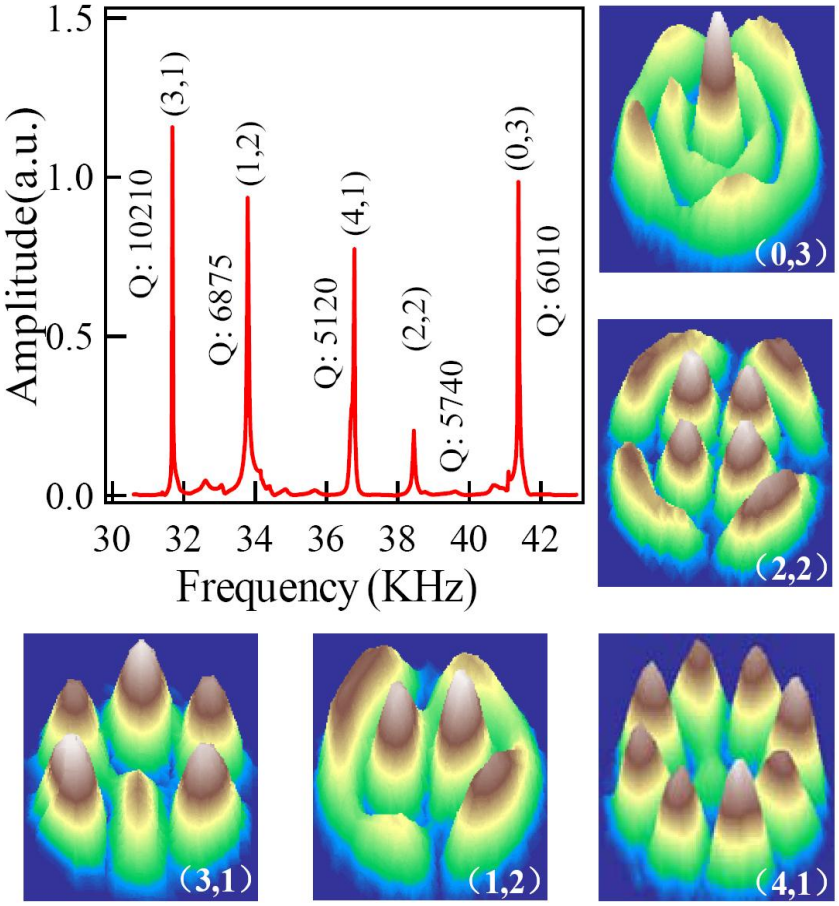

Figure 6.12: Measured resonances spectra response for optical actuation by the irradiation of the modulated laser diode, using interferometer (Fig. 6.12a). Our interferometer system has a limited minimum frequency response of 20 kHz. The modes are named by *(n, m)*, where n is circular node and m is diametrical node. The m and n values are determined by experimental mode amplitude mapping and simulation. Surrounding image plots show the measured amplitude mapping patterns of those corresponding modes. When mapping, the optical actuation was fixed at the resonance mode and the interferometer laser gun was controlled by a stage controller for lateral movement with sub-1 μm lateral resolution. These experiment data matched well with the theoretical vibration modes.

verify the optical excitation, we used piezoelectric actuation, by mounting a PZT plate to the backside of the device. The vibration deflection amplitude response of the membrane resonator was measured by PolyTec^{TM} interferometer with sub-1-nm amplitude resolution. Measured resonance spectra response of the membrane resonator from optical actuation matched very well with the spectra from PZT excitation. These data show linear optical actuation. The standing wave vibration amplitude 2D mapping patterns of the modes were measured (Fig. 6.12). During mapping, the optical actuation frequency was fixed at the resonance mode and the interferometer laser gun position was controlled by a 2-axis stage controller with sub-0.5 μm lateral resolution.

Most interestingly, a nano-pillar membrane speaker was demonstrated, by using a closely located microphone to detect the vibration response in the frequency range from 1 kHz to 20 kHz (Fig. 6.13). The acoustic emission could be measured using B&K 2205 Sound Pressure Level Meter, corresponding to sound pressure levels of 50-60 dB. When the actuation was fixed at a specific resonance frequency of the membrane 11.04 kHz, real-time microphone output could be recorded (Fig. 6.13b). When the optical actuation was switched between "on" and "off" back and forth, the output was tuned accordingly.

Model and Simulation: For our Si/SiO_2 bilayer membrane, we could simply model the system to be a flexural rigidity-dominated elastic unimorph plate with silicon and silicon-dioxide layers. With opto-thermal excitation, the local heating from the incident modulated laser leads to Si/SiO_2 bending moments (Fig. 6.11c). This opto-thermal excitation could be modeled as a transverse loading per unit area $f(r,\theta,t)$. By considering damping, the nonlinear partial differential equation governing the membrane can be obtained as equation [77]:

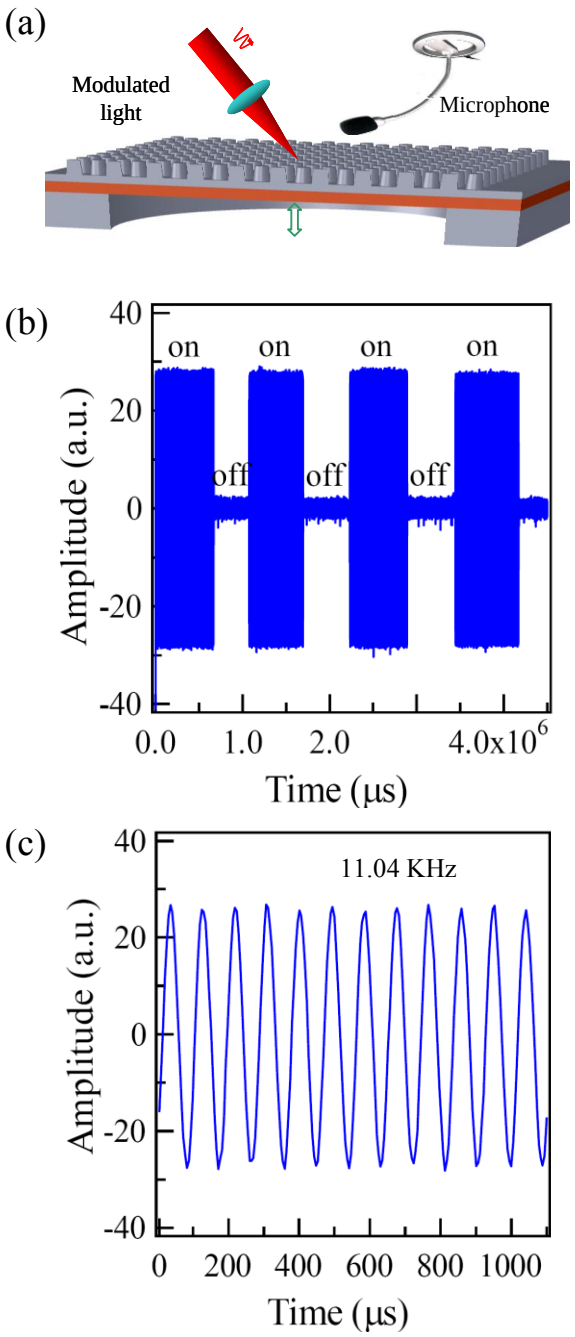

Figure 6.13: Nanopillar membrane opto-thermo-mechanical actuated acoustic speaker demonstration. (a) Schematic for experiment set up in air. A microphone, which was placed closely to the membrane, was used to record the vibration response of the membrane resonator in the frequency range from 1 kHz to 20 kHz. (b) Real-time microphone recorded output, in which the optical actuation was switched "on" and "off" back and forth. The actuation was fixed at a specific resonance frequency of the membrane, 11.04 kHz. (c) Zoom in plot of (b) at "on" state.

$$\rho h \frac{\partial^2 Z}{\partial t^2} + D\nabla^4 Z + \zeta \frac{\partial Z}{\partial t} = f(r,\theta,t) \tag{6.5}$$

where $Z(r,\theta,t)$ is the transverse displacement, ζ is the damping coefficient, h is the effective membrane thickness, ρ is the effective mass density, and D is the effective flexural rigidity of the membrane, and ∇^2 is the Laplacian. By solving this equation for a circular membrane with radius r_0, the resonant frequencies and their corresponding transverse displacement profiles at different mode shapes are obtained as follows [83]:

$$f_{mn} = \frac{1}{2\pi}\sqrt{\frac{\gamma_{mn}^4 D}{\rho h}} \tag{6.6}$$

$$Z_{mn}(r,\theta) = \left[J_m(\gamma_{mn} r) - \frac{J_m(\gamma_{mn} r_0)}{I_m(\gamma_{mn} r_0)} I_m(\gamma_{mn} r) \right] \cdot [A_{1m}\sin(m\theta) + A_{2m}\cos(m\theta)] \tag{6.7}$$

where the functions $J_m(\gamma_{mn} r)$ and $I_m(\gamma_{mn} r)$ are the Bessel function and the modified Bessel function of the first kind, γ_{mn} are the eigenvalues and the subscripts m and n represent the number of nodal diameters and nodal circles for the vibration mode, respectively. The final opto-thermo-mechanical actuation efficiency should be a combination of opto-thermo efficiency η_{op-th} and thermal-mechanical efficiency η_{th-me}:

$$\eta_{final} = \eta_{op-th} \cdot \eta_{th-me} \tag{6.8}$$

The thermal-mechanical efficiency depends on the strain and temperature distributions in the resonator. Here, we assume that we have the same thermal-mechanical efficiency. Therefore, the final actuation efficiency only depends on the opto-thermal efficiency. For laser heating actuation, light incident onto the resonator is absorbed and converted to heat via photon absorption. The opto-thermo efficiency is related to the light absorption efficiency $A(\lambda)$ of the device.

$$\eta_{op-th} \propto A(\lambda) \tag{6.9}$$

Therefore, we could calculate the efficiency enhancement factor F for our device, compared with the planar Si membrane devices.

$$F = \frac{\eta_{final\_NW}}{\eta_{final\_planarSi}} = \frac{\eta_{op-th\_NW}}{\eta_{op-th\_planarSi}} = \frac{A_{NW}(\lambda)}{A_{planarSi}(\lambda)} \tag{6.10}$$

where λ is the wavelength of the driving light.

For the resonant mode detected at 11 kHz, the sound pressure level was measured to be 55 dB, indicating a net acoustic power of 1.9 nW, using 30% acoustic power collection efficiency by the microphone. The amount of optical energy being dissipated is 10 mW of AC power. Thus the net efficiency of optical to acoustics is 0.2 ppm.

6.4 Femto-molar DNA photonic crystal nanowire array ultrasonic mass sensor

Nanoelectromechanical systems (NEMS) are enabling emerging applications in bio-sensing, due to their extraordinary sensitivities in mass changes [84]. For mass-change based nanomechanical bio-sensor, there are two important metrics [85]. The first one is its minimum detectable mass, which is defined as its absolute mass sensitivity. The resonance frequency of a NEMS resonator is a sensitive function of its mass, distributed over a mode shape. By measuring the resonance frequency change of the resonator, the mass change can be measured. Achieving small detectable mass changes requires the resonator to be as light as possible and operated at a resonance with high quality factor. The second metric is the minimum detectable mass per area (*Min-*M_A), defined as the minimum detectable mass divided by the surface sensing area of the device. *Min-*M_A is useful for comparing concentration sensitivity. When a bio-senor is immersed into a target solution at a certain concentration, the total mass of the bio-molecules bound to

sensor surface will be proportional to its surface sensing area, at fixed time in the linear region. For nanomechanical bio-sensing at ultra-low concentrations, it requires not only minimum detectable mass but also large device surface area for the binding molecules. Nanomechanical cantilevers have demonstrated single-molecule level absolute mass sensitivity [86]. However, single DNA detection in these methods require high concentration of DNA solution (10^{-9} mol/liter) to get even a single DNA binding, due to the small surface area of the sensitive device. A recent report [86] indicates that the challenge for new biosensors is to achieve low limits of concentration detection. Therefore, achieving high concentration sensitivity of a biosensor leads to a requirement of a *Min-*M_A, instead of a minimum detectable mass only.

Here, we present a novel nanomechanical resonator device with ordered vertical nanowire (NW) arrays on top of a Si/SiO_2 bilayer thin membrane. The device shows strongly enhanced total surface area-to-volume ratio 10^8 m^{-1}, enabling bio-molecule sensing in low-concentration target solution in the femto-molar concentration range.

Fabrication and experiments: The surface area-to-volume ratio of our ordered NW array resonator is extremely large (up to 10^8 m^{-1}). This is nearly two and three orders of magnitude larger than that of the micro-cantilever [87], and the suspended micro-channel resonators[85], respectively. This large surface area-to-volume ratio allows highly effective surface-based bio-molecular mass sensing, especially at ultra-low target concentrations (Fig. 6.14). For device fabrication, electron beam lithography was used to pattern SiO_2 nano-post arrays on a silicon-on-insulator (SOI) wafer. Si NW arrays were created by silicon reactive ion etching (RIE), using patterned SiO_2 nano-posts as the etching mask. Optical lithography was used to pattern the backside circular cavity, using

backside alignment. Silicon deep RIE was used to etch through the silicon substrate using the SOI buried oxide as the stopping layer. The

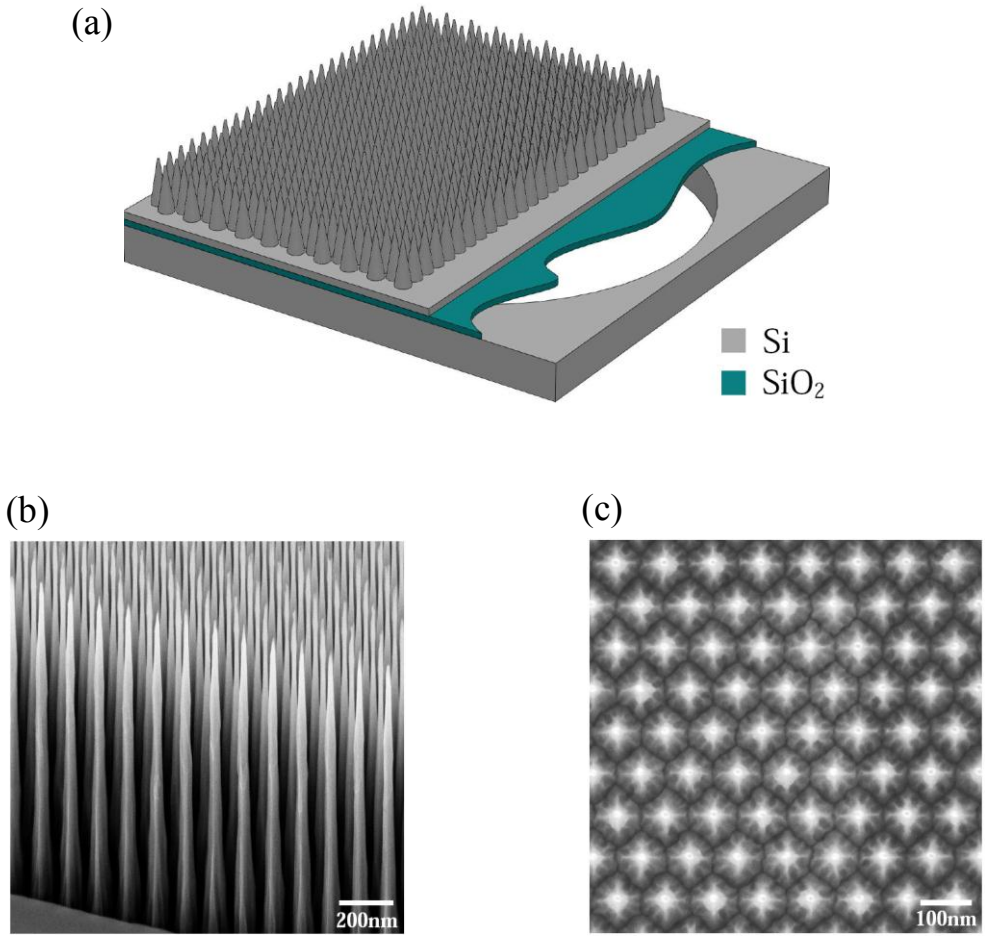

Figure 6.14: Device structure of the photonic crystal NW arrays mechanical resonator. (a) Schematic of device structure, with ordered vertical Si NW arrays on top of the Si/SiO_2 (300 nm/200 nm) membrane. The outer surface of NWs on membrane region was coated with a thin Ti/Au (2 nm/3 nm) passivation layer (not shown here). (b) SEM image (40^o side view) of the Si NW arrays, with 1.7 μm wire height, 100 nm wire base diameter, ~5 nm tip, at a 100 nm pitch. (c) SEM image (top view) of the NW arrays in (b).

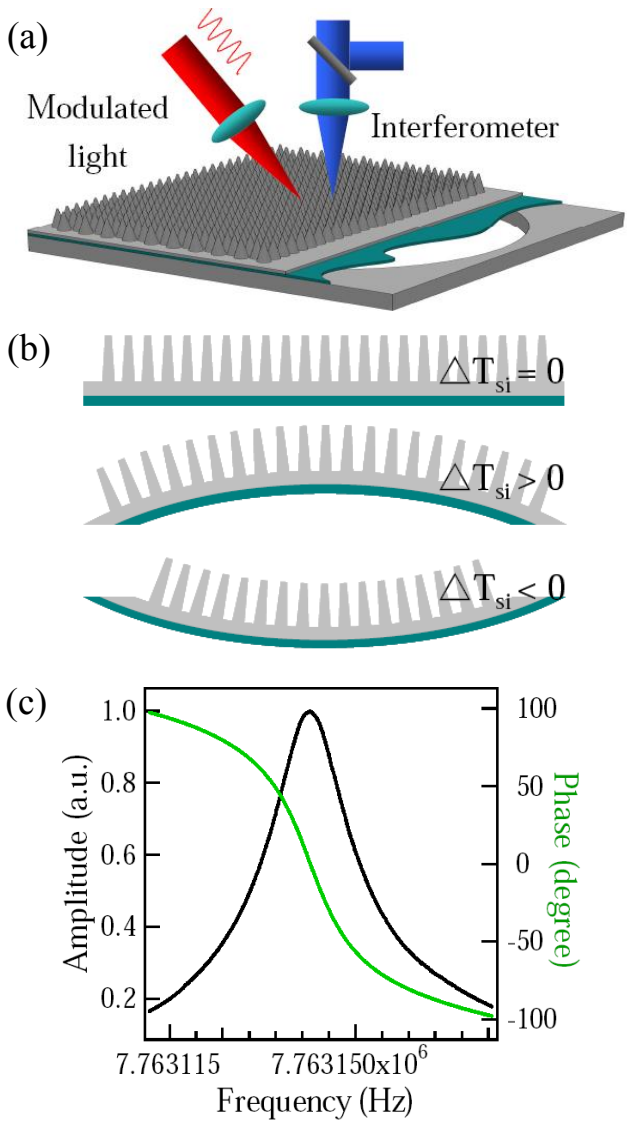

Figure 6.15: Opto-thermo-mechanical actuation for the photonic crystal NW array mechanical resonator, and its response. (a) Schematic for experiment set up. Intensity modulated light was used to actuate the membrane resonator and the vibration responses were measured using PolyTec interferometer with phase locked loop. (b) Schematic for Si/SiO_2 bending moments induced by the local heating from the modulated laser, due to the coefficient of linear thermal expansion varies for the bilayer materials. The periodic temperature difference (ΔT_{Si}) necessary for device excitation is of the order of 0.1 ℃ or less. (c) Measured amplitude and phase of the resonator's response showing a mode resonance at 7.76314 MHz. This mode has a high quality factor up to $Q \sim 3.2 \times 10^5$. The resonator was consist of vertical NW arrays on Si/SiO_2 bilayer membrane (Fig. 6.14), with membrane diameter of 50 μm.

photonic crystal NW arrays presented highly anti-reflective optical properties, due to the strongly enhanced light trapping and absorption efficiency, over a broad-band wavelength of 400~900 nm, as compared to the absorption in planar Si thin film. This is consistent with previous predictions and reports [82]. Light incident onto the NW arrays is absorbed and converted to heat efficiently via photon absorption. This was confirmed by the infrared (IR) camera image, showing that the NW area temperature increased much faster than that for the surrounding planar Si area, when they are irradiated by the same white light source. The strong broad-band light trapping and absorption optical properties of the photonic crystal NW arrays enable the high-efficiency opto-thermo-mechanical excitation for the resonator. An intensity modulated laser light (λ = 680 nm) was focused onto the membrane (Fig. 6.15a). The heating from the incident modulated light leads to bending moments in the Si/SiO_2 laminate (Fig. 6.15b), due to the differences in the coefficient of linear thermal expansion in the two layers. The opto-thermo-mechanical actuation directly couples optical energy into selected device areas, eliminating the electrical interconnects required in integrated electrostatic or piezoelectric actuation, and enabling high-efficiency remotely actuated bio-sensing. Compared with previous planar Si nano-mechanical resonators actuation methods by local laser heating [88], our excitation technique has the following advantages. First, the excitation efficiency of the photonic crystal NW array resonator has an enhancement factor of five to thirty over the measured spectra range 400~900 nm, compared with a planar Si thin film resonator, used as a control. Second, the wavelength of the driving light can be broad band, ranging from ultraviolet (UV) to near IR. In bio-sensing, this broad-band excitation capability enables the protection of the bio-molecules that are sensitive to high-energy

photons[89], by using low-energy photon excitation, such as the near IR range.

The thermo-optically excited vibration response of the laminate was measured using a PolyTec interferometer. (Fig. 6.15a) with a phase locked loop, which has a resolution of less than 0.1 nm in vibration amplitude resolution. One of the mechanical modes possesses highest quality factor up to 3.2 x 10^5, as shown by the frequency response plot in figure 6.14c. The high quality factor of the resonator (in vacuum 0.1 mTorr) might be due to the reduced surface loss [90] and clamping loss [91], through proper Si surface high temperature annealing treatment processes and the induced tensile stress to the Si film, respectively.

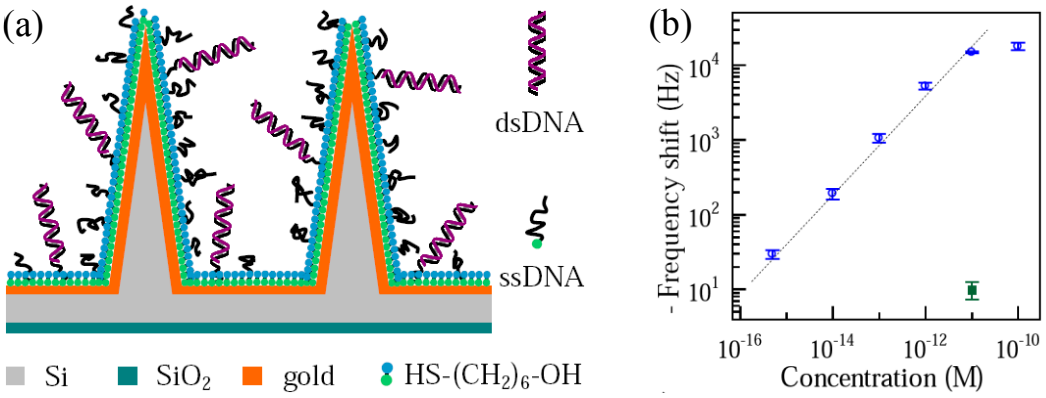

Figure 6.16: (a) Schematic of the DNA immobilization and hybridization. (b) Measured resonance frequency shift, plotted as a function of target concentration. The dashed fitting line is also added. The control experiment, using 10 pM non-matching DNA, is shown by a green square. The error bars present the variations for multiple measurements (n=3). The frequency shows saturation at concentrations above 10 pM.

The NW array resonator detection relies on the resonance frequency shift due to the mass change after bio-molecule attachment. With very low *Min-*M_A, the resonator enables high-sensitivity surface-based detection of bio-molecules at low concentrations. This is

proved by demonstrating a low-concentration DNA sensor. For DNA detection, single-stranded probe DNA molecules with known sequence are immobilized onto the gold-coated NW surface and followed by surface passivation with mercaptohexanol (MCH) [92]. The thin-gold coating does not affect the optical absorption.

For DNA hybridization, we carried out the control experiment against a non-matching DNA sequence at 10 pM concentration first and then the hybridization experiments for matching sequence at progressivey increased target DNA concentrations from 500 aM up to 10 pM. The resonance frequency negative shift has
a well-defined linear relation with the target DNA concentration (Fig. 6.16b). Since the total mass of the bio-molecules bound to the surface is proportional to its sensing area, then the concentration sensitivity of the sensor is $\delta C = \beta \cdot \delta m / S_{total}$, with constant β and total surface sensing area S_{total}.

Theory: The dynamics of a flexural mode nano-mechanical resonator can be modeled as a simple damped harmonic oscillator. The potential energy and the kinetic energy can be expressed as:

$$P.E. = \frac{1}{2} k \cdot z_{eff}^2 \qquad K.E. = \frac{1}{2} m_{eff} \dot{z}_{eff}^2, \tag{6.11}$$

Here z_{eff} is the equivalent displacement of the single degree-of-freedom resonator, k is the stiffness coefficient, and m_{eff} is the effective mass. Then the resonance frequency f_0 is:

$$f_0 = \frac{1}{2\pi} \sqrt{\frac{k}{m_{eff}}} \tag{6.12}$$

For an ideal planar circular membrane with radius r_0, thickness h, mass

density ρ , the displacement at a point (r,θ) on the membrane can be expressed as:

$$z(r,\theta) = \varphi(r,\theta) \cdot z_{eff} \tag{6.13}$$

Where $\varphi(r,\theta)$ is the mode shape and can be obtained from Bessel's function [93]:

$$\varphi(r,\theta) = \sum_{m=0}^{\infty}\sum_{n=1}^{\infty} A_{mn} J_m(\sqrt{\lambda_{mn} \cdot r})\cos(m\theta) + \sum_{m=1}^{\infty}\sum_{n=1}^{\infty} B_{mn} J_m(\sqrt{\lambda_{mn} \cdot r})\sin(m\theta) \tag{6.14}$$

The kinetic energy of the membrane vibration can be expressed as:

$$K.E. = \frac{1}{2}\{\rho \cdot h \cdot \int_0^{r_0} r dr \int_0^{2\pi} [\varphi(r,\theta)]^2 d\theta\} \cdot \dot{z}_{eff}^2 \tag{6.15}$$

By comparing equation 6.15 with equation 6.11, the effective mass of the membrane will be:

$$m_{eff} = m_{total} \cdot \frac{1}{\pi \cdot r_0^2} \cdot \{\int_0^{r_0} r dr \int_0^{2\pi} [\varphi(r,\theta)]^2 d\theta\} \tag{6.16}$$

When a mass change is added to the resonator, the resonance frequency will be:

$$f = \frac{1}{2\pi}\sqrt{\frac{k}{m_{eff} + \alpha \cdot \delta m}} \tag{6.17}$$

where α is a numerical constant that depends on the geometric localization of the added mass.

One of the fundamental limits imposed upon *Min-M_A* is from the thermo-mechanical noise, which originates from thermally driven random motion of the mechanical device [94]. By considering the thermo-mechanical noise, the mass sensitivity can be modeled as:

$$\delta m|_{\min} = 2m_{eff} \cdot \left(\frac{k_B T}{E_c}\right)^{1/2} \cdot \left(\frac{\Delta f}{Q \cdot f_0}\right)^{1/2} \tag{6.18}$$

where $E_c = m_{eff} \cdot (2\pi f_0)^2 \cdot \langle x_c^2 \rangle$ is the maximum drive energy, x_c is the vibration

amplitude, Δf is the minimum measurable frequency shift, Q is the quality factor

Table 6.1: Sensitivity comparison of our photonic crystal NW array resonator to other mechanical mass sensors.

Methods	**Absolute Mass Sensitivity (kg)**	**Total Surface Area (m^2)**	**Mass-per-Area Sensitivity (kg/m^2)**
Quartz Crystal Microbalance (QCM) [95]	1.0×10^{-12}	2.0×10^{-05}	5.0×10^{-08}
Suspended Microchannel Resonator [85]	1.0×10^{-18}	1.0×10^{-08}	1.0×10^{-10}
Resonant micro-cantilever [84]	5.0×10^{-23}	1.3×10^{-15}	3.8×10^{-08}
Resonant nano-cantilever [87]	8.7×10^{-23}	4.8×10^{-13}	1.8×10^{-10}
Photonic Crystal NW Array Resonator (ours)	2.5×10^{-20}	6.1×10^{-08}	4.1×10^{-13}

of the resonator. By using the measurement frequency uncertainty 1 Hz, the mass sensitivity of our resonator could be calculated to be 2.5×10^{-20} kg, which represents a lower-bound for the sensor mass sensitivity. Based on figure 6.17b, this is corresponding to a lower-bound concentration sensitivity of 3×10^{-18} mol/liter. Our measured concentration sensitivity is two orders of magnitude above this lower bound, which is due to other limits, including background noise of nonspecific binding, shot noise of the laser signal, etc.

6.5 Chaotic behavior of a membrane resonator with nanowire array

Nano-scale resonance systems can transition from a linear resonance operation to a nonlinear one through an increase in its dynamic operating amplitude. In the nonlinear regime of nano-electro-mechanical system (NEMS), phenomena, such as hysteresis [96], spring hardening [97], and pull-in [98], can occur. The nonlinear dynamical properties of the NEMS have been exploited for many applications. For instance, noise-enabled transitions in a nonlinear resonator were analyzed to improve the precision in measuring the linear resonance frequency [99], and a homodyne measurement scheme for a nonlinear resonator was proposed for increasing the mass sensitivity and reducing the response time [100].

The nonlinear dynamics of NEMS system might lead to the appearance of chaos. Chaotic behavior of a dynamical system is highly sensitive to initial conditions. Chaos can be observed in many natural systems, such as weather, where infinitesimally small perturbations can cause large effects. For chaotic systems, small differences in initial conditions will result in widely diverging outcomes, leading to system outcome prediction impossible [101]. Normally, such behavior may be investigated or explained through analysis of a chaotic mathematical model, or through analytical techniques such as recurrence plots and Poincaré maps. Nonlinearity, especially chaos, in NEMS systems has mostly been seen as a problem, but here we might want to ask whether one can explore chaos to enhance its applicability.

Here, we report the first chaotic behavior of a membrane mechanical resonator with nanowire (NW) array structured surface. Compared with the control sample without NW array, the membrane resonator with NW array structured surface (Fig. 6.17), can easily

transit from linear resonance operation to a nonlinear one, and further to a chaotic state, through an increase in its dynamic operating amplitude. The high nonlinearity of our device will help to spread the concentrated excitation energy from line-spectrum frequency to a broad-band frequency range (Fig. 6.18 & 6.19), which could be used for line-spectrum vibration isolation [102]. Vibration isolation is needed for MEMS device [103]; for example, inertial sensors, especially MEMS gyroscopes, can be interfered or even damaged by the undesired modes of vibration present in mechanically harsh environments. For a linear vibration isolation system, frequency conservation is the main characteristics. For nonlinear oscillations, external harmonic excitation from noise can exhibit a great variety of harmonic responses, sometimes countless when chaos appears. The concentrated energy therefore spreads from the frequency of excitation to a broad-band frequency range (Fig.6.18). For the given input energy, the response energy at the excitation frequency for the chaotic vibration system is much less than that for the linear vibration system [102]. Hence, a chaotic energy dissipater could be used to isolate sensors from external vibrations.

Device fabrication: For device fabrication, we used electron beam lithography to pattern the vertical silicon NW arrays, on a SOI wafer, by silicon reactive ion etching (RIE) using SiO_2 nano-posts as the etching mask. The vertical silicon NW array has 300 nm of wire diameter, 1 μm of pitch and 3.5 μm of height (Fig. 6.17b). These NW arrays show uniform wire diameter, controllable wire orientation and wire pitch spacing. Optical lithography with backside alignment was used to pattern the backside circular cavity (800 μm diameter), followed by a silicon DRIE to etch through the silicon substrate using the SOI buried oxide as the stopping layer. A PZT plate was adhesively bonded to the silicon

backside to actuate the membrane.

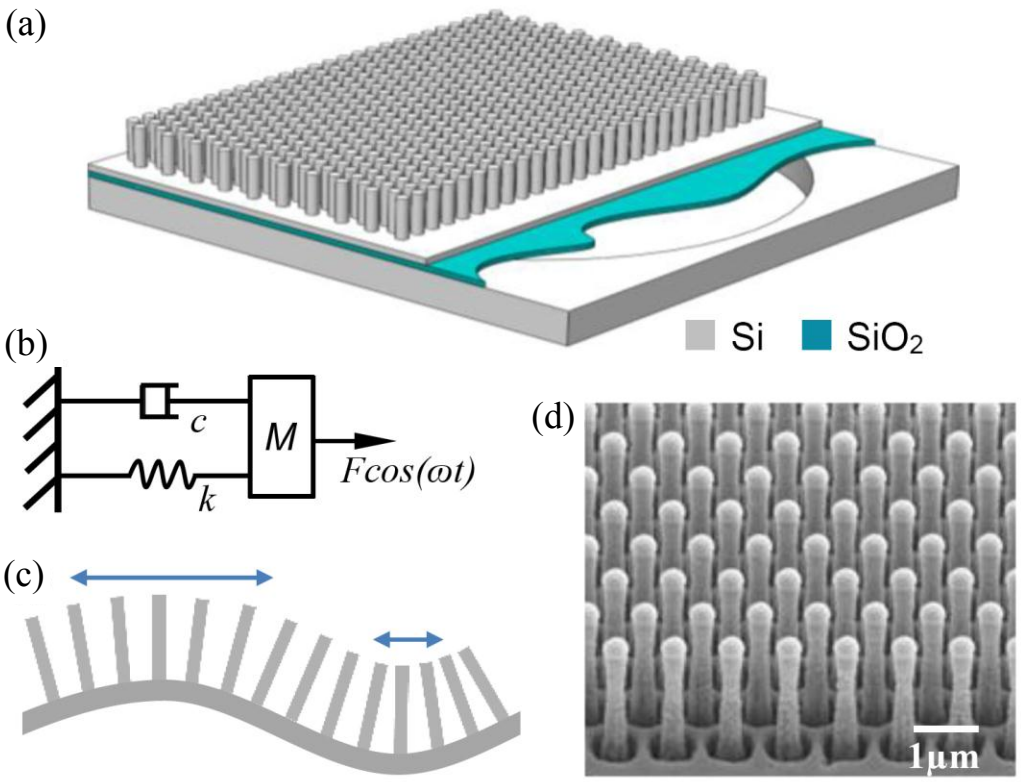

Figure 6.17: (a) Schematic for device structure. Vertical Si nanowire (NW) array were patterned on Si/SiO_2 (1 μm/2 μm in thickness) bilayer circular membrane (diameter 800 μm). (b) Schematic for the single degree of freedom model with damping. (c) Schematic for the space modulation of the NWs by the standing wave of the membrane. (d) SEM image of the NW array.

Experimental observations: The vibration response of the membrane was measured by an optical interferometer (PolyTec^{TM}). Power-spectrum density characteristics (Fig. 6.18) of the devices were measured by using a power spectrometer to analyze the output signal from the interferometer. The *vibration amplitude* versus *time* was measured using an

oscilloscope and a spectrum analyzer. For the membrane with NWs, we observed the fundamental resonance mode (f_1) at 163 kHz. When the system operates in linear range with low driving voltage 20 mV, the output signal shows monotonic spectrum (Fig. 6.19a top). The device can easily transition from linear resonance operation to nonlinear one, by increasing the PZT driving voltage. Initially, super harmonic nonlinear modes, such as $2f_1$ and $3f_1$, showed up at higher driving voltage (100 mV). Since the samples with and without NW are on the same chip and share the same PZT for actuation, the coupling from the PZT was the very similar in two samples. In the non-membrane area, the amplitudes of the NW versus non-NW samples were in the ratio of around 1:3, since the sample without NW has higher Q value (Table 6.2). When we increased the driving voltage further, the resonance modes and super harmonic modes will start to split into symmetric sub-bands, through bifurcation process. Finally, chaotic behavior of the device was observed (Fig. 6.18a bottom), at 300 mV driving voltage. In the chaotic state of the device, the concentrated excitation energy was spread from line-spectrum frequency to many peaks over broad frequency range. The measurement of upper frequency range was limited by the range of the spectrum analyzer. The nonlinearity originates from mechanical vibration and not optical detection nonlinearities as the maximum measured device vibration velocity was much less than the dynamic range of the interferometer used.

Moreover, we did the same measurement on the control sample, a Si membrane device without NW. The control sample was fabricated on the same chip, sharing the fabrication processes with the NW membrane device. These two samples have the same membrane size. For the control sample, a close resonance mode (f_2) at 153 kHz was

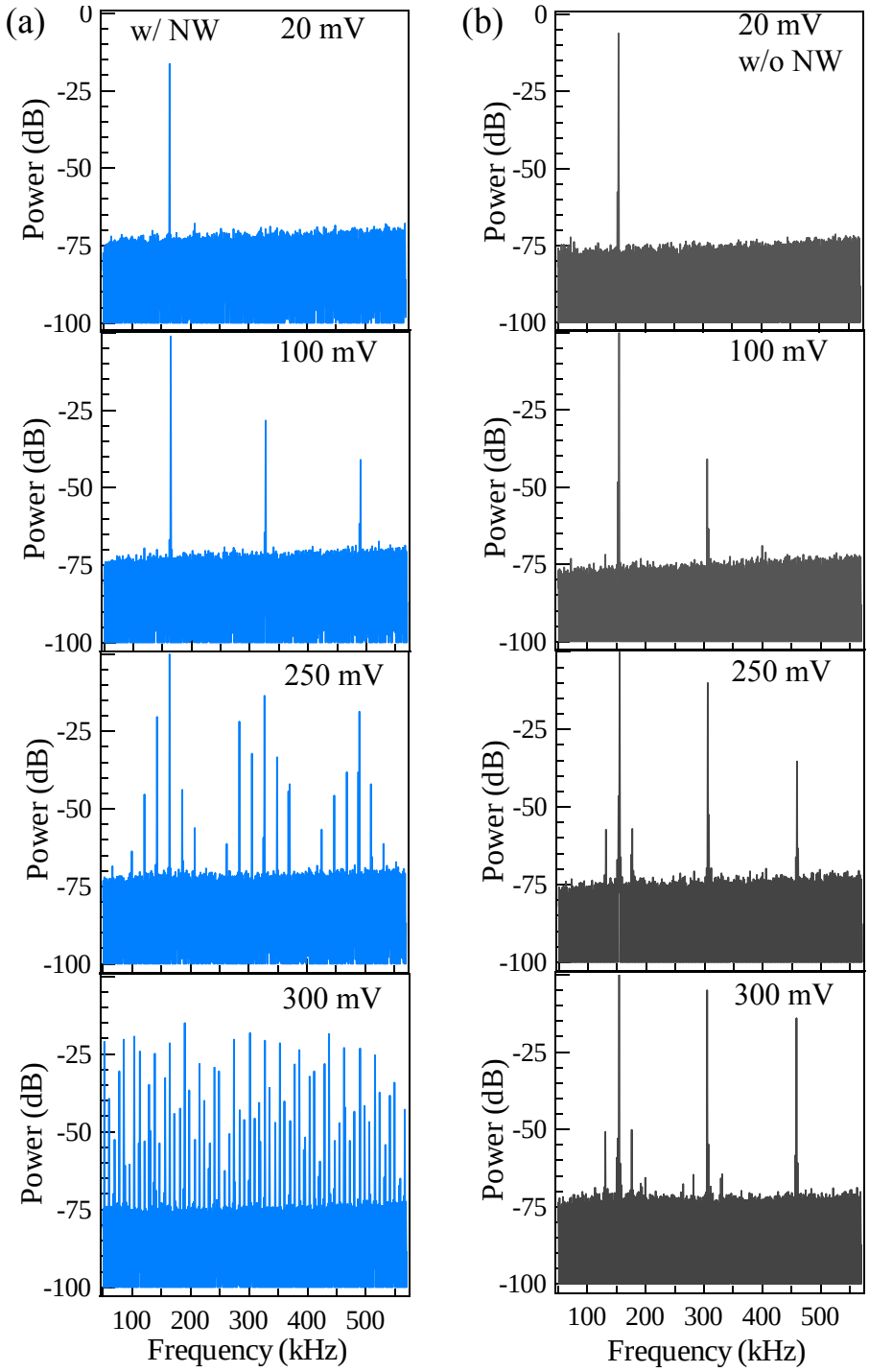

Figure 6.18: (a) Power-spectrum density characteristics of the membrane with NW at its resonant mode, when the device is driven by PZT under driving voltages of 20, 100, 250, 300 mV. (b) power-spectrum density of the control membrane without NW, when it is driven at the same driving voltages correspondingly.

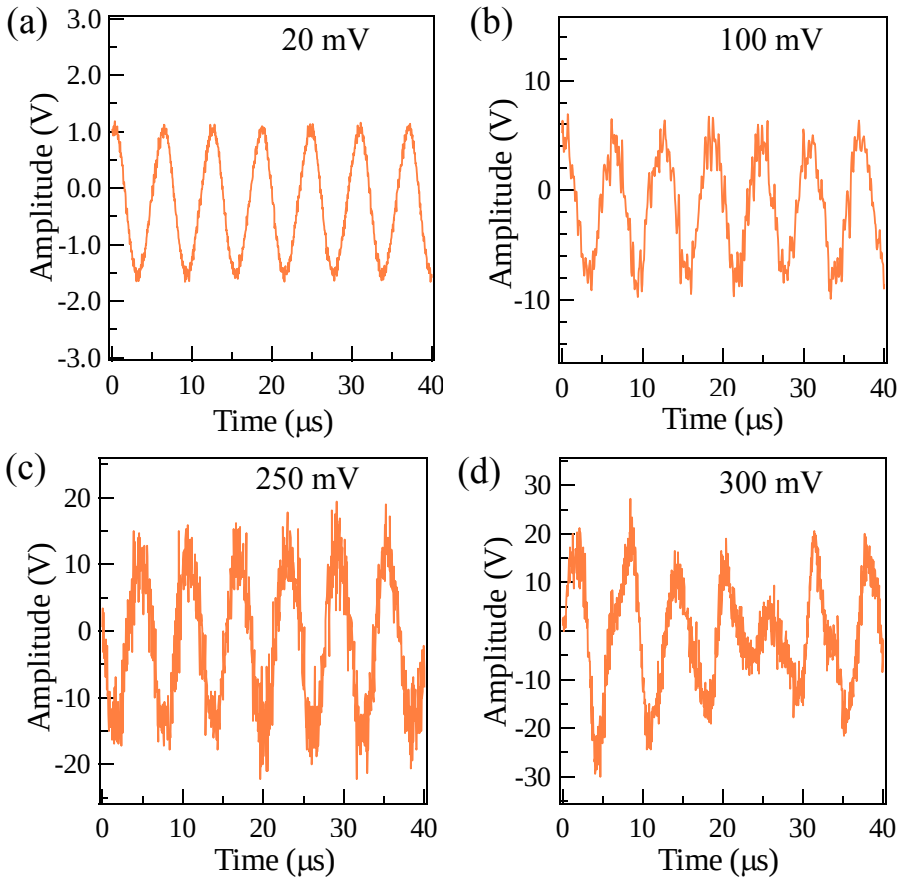

Figure 6.19: Output voltage vs. Time curves of the membrane with NW at its resonance mode, when the device is driven by PZT under driving voltages of 20, 100, 250, 300mV, for a-d, respectively.

observed, compared to the 163 kHz for the NW sample. The NW sample is lower frequency probably due to the lower effective density of the membrane. The power-spectrum density characteristics of this mode (Fig. 6.18b) ware also investigated as comparison. At higher driving voltage, super harmonic nonlinearity modes, such as $2f_2$ and $3f_2$, could be observed. However, compared with the membrane device with NWs, the control sample did not show obvious mode bifurcation process under the driving voltage. Even though much higher driving voltage was used and the device vibration velocity was reaching the upper dynamic limit of the interferometer, no chaos was

observed on the control sample.

Potential sources of nonlinearity: The high nonlinearity of our NW array membrane resonator comes from several reasons. Firstly, the NW array structured surface introduces large surface roughness to the membrane on one side, leading to the broken of symmetry when the membrane vibrates. Secondly, the membrane has significant nonlinearity in tension version compression. Thirdly, air-damping will also introduce significant nonlinearity to the system. These NWs can enhance the total surface area by a factor of 10, leading to larger the air-damping force. In following section, we would like to focus on the modeling of nonlinearity from air-damping.

Modeling and analysis: By considering damping, the nonlinear partial differential equation governing the membrane can be obtained as equation [104]:

$$\rho h \frac{\partial^2 Z}{\partial t^2} + D\nabla^4 Z + \zeta \frac{\partial Z}{\partial t} = f(r,\theta,t) \tag{6.19}$$

Where $Z(r,\theta,t)$ is the transverse displacement, ζ is the damping coefficient, h is the effective membrane thickness, ρ is the effective mass density, and D is the effective flexural rigidity of the membrane, and ∇^2 is the Laplacian.

By solving this equation for a circular membrane with radius r0, the resonant frequencies and their corresponding transverse displacement profiles at different mode shapes are obtained as follows [105]:

$$f_{mn} = \frac{1}{2\pi}\sqrt{\frac{\gamma_{mn}^4 D}{\rho h}} \tag{6.20}$$

$$Z_{mn}(r,\theta) = \left[J_m(\gamma_{mn} r) - \frac{J_m(\gamma_{mn} r_0)}{I_m(\gamma_{mn} r_0)} I_m(\gamma_{mn} r) \right] \cdot [A_{1m}\sin(m\theta) + A_{2m}\cos(m\theta)] \tag{6.21}$$

where the functions $J_m(\gamma_{mn}r)$ and $I_m(\gamma_{mn}r)$ are the Bessel function and the modified Bessel function of the first kind, γ_{mn} are the eigenvalues and the subscripts *m* and *n* represent the number of nodal diameters and nodal circles for the vibration mode, respectively.

Symmetric circular discs under high-amplitude excitation have been shown to undergo bifurcation, leading to chaotic motion [106]. This happens due to the presence of cubic nonlinearity in the system, which becomes prominent at large amplitude vibrations, where energy is spread into different modes of the disc. The mode mixing results in the excitation of other energy modes, from what is being directly forced. This results in the quasi-periodic response of the directly excited mode which may become chaotic. It has also been shown that if structural symmetry in such systems is broken, the chaotic transition becomes possible at a much lower forcing[106]. Additionally the route to chaos is through period doubling, which is what is observed in the current system. Hence the presence of NW brings down the forcing threshold for the chaos, which can now be observed at relatively lower amplitude forcing. In order to handle the complexity of the analysis we obtain a reduced ordered set of equations for the system at hand by projecting the governing partial differential equation of the system motion, on to the dominant linear modes and hence obtain a set of ordinary differential equations, which are integrated using a 4th order Runge-Kutta based ODE solver. The governing equations used for the simulations are [107]:

$$\ddot{x} + \alpha \dot{x} + \gamma(\dot{x})^2 + \omega_0^2 x + \beta x^3 = F\cos(\omega t) \tag{6.22}$$

where x is the position displacement, α is the linear damping coefficient, γ is the

quadratic damping coefficient, ω_0 is the resonance frequency of the system, β is the Duffing's cubic nonlinearity coefficient, F is the external excitation force and ω is the frequency of the external force.

Previous theoretical reports [107] showed that damping force plays an important role in the nonlinear dynamics of a Duffing's oscillation system, which is also confirmed by our simulation results. We simulated the Poincare maps (Fig. 6.20) for two different cubic nonlinear systems with: 1) linear damping, and 2) quadratic damping. Poincare map for the system is obtained by plotting the solution at every forcing time period, which shows the periodic vibrations at the forcing frequency, with one point, while period doubling is shown with twice the number of points. Figure 4b shows that quadratic damping has lower forcing threshold value for the chaos, among these three systems. For the system without damping, we did not get chaotic behavior in the force range simulated, which indicates that it has the highest forcing threshold value for the chaos. Therefore, the addition of damping or quadratic damping term of same order significantly reduces the forcing threshold value for chaos.

From our experiments, we observed that the membrane device with NWs did show higher damping, compared with the membrane without NWs. We measured three resonance modes on each device (Table 6.2). The modes for the device with NWs showed much lower quality factor values (40~75) than that of the modes from the device without NWs (250~350). The enhanced air damping might be due to the enhanced total surface area, by a factor of 10, from these high aspect ratio NW structures. The squeeze film damping between the nanowires is also expected to increase the damping.

Based on fluid dynamics theory [108], the drag force on an object is generally

dependent on its velocity, υ, and there exist two regimes where this dependence is either linear or quadratic. The parameter that differentiates these two regimes is the Reynolds number, R_e, which is the ratio of inertial to viscous forces,

$$R_e = \rho l \upsilon / \eta \tag{6.23}$$

where ρ is the fluid density, l is the characteristic cross-sectional length, υ is the velocity and η is the dynamic fluid viscosity. At high Reynolds number (R_e>10^3), drag is approximately dependent on the square of the velocity[108]:

$$f_d(\upsilon) = \frac{1}{2}\rho C_d A \upsilon^2 \tag{6.24}$$

where $f_d(\upsilon)$ is the velocity-dependent drag force where C_d is the drag coefficient, A is the cross-sectional area and. The drag coefficient, C_d, depends on the Reynolds number. At low Reynolds number (R_e<1), drag is linear with velocity [108]:

$$f_d(\upsilon) = 12\eta A \upsilon / l \tag{6.25}$$

Based on our measured velocity (Fig. 6.21a), the Reynolds number of our device

Table 6.2: Comparison of the measured quality factor (in air) for the modes of the membrane sample with NW and without NW.

Membrane with NW		Membrane without NW	
f (kHz)	Q	f (kHz)	Q
163	42	153	337
107	38	101	265
234	73	218	352

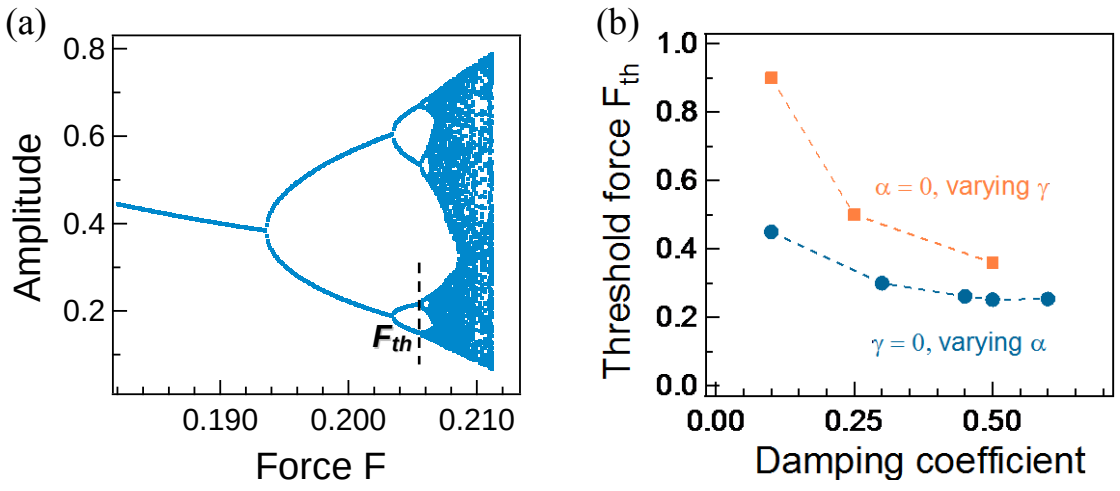

Figure 6.20: (a) Simulated Poincaré map of Position x vs. Force for a forced Duffing's oscillator with quadratic damping. Dashed line indicates the threshold force (F_{th}) value for chaos. (b) Simulated threshold force values as a function of the parameters for linear damping (alpha) and quadratic damping (gamma).

is in the range of 1-50 (Fig. 6.21b). Therefore, the damping force for our system should be a combination of linear and quadratic damping. Moreover, based on equation 6.24 and 6.25, both linear and quadratic damping forces could be enhanced by the NW structure, due to the enhanced surface area.

Moreover, it has been previously shown [109] that in beam vibration problems, combination resonance can occur when the sum of the natural frequency of certain modes of the system is close to the sum of other modes of the system. In this case energy can transfer from higher modes of the system to the lower ones but no other way. Excitation close to the higher modes can lead to vibration of lower modes. This also leads to periodic modulation of primary mode being excited. However for this combination of the frequencies to be in an internal resonance, it is necessary that the governing equation have a quadratic nonlinearity term. This term seems to originate from the quadratic

damping term that can be used to model the air drag. Here, the enhanced quadratic damping term from NWs might also trigger internal resonances, leading to lower threshold forcing value for chaos.

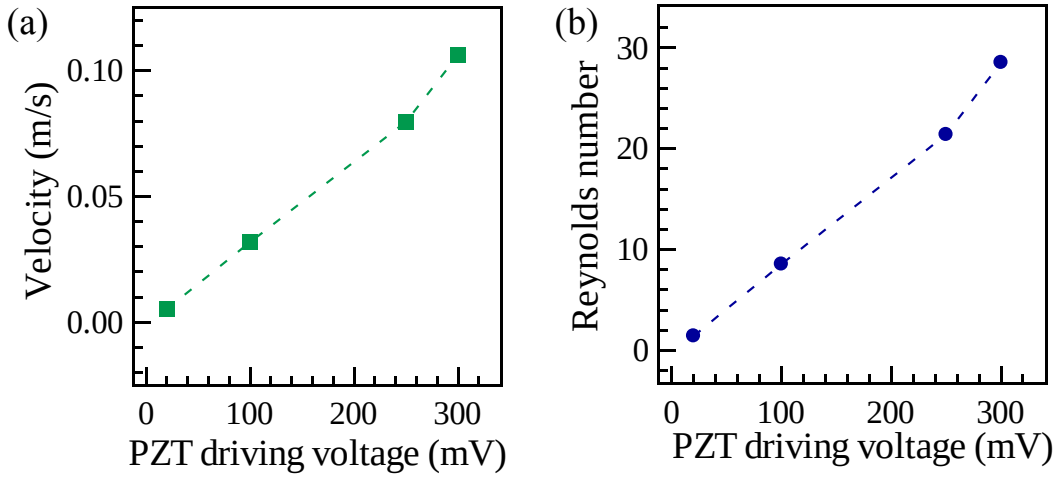

Figure 6.21: (a) Measured velocity as a function of the PZT driving voltage. (b) Calculated Reynolds number of our device based on the measured velocity and equation 6.23.

Of course, chaotic motion is a very complicated dynamic process, which is related to many factors. In order to have a better understanding on the chaotic behavior of our device, more theoretical and experimental work is needed. Although hard to model, our system will be useful where energy dispersion is required. Also, our device provides a good platform to investigate nonlinearity dynamics and potential chaos engineering.

CHAPTER 7

SELF-POWERED ION GAUGE AND SELF-POWERED ION PUMP

7.1 Background and motivation

High vacuum in small chambers has been an active field of research in MEMS packaging. Several solutions of hermetic packages have been developed [110-112] for inertial sensors and resonator oscillators. Recently a number of solutions have used thin-film sealing to achieve partial vacuum [113]. A few efforts, mainly stemming from U-Michigan have demonstrated sustained pressure of a few milli-Torr. Using UHV packaging techniques and use of getters, some solutions have demonstrated micro-Torr pressures, but the cost and size of these packages is too prohibitive. What is needed is a technique to realize high vacuum with no power penalty. If a pumping mechanism is found based on radioisotope films, then the pumping rate will be proportional to the film area. As the volume of cavity being pumped decreases, the surface/volume ratio increases and therefore, the film-based pumping mechanism becomes a better option at reduced scaling.

Moreover, in order to detect the pressure for high vacuum package, ionization gauges are widely used, which can be classified into hot and cold cathode gauges, depending on the generation methods of electrons. Conventional hot cathode ionization gauges, using thermally generated electrons, have serious out-gassing problems, while cold cathode ionization gauges, using a glow discharge to generate free electrons, suffer from the requirement of a few kilovolts to function and the instability of the glow discharge at low pressures. In the case of miniature vacuum systems (1-10 cc), power and volume

dedicated to an ion-gauge is highly limited, and is often the performance limiting component of portable vacuum instruments.

Radioactive isotopes ^{63}Ni thin film emitter has been used as fuel for low power batteries [114-116], nano-lithography sources [33, 34], because of its 100 years long half-life, suitable beta electron energy range (E_{av} = 14.9 keV, E_{max} = 67 keV) and safe radiation applications. The low-energy beta electrons from ^{63}Ni source can be shielded by thin layers (~25 μm) of most materials and could not penetrate the death skin of the human beings [117]. The beta emitter has high stability, since the beta emission is independent of pressure or temperature. This stable beta emitter with long life is an attractive candidate for cold cathode ionization gauges application.

Here, we used a radioisotope ^{63}Ni thin-film source as a cold cathode to realize a Self-Powered Ion Gauge (SPIG) (Fig. 7.1), demonstrating the largest sensitivity range among all reported pressure sensors, from high vacuum (10^{-6} Torr) to high pressure (10^{3} Torr). Since ^{63}Ni emits electrons with average energy 14.9 keV, this eliminates the high voltage and temperature for field emissions and thermal emission typically required in high vacuum gauges. ^{63}Ni has 100 years' half-life ensuring SPIG long time operation. The ^{63}Ni source is also highly stable as the radioisotope electron emission is independent of pressure or temperature [118]. We also show that SPIG can be transformed into a Self-Powered Ion Pump (SPIP) due to self-charge generated voltage induced ion-implantation of ionized gas atoms. The combination of SPIG and SPIP provides a near-zero-power solution to measuring and maintaining high vacuum in micro-system packages. The amount of radioactivity is in the micro-Ci to milli-Ci range, which is a commercially viable from both the point of view of safety and cost in a sealed package.

7.2 Self-powered ion gauge

In the case of miniature, potentially battery-powered vacuum systems (1-10 cc), power and volume dedicated to an ion-gauge is highly limited, and is often the performance limiting component of MEMS portable vacuum instruments. Attempts at realizing miniature ion gauges have utilized nanostructures to amplify emitted electron flux, such as carbon nanotubes (CNTs) ion gauges [119]. But the degradation of the field-emission current leading to short life time remains serious problems for CNT-based ion-gauges, possibly due to local heating and nano-tip reaction with oxygen. Hence, the problem of realizing a stable electron source operable over wide operating dynamic range of pressure and temperature is unsolved. Here, we use the stable radioisotope ^{63}Ni thin film source as the cold cathode to realize a SPIG (Fig. 7.1&7.2). A capacitor formed of a titanium plate and ^{63}Ni thin film were placed in a package that

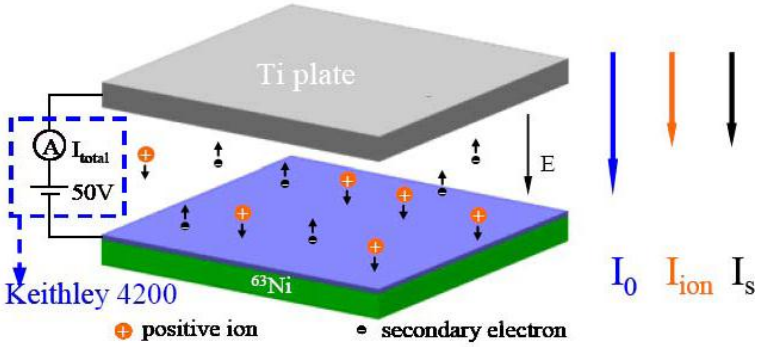

Figure 7.1: Schematic of Self-Powered Ion Gauge (SPIG). The gap between the ^{63}Ni and the Ti plate is 1 mm. The size of the ^{63}Ni thin film source is 1 cm X 2 cm.We define $I_{total} = I_0 + I_{ion} + I_s$.

was placed in a 10 cc vacuum chamber, being pumped by a turbo pump and pressure was controlled by a leak-valve. The current across the capacitor consists of the emitted current

and ion current due to electron ionization. Figure 7.3 shows the ability to measure pressure down to 10^{-6} Torr by calibrating the ionization current versus pressure. Pressure measured over several days shows no drift in the current measurement. A scaling theory on the sensitivity as a function of capacitor area shows sensitivity maintained even with capacitors as small as 5 mm^2, small enough for miniature MEMS packages.

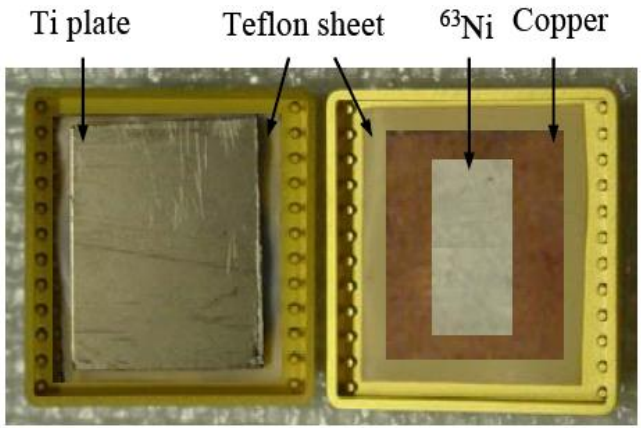

Figure 7.2: Photo of the device set up; the Teflon was chosen as out-gassing is minimal.

Based on Monte Carlo calculation, the high-energy beta electrons with average energy of 14.9 keV, emitted from the ^{63}Ni thin film source, can travel around 4cm in air under atmosphere pressure at room temperature. Some of these primary high energy electrons will penetrate deeply into the titanium metal plate, while the rest will be back scattered. These back-scattered electrons might still have high energy and they are possible to be scattered back and forth between the ^{63}Ni thin film and titanium plate capacitive structure, for hundreds of times, before they are absorbed. These back-scattered electrons and the primary beta electrons from ^{63}Ni thin film, will lead to many gas ionization events, producing substantial flux of positively charged ions, and related

amount of secondary electrons. The density of these positive ions and secondary electrons is proportional to the gas molecule number volume density, which is proportional to pressure.

The ^{63}Ni thin film was grounded and 50 V constant DC bias was applied on the stainless steel plate. The positive ions and the gas secondary electrons will be collected by the ^{63}Ni thin film and stainless steel plate, respectively (Fig. 7.1). Keithley 4200, which has a high current resolution down to 1 fA, was used for the DC voltage supply, and the total current measurement. The total current I_{total} includes both the basic current, defined as I_0 due to primary electrons and back-scattered electrons, and the ionization current, defined as $I_{ionization}$ due to the positive ions and the secondary electrons.

$$I_{ionization} = I_{total} - I_0 \tag{7.1}$$

The measured Total current I_{total} *vs Pressure* curve is shown in log plot in figure 7.3 a, with pressure ranging from 10^{-6} Torr up to 10^{3} Torr (~1.4 atm). The pressure was measured using commercially available Pfeiffer compact full range gauge with sensitivity down to 10^{-8} Torr as the standard. In high vacuum region with pressure ranging from 10^{-6} Torr to 10^{-4} Torr, we could see that I_{total} is linearly proportional to the pressure, in the double linear plots $I_{ionization}$ is much smaller than current I_0, since there is a small of amount of ionizations due to very small number density of gas molecules. The I_0 current could be considered to be a constant value shown in figure 7.3a inset, since the ionization is small and will give an insignificant effect on the back-scattered electrons. Therefore, an extrapolated I_0 value of 20.52 pA can be obtained by extrapolating the linear experimental data to the ideal real vacuum with zero Pa pressure (Fig. 7.3a inset). The ionization current $I_{ionization}$ can be obtained by reducing I_0 from the total current I_{total}, as

shown in equation 7.1. The double log plot of $I_{ionizaiton}$ *vs Pressure* curve (Fig. 7.3b) shows good linearity, from high vacuum down to 10^{-6} Torr to high pressure 10^{3} Torr.

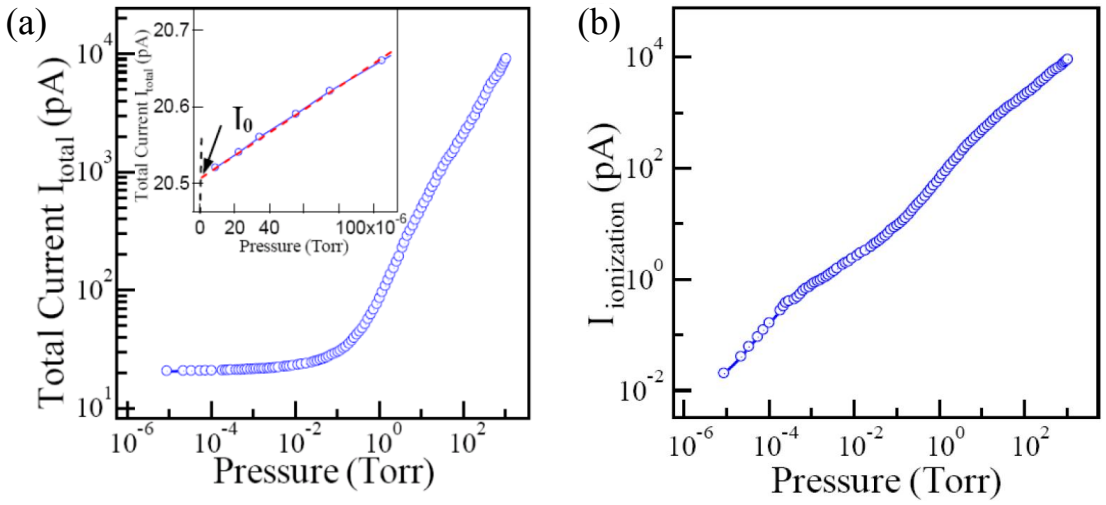

Figure 7.3: (a) Log plot of the measured Total current I_{total} *vs Pressure* curve of the device, with pressure ranging from $8.9\text{x}10^{-6}$ Torr up to $1.6\text{x}10^{3}$ Torr (~1.4 atm), at room temperature. Inset shows the linear plot curve of Total current vs Pressure for high vacuum region. The total current is almost linear to the pressure. We extrapolate the curve to the ideal absolute vacuum case (zero Pa pressure) and get a constant current value I_0. (b) Log plot of the measured ionization current $I_{ionization}$ *vs Pressure*. Here, we define ionization current by $I_{ionization} = I_{total} - I_0 = I_{ion} + I_s$.

7.3 Self-powered ion pump

To solve the vacuum problem, we develop ion-pumps that use the electron emission from ^{63}Ni directly. If no bias is applied across the SPIG capacitor at low initial vacuum (< 0.01 Torr), voltage as high as 7-10 kV can be generated across the capacitor [114]. This high voltage is able to accelerate the ions, created from gas ionization by emitted electrons, to high energy, and implant these ions into the top metal plate permanently. Energies as low as 1 kV are needed to implant a few nm into the top plate (Fig. 7.6). This pumping effect

makes the capacitor a Self-Powered Ion Pump (SPIP) (Fig. 7.4).

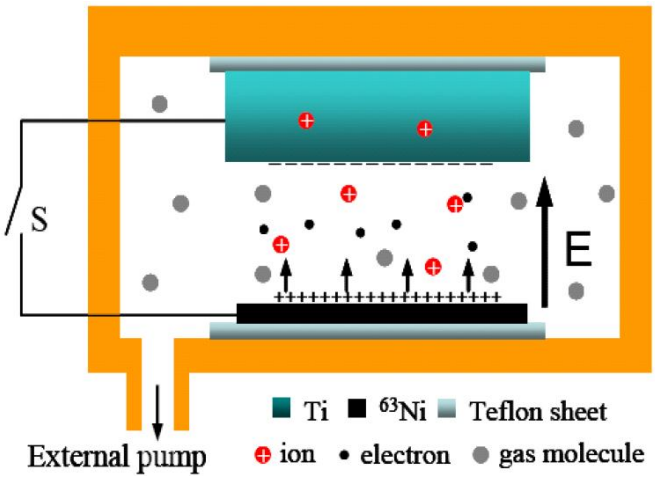

Figure 7.4: Schematic drawing for Self-Powered Ion Pump (SPIP) set up. When the switch *S* is open, there will be an electrical field E between the Ti and ^{63}Ni plates, due to the built up voltage (up to 10 kV) by the Ti self-charging from ^{63}Ni beta emission. The positive ions, from air gas ionization, will be accelerated and implanted into the Ti plate permanently. This will cause pumping effect. The SPIP is on when *S* is open, while it is off when *S* is closed.

SPIP is experimentally demonstrated in figure 7.4&7.5. When SPIP is off (*S* closed), the highest vacuum we could reach is 7.5×10^{-7} Torr, due to the balance of the external pumping with the vacuum system leaking. When SPIP is on (*S* open), the highest vacuum turns to be 5.0×10^{-7} Torr, due to the new balance of the vacuum system leaking with the external pumping and the pumping from SPIP. As shown in figure 7.5, if we turn on and off the SPIP back and forth, by controlling the switch open and closed, the minimum vacuum point will be switched up and down accordingly. This experimentally demonstrated the SPIP pumping. This preliminary result is promising but much work needs to be done to understand the details of the pumping process.

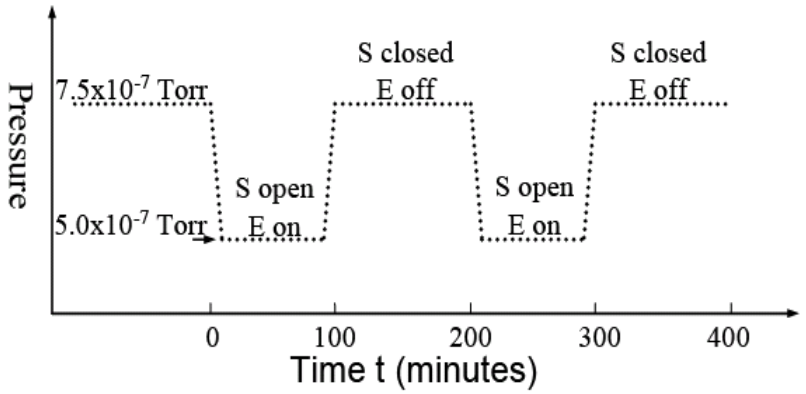

Figure 7.5: Experimental demonstration for SPIP. When SPIP is off (S closed), the highest vacuum we could reach is 7.5×10^{-7} Torr, due to the balance of the external pumping with the vacuum system leaking. When SPIP is on (S open), the highest vacuum turns to be 5.0×10^{-7} Torr, due to the new balance of the vacuum system leaking with the external pumping and the pumping from SPIP. As shown in figure 3b, if we turn on and off the SPIP back and forth, by controlling the switch open and closed, the minimum vacuum point will be switched up and down according. This experimentally demonstrated the SPIP pumping.

7.4 Model analysis

The emitted electrons can undergo many energy transfer interactions with the gas atoms. As the electrons travel across a gap, they undergo ionization reactions with the gas atoms resulting in ion creation. As the initial electron energy is quite high (average E_{av} = 14.9 keV), the cross-section of ionization is very small. The electrons eventually hit the opposing electrode and the impact can result in secondary electron emission. The secondary electron energy is on the order of a few to hundreds of eV. We believe it is the secondary electrons that lead to a larger amount of ionization of the gas molecules, as the cross-section is higher. The original emitted electrons build up charge on the collector and also result in positive charge on the emitting plate. This leads to a voltage and

electric field buildup in the gap that accelerates away the secondary electrons toward the emitter. The number of electrons emitted for high-energy electrons is very low, causing the back current due to secondary electrons being less than the emitted current. Our current measurements in vacuum indicate that 20 secondary electrons are emitted from the cathode for every 100 emitted from the anode to the cathode. In addition to the secondary electrons, the ionization due to the emitted and secondary electrons lead to an ionic current that also reduces the current due to the emitted electrons. At zero applied voltage across the capacitor, the ions recombine resulting in a current that only contains the secondary electron current information. As the gap is decreased, the amount of ions and ionic currents decrease.

The ions are generated with kinetic energies of approximately 10-300 eV, which can collide with other gas atoms or can impact the cathode sputtering the atoms off the cathode. Atoms that have energy higher than the ionization potential of 100-200 V govern the sputtering process. The ions that collide with the cathode can undergo two actions. First, most of ions will be accelerated by the high build up voltage and be implanted into the top metal plate permanently. Second, the ions can also sputter the Ti metal plate the sputtered Ti atoms can also remove atoms from the gas due their specific reactivity. The rate at which ions are generated can be approximated by:

$$n_{ion} = \frac{\sigma}{A} N n_{gas} \tag{7.2}$$

where n_{ion} is the rate of ion generated per cm^3 per second, σ is the cross-section of the incident electron and gas particle impact, A is the total area of the emission, N is the rate of electrons emitted per second from the radioactive thin film, and n_{gas} is the density of gas. The cross-section σ is a strong function of the energy of the electron and is low at

high energies beyond a few hundred eV. The secondary electrons produced during the electron impact also contribute to the gas ionization with a similar rate given by equation 7.2.

$$n_{ion-se}(E) = \frac{\sigma_{se}(E)}{A} N_{se} n_{gas} = \frac{\sigma_{se}}{A} n_{seg}(E) N n_{gas} \tag{7.3}$$

where $\sigma_{se}(E)$ is the cross-section of ionization for electrons with energy E, N_{se} is the total number of secondary electrons generated per second, $n_{seg}(E)$ is the number of secondary electrons generated with incident electrons of energy E, and N is the rate of incident electron generation. We need to integrate over the ^{63}Ni energies and particle densities to get the total ion generation. The generated ions can also undergo secondary reactions with the gas creating further electrons and ions. Since the secondary ion generation rate is proportional to the initial ion generation, the total

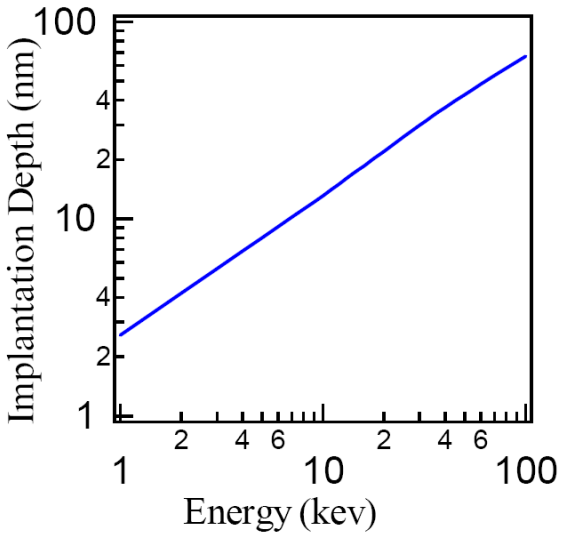

Figure 7.6: Ion implantation depth vs ion energy curve. The ion is oxygen and the target is Ti metal.

generation rate for the ions is proportional to the gas concentration and the incident

electron rate. The rate of sputtering of atoms from the Ti plate and the corresponding rate of pumping will also be proportional to this product. The total rate of gas atom removal assuming removal of all ions (assuming no recombination) will therefore be

$$\frac{dn_{gas}(E)}{dt} = -(n_{ion} + Gn_{ion}) = -(1+G)(\sigma + \sigma_{se} n_{seg}(E))\frac{N}{A} n_{gas} \tag{7.4}$$

where G is the number of secondary ion generated.

Once the solution for the gas density is obtained, the expression for the gas pressure can be written as:

$$p = n_{gas} kT \tag{7.5}$$

where P is the pressure; k is Boltzmann constant and T is temperature.

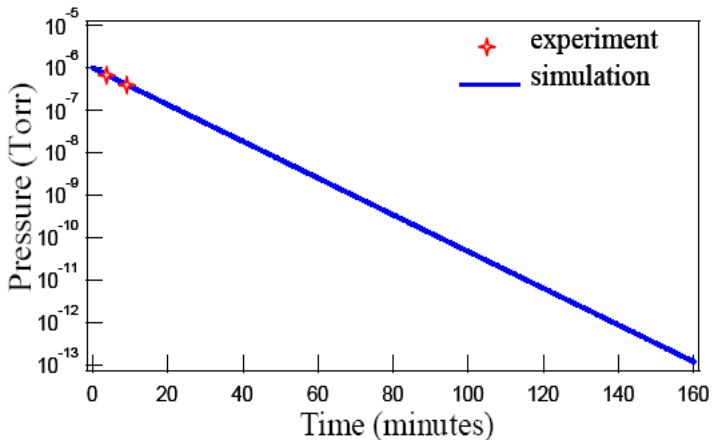

Figure 7.7: Pumping speed Simulation for SPIP. We assume to use 1 cm^3 small volume chamber, which is pre-pumped to initial pressure P_0 = 1x10^{-6} Torr.

7.5 Summary

We have realized a Self-Powered Ion Gauge (SPIG), using radioisotope ^{63}Ni thin-film source as the cold cathode, which has the largest sensitivity range among all reported

pressure sensors, from high vacuum (10^{-6} Torr) to high pressure (10^{3} Torr). SPIG can also be transformed into a Self-Powered Ion Pump (SPIP) due to self-charge generated voltage induced ion-implantation of ionized gas atoms. The pumping model for our SPIP is analyzed, which matches well with our current available experimental data. Here, the combination of SPIG and SPIP provides a near-zero-power solution to measuring and maintaining high vacuum in micro-system packages.

CHAPTER 8

RIPEL APPLICATIONS TO INERTIAL SENSOR FABRICATIONS

8.1 Introduction and motivation

Optical lithography can be a limiter for MEMS inertial sensor performance and cost reduction. Inertial sensor biases, which determine the sensor performance, are determined by mismatches in spring constants and proof-masks, which are caused by variations in lithographic feature definition, and other device fabrication steps such as etching, and variations in material properties. Conventional optical lithography, with critical dimension (CD) of ~1 micron over 10-100 micron lateral feature sizes, produces 10-20% dimensional tolerances when attempting to define MEMS features [120]. Traditional e-beam lithography that can define the geometries down to 20 nm features with much higher precision would reduce the biases and improve precision and noise of inertial sensors. This is particularly true in the case of MEMS made in SOI silicon, where the material properties of top epi-silicon are uniform. This is contrast to poly-silicon structures where Young's modulus and stress gradients also affect mismatches.

Although e-beam lithography can be used to define devices with high precision, the throughput for nano-scale lithography would be too low for cost competitive devices. Moreover, e-beam lithography systems are expensive to procure and maintain due to the large electron focusing column and high vacuum environment needed [28]. Recently developed SCALPEL [32] at Lucent Technologies and PREVAIL [9] at IBM brought projection electron beam lithography within range of use in IC production. Fundamentally, both of them are still not wafer-scale massively parallel like optical

lithography, and their throughputs are still too low for commercialization.

8.2 Analysis of how variations offset sensor performance

Figure 6.1 shows a schematic of a MEMS device that has capacitors on both sides of the movable plate. Assume that equal voltage is applied over both plates. Note that the equilibrium point is always at $x = 0$. The expression for the pull-in voltage is:

$$U_p = \sqrt{\frac{kg^3}{2\varepsilon A_{el}}} = \sqrt{\frac{2EWh^3g^3}{\varepsilon A_{el}L^3}} \tag{8.1}$$

$$k = \frac{4EWh^3}{L^3} \tag{8.2}$$

where k is the stiffness of the four clamped beam in series (Fig. 8.3a). L is the beam length (300 μm), W is the beam depth (5 μm), h is the width of the beam (0.6 μm), E is the Young's modulus of silicon and g is the gap of the capacitor (1 μm).

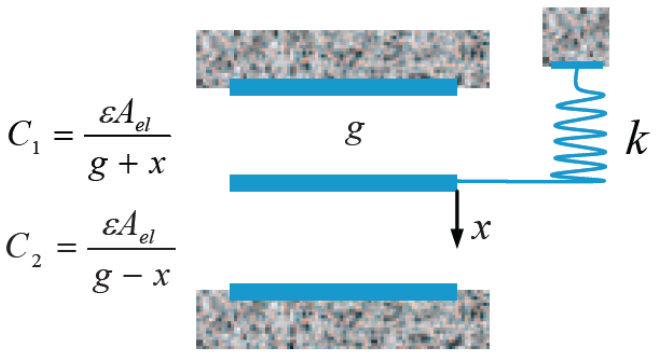

Figure 8.1: Schematic of a MEMS device that has capacitors on both sides.

The pull-in voltage error is expressed as:

$$\left(\frac{\Delta U_p}{U_p}\right)^2 = \frac{3}{2}\cdot\left[\left(\frac{\Delta g}{g}\right)^2 + \left(\frac{\Delta h}{h}\right)^2 + \left(\frac{\Delta L}{L}\right)^2\right] \tag{8.3}$$

Based on equation 8.3, the device performance variation will increase the dimension of the device scales down. Therefore, it requires higher fabrication accuracy for the manufacturing tools. For example, for a NEMS device with beam dimension smaller than 1 μm, even a fabrication variation of 100 nm will cause around 15% device performance error.

8.3 Lateral electrostatic accelerometer using RIPEL

Here, we used RIPEL to fabricate a representative MEMS accelerometer. RIPEL, which utilizes the spontaneously emitted energetic electrons from beta emitting radioisotope thin-films to parallel expose resist through a stencil mask, enables arbitrarily large area substrates to be defined with wide dynamic range of dimensions (nm to mm), with nm precision. The critical dimension of RIPEL was demonstrated to be sub-75nm, by both simulation and experiments [33, 34]. The ability to realize nano-scale dimensions in parallel over large area substrates (limited by the size of the radioisotope source and stencil mask) enables the potential reduction of very inexpensive high performance devices. To prove validity of using RIPEL for MEMS, we fabricated an electrostatic sensed accelerometer, largely based on the commercial ADXL differential capacitive sensor. Change of C_1 and C_2 (Fig. 6.2a) in response to acceleration are differentially detected. We made a stencil mask, as shown in figure 8.3b. The RIE tungsten dry etching process produced highly vertical mask edges, with very small edge surface roughness (<

20nm) (Fig. 8.3b left), which is critical for RIPEL to get devices with small edge surface roughness as well as high degree of dimensional matching between devices. The fabricated devices fabricated by RIPEL indeed show high degree of dimensional matching (1-5%) across five devices. Moreover, for electrostatic actuated MEMS devices with gaps within the micron or sub-micron range, the electrode roughness greatly

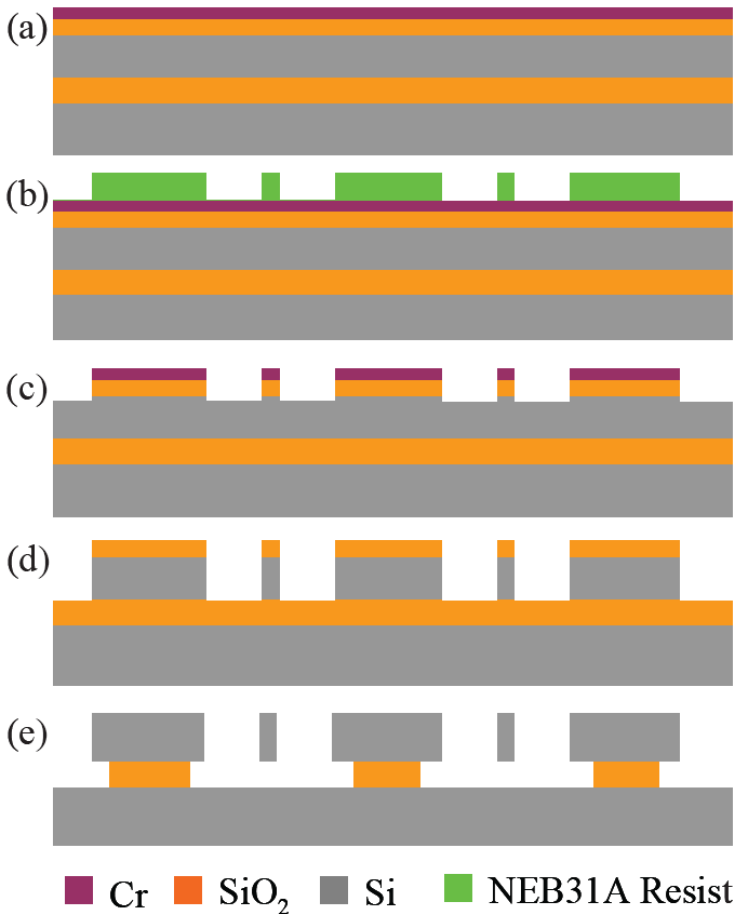

Figure 8.2: Device fabrication process, using RIPEL. (a) 300 nm SiO_2 was deposited on SOI (5 μm Si + 2 μm SiO_2), followed by 50 nm Cr evaporation. (b) Negative tone electron resist NEB31A (120 nm) patterning, by RIPEL parallel exposure, using fabricated mask. (c) Cr RIE etching, using NEB31A as etching mask. (d) Si vertical etching, using Cr as etching mask. (e) BOE (6:1) SiO_2 etching to release the beam, followed by critical point dry.

influences the pull in voltage, since the surface roughness determines the surface van der Waals forces and Casimir forces that modify the basic electrostatic forces [121]. Here, our measured accelerometer beam edge roughness is small (± 10 nm) (Fig. 8.4 left bottom insert), which leads to the consistency between the measured pull in voltage and

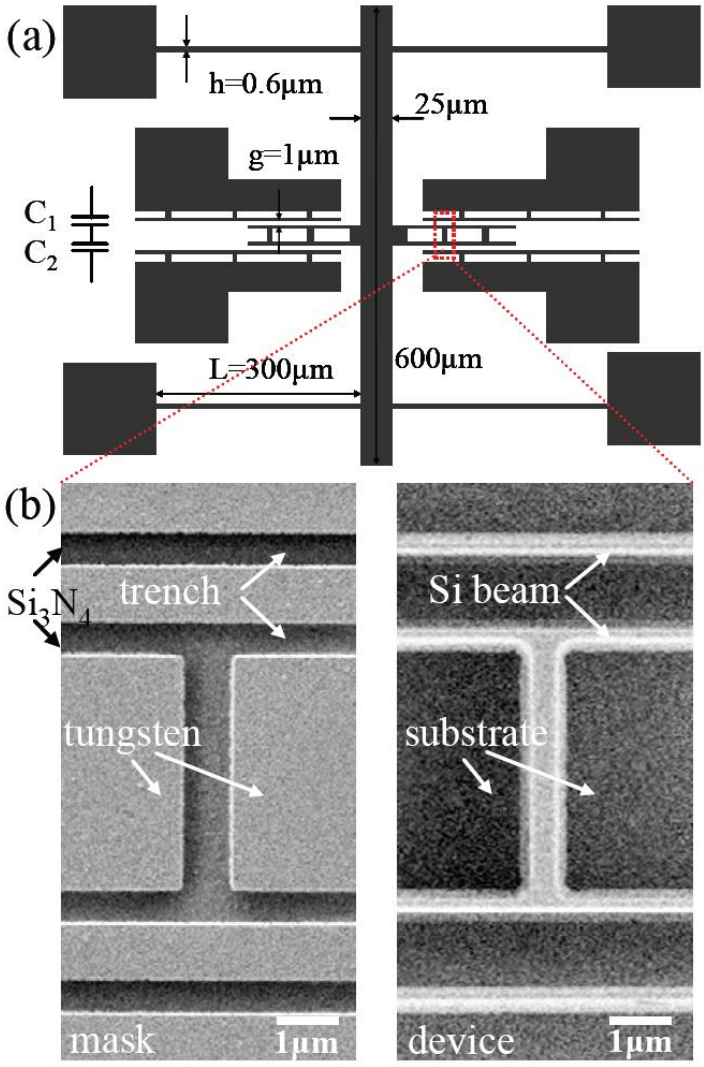

Figure 8.3: (a) Layout of our lateral electrostatic accelerometer; (b) SEM images of the RIPEL mask and the corresponding final accelerometer device, for the dashed line region in (a).

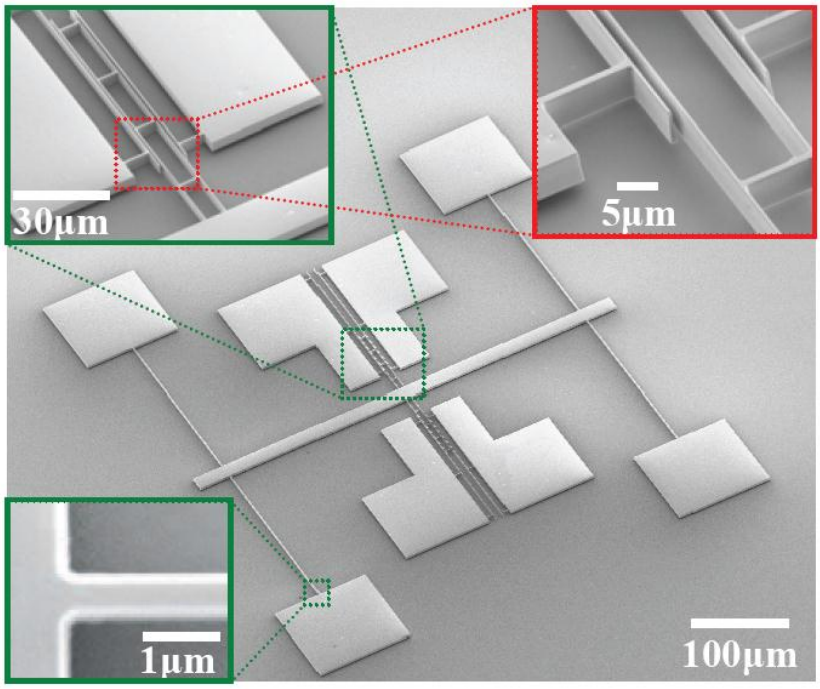

Figure 8.4: SEM images (45 degree view) of the electrostatic accelerometer device, fabricated by RIPEL. Left bottom insert shows the top view of the beam with highest aspect ratio.

the theoretical calculation value. Also, due to small average deviation on the beam width ($\pm$ 15 nm), the measured pull in voltage uniformity from device to device is also small (1-5%). Our lateral electrostatic accelerometer device fabrication shows that we could use RIPEL to fabricate MEMS devices in nano-scale, with high precision, over large areas for reduced cost.

APPENDIX A

FABRICATION PROCESS FOR NANOWIRES AND NANO-CONES

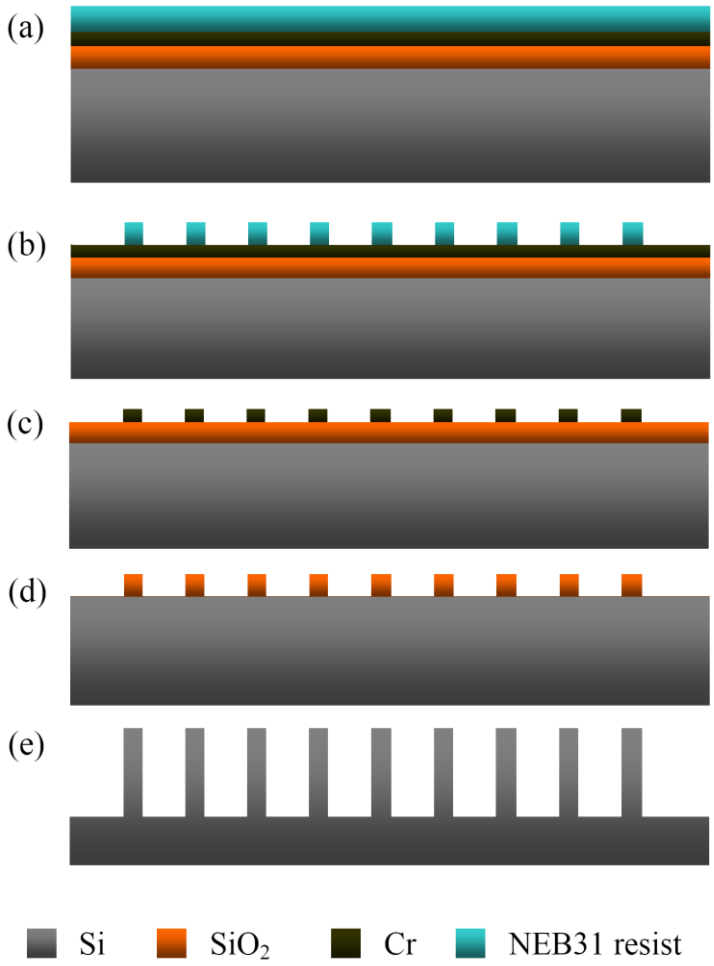

Figure A.1: Silicon vertical nanowire arrays fabrication process. (a) 400 nm of SiO_2 was produced by wet oxidation at 1100 degree on n-type (100) silicon wafer, followed by 50nm Cr evaporation. A thin layer (~100nm) of negative tone e-beam resist NEB31A was spun on top. (b) NEB31A e-beam resist was patterned by electron beam lithography exposure, followed by normal NEB31A development. (c) Cr was dry etched, using NEB31A as the etching mask. (d) SiO_2 was dry etched by RIE, using Cr as the etching mask. (e) Vertical Silicon NW Arrays were produced by Si RIE etching, using SiO_2 as the etching mask.

We could modify the RIE etching condition to adjust the slant angle of the nano-conical-frustum (NCF). For our NCF arrays (Fig. 5.2, slant angle 3.8 degree), we used Si RIE etching condition: 70 sccm of BCl_3, 2 sccm of H_2, 20 mTorr pressure, with 65 W power. For our quasi-nanowire (QNW) arrays (slant angle zero degree), we used Si RIE etching condition: 70 sccm of BCl_3, 2 sccm of H_2, 10mTorr pressure, with 70 W power.

APPENDIX B

RIPEL MONTE CARLO SIMULATION MATLAB CODE

```
function   [fN_hole_out, fN, fBESite] = Au_Hole _Penetration_Parallel

%Initial Input Parameters
%E0=input('Please input the energy of the electron in (keV):');
%Z=input('Please input the Atomic Number Z of the solid:');
%Angle_X0=input('Please input Initial beam incident angle Theta_x:');
%Angle_Y0=input('Please input Initial beam incident angle Theta_y:');
%Angle_Z0=input('Please input Initial beam incident angle Theta_Z:');
%T_Au = input('Please input the thickness of Au on source(nm):');
N_electrons = input('Please input the Total number of electrons you need to simulate:');
d_beam = input('Please input the beam diameter in (nm):');
Z_Au = input('Please input the thickness of top Au layer in (nm):');
S_hole = input ('Please input the hole size for the Au layer(nm):');

%Site(1).energy = E0;
%Site(1).XYZ(1:3)=[0,0,0];
%Site is a variable like: Site(N).XYZ(1:3), Site(N).angle(1:3), Site(N).energy(1)
%Read Data from files
%Ratio_all=wk1read(num2str(Z+200));

Rand_R1                    = rand(1, 10000000);
Rand_R2                    = rand(1, 10000000);
Rand_angle                 = rand(1, 10000000);
Rand_If_Edistri            = rand(1, 10000000);
Rand_Init_SAI              = rand(1, 10000000);
Rand_Leng                  = rand(1, 10000000);
Rand_R_rand                = rand(1, 10000000);
Rand_Sai                   = rand(1, 10000000);
Rand_R_Delta_rand          = rand(1, 10000000);
Rand_R_Sai                 = rand(1, 10000000);
Rand_R_ATOM_elastic        = rand(1, 10000000);

R1_n                   = 1;
R2_n                   = 1;
Rand_angle_n           = 1;
R_elastic_or_inelastic_n = 1;
R_rand_n               = 1;
Rand_If_Edistri_n      = 1;
Init_SAI_n             = 1;
Leng_n                 = 1;
R_elastic_or_inelastic_n = 1;
R_rand_n               = 1;
Sai_n                  = 1;
R_Delta_rand_n         = 1;
R_Sai_n                = 1;
```

```
Rand_ATOM_elastic_n                = 1;

n_ZEP520 = 1;

Ratio_all                = wk1read(num2str(279));
Ratio_all_inelastic = wk1read(num2str(479));
Ratio_all_inelastic_ZEP520 = wk1read('IMFP_DEDS_NoExchange_113');

Ratio_ZEP520_all=wk1read(num2str(299));    % for EMFP values
Ratio_C_all=wk1read(num2str(6+200));        % for cross section for elastic collision
Ratio_H_all=wk1read(num2str(1+200));
Ratio_O_all=wk1read(num2str(8+200));
Ratio_Cl_all=wk1read(num2str(17+200));

Fraction(1:13)=6;
Fraction(14:28)=1;
Fraction(29:30)=8;
Fraction(31)=17;

N_BE = 1;   % tracking back scattering electrons
BESite(N_BE).energy = 0;
BESite(N_BE).angle(1:3)   = [0,0,0];
BESite(N_BE).XYZ(1:3)   = [0,0,0];

E_distr = wk1read('Edistribution');

N_hole_out = 1;
Hole_out(1).XYZ = [0,0,0,0];

% for N electrons loop

for k = 1:N_electrons
    % Generate initial beam position
    R1 = Rand_R1(R1_n);
    R1_n = R1_n +1;
    R2 = Rand_R2(R2_n);
    R2_n = R2_n +1;
    X0 = d_beam*(R1-0.5);
     Y0 = 1/10*d_beam*(R2-0.5);

    %Generate initial beam position
    Site(1).XYZ = [X0,Y0,0];

    % Generate angle distribution
    Init_THETA = Rand_angle(Rand_angle_n)*pi*5/12;
    Rand_angle_n = Rand_angle_n + 1;

    Init_SAI    =2*pi*Rand_Init_SAI(Init_SAI_n);
    Init_SAI_n = Init_SAI_n + 1;

    Angle_X0 = acos(sin(Init_THETA)*cos(Init_SAI));
```

```
    Angle_Y0 = acos(sin(Init_THETA)*sin(Init_SAI));
     Angle_Z0 = Init_THETA;

    % Generate angle distribution
     Site(1).angle(1:3)=[Angle_X0,Angle_Y0,Angle_Z0];

    % Site(1).angle(1:3)=[pi/2,pi/2,0];
    R_if_Edistri = Rand_If_Edistri(Rand_If_Edistri_n);
    Rand_If_Edistri_n = Rand_If_Edistri_n + 1;
    E0_find_index = find(E_distr(1:180,3) > R_if_Edistri);
    E0 = E_distr(E0_find_index(1), 1) + (R_if_Edistri - E_distr(E0_find_index(1), 3))*(
E_distr(E0_find_index(1)+1, 1)- E_distr(E0_find_index(1), 1)) /( E_distr(E0_find_index(1)+1,
3)- E_distr(E0_find_index(1), 3));


     % Generate initial electron energy from the source, considering Energy distribution of 63-Ni
thin film
    Site(1).energy = E0;

if ( - S_hole/2 < X0 & X0 < S_hole/2 )

        X_new = X0 + Z_Au / cos(Angle_Z0)*cos(Angle_X0);
        Y_new = Y0 + Z_Au / cos(Angle_Z0)*cos(Angle_Y0);
        if ( - S_hole/2 < X_new & X_new < S_hole/2 )
            N_hole_out = N_hole_out + 1;
            Hole_out (N_hole_out).XYZ = [X_new,Y_new,Z_Au,Site(1).energy];

            N_ZEP520(n_ZEP520).XYZ      = [X_new,Y_new,0];
            N_ZEP520(n_ZEP520).energy = Site(1).energy;
            N_ZEP520(n_ZEP520).angle   = Site(1).angle;

            n_ZEP520 = n_ZEP520 +1;

            continue
        else
            if ( X_new >= S_hole/2   )
              X_face = S_hole/2;
              Y_face = Y0 + (Y_new - Y0) * (X_face - X0) / (X_new - X0);
              Z_face = 0 +   (Z_Au - 0) * (X_face - X0) / (X_new - X0);

            elseif ( X_new <= -S_hole/2 )
              X_face = - S_hole/2;
              Y_face = Y0 + (Y_new - Y0) * (X_face - X0) / (X_new - X0);
              Z_face = 0 +   (Z_Au - 0) * (X_face - X0) / (X_new - X0);
          end
        end

        Site(1).XYZ = [X_face,Y_face,Z_face];
else

   n=1;
```

```
while(Site(n).energy >= 0.02)
    break_sign = 0;
    if (Site(n).energy >= 9)
        Mean_free_path_inelastic = 4.725817 + (7.808919 - 4.725817)/(9-5)*(Site(n).energy - 5);
    else
        MFP_inelastic_index = find(Ratio_all_inelastic(2:28,1)>Site(n).energy)+1;
        Mean_free_path_inelastic = Ratio_all_inelastic(MFP_inelastic_index(1)-1,185) +
(Site(n).energy - Ratio_all_inelastic(MFP_inelastic_index(1)-
1,1))*(Ratio_all_inelastic(MFP_inelastic_index(1),185)-
Ratio_all_inelastic(MFP_inelastic_index(1)-
1,185))/(Ratio_all_inelastic(MFP_inelastic_index(1),1) -
Ratio_all_inelastic(MFP_inelastic_index(1)-1,1));
    end

        MFP_elastic_index = find(Ratio_all(2:35,1)>Site(n).energy)+1;
        Mean_free_path_elastic = Ratio_all(MFP_elastic_index(1)-1,100) + (Site(n).energy -
Ratio_all(MFP_elastic_index(1)-1,1))*(Ratio_all(MFP_elastic_index(1),100)-
Ratio_all(MFP_elastic_index(1)-1,100))/(Ratio_all(MFP_elastic_index(1),1) -
Ratio_all(MFP_elastic_index(1)-1,1));

        Mean_free_path = 1/(1/Mean_free_path_inelastic + 1/Mean_free_path_elastic);
        Leng = -log(rand) * Mean_free_path;

        R_elastic_or_inelastic = rand;

        R_elastic_or_inelastic_n = R_elastic_or_inelastic_n + 1;
        if (R_elastic_or_inelastic < (1/Mean_free_path_elastic) / (1/Mean_free_path) )

            R_rand = Rand_R_rand(R_rand_n);
            R_rand_n = R_rand_n + 1;
            if (Site(n).energy < 30)
                Theta_Emin_index = find(Ratio_all(MFP_elastic_index(1)-1,3:98) > R_rand)+2;
                Theta_polar_Emin = Ratio_all(1,Theta_Emin_index(1)-1) + (R_rand -
Ratio_all(MFP_elastic_index(1)-1,Theta_Emin_index(1)-1)) *
(Ratio_all(1,Theta_Emin_index(1)) - Ratio_all(1,Theta_Emin_index(1)-1)) /
(Ratio_all(MFP_elastic_index(1)-1,Theta_Emin_index(1)) - Ratio_all(MFP_elastic_index(1)-
1,Theta_Emin_index(1)-1));

                Theta_Emax_index = find(Ratio_all(MFP_elastic_index(1),3:98) > R_rand)+2;
                Theta_polar_Emax = Ratio_all(1,Theta_Emax_index(1)-1) + (R_rand -
Ratio_all(MFP_elastic_index(1),Theta_Emax_index(1)-1)) * (Ratio_all(1,Theta_Emax_index(1))
- Ratio_all(1,Theta_Emax_index(1)-1)) /
(Ratio_all(MFP_elastic_index(1),Theta_Emax_index(1)) -
Ratio_all(MFP_elastic_index(1),Theta_Emax_index(1)-1));

                Theta_polar = Theta_polar_Emin + (Site(n).energy -
Ratio_all(MFP_elastic_index(1)-1,1))*(Theta_polar_Emax - Theta_polar_Emin) /
(Ratio_all(MFP_elastic_index(1),1) - Ratio_all(MFP_elastic_index(1)-1,1));

                clear Theta_Emin_index;   % important to clear these vectors after each loop
```

```
            clear Theta_Emax_index;
        else
            Theta_index = find(Ratio_all(27,3:98) > R_rand)+2;
            Theta_polar_30 = Ratio_all(1,Theta_index(1)-1) + (R_rand -
Ratio_all(27,Theta_index(1)-1)) * (Ratio_all(1,Theta_index(1)) - Ratio_all(1,Theta_index(1)-1)) /
(Ratio_all(27,Theta_index(1)) - Ratio_all(27,Theta_index(1)-1));
            Theta_polar = (300 - Site(n).energy)/(300 - 30)*Theta_polar_30 ;
        end

        %Following code is used to compute Next Site_Next   XYZ value
        if   (sum(cos(Site(n).angle(:)).^2)==1)
             Arfa = Site(n).angle(1);
             Beta = Site(n).angle(2);
             Garma =Site(n).angle(3);
        else
             COSANGLE=cos(Site(n).angle);
             Angle=acos(COSANGLE./(sum(COSANGLE(:).^2)).^0.5);
             Arfa = Angle(1);
             Beta = Angle(2);
             Garma =Angle(3);
        end

        % setting polar angle here
             Thet = Theta_polar;
        % using a rand number for Thai angle
             Sai   = 2*pi*Rand_Sai(Sai_n);
             Sai_n = Sai_n +1;

            M = [sin(Thet)*cos(Sai), sin(Thet)*sin(Sai), cos(Thet)]*[sin(Arfa), -
cos(Arfa)*cos(Beta)/(cos(Beta)^2+cos(Garma)^2)^0.5,   -
cos(Arfa)*cos(Garma)/(cos(Beta)^2+cos(Garma)^2)^0.5 ; 0, cos(Garma)*sin(Arfa)+
cos(Arfa)^2*cos(Garma)/(cos(Beta)^2+cos(Garma)^2)^0.5, -cos(Beta)*sin(Arfa)-
cos(Arfa)^2*cos(Beta)/(cos(Beta)^2+cos(Garma)^2)^0.5; cos(Arfa), cos(Beta), cos(Garma)];

        %Set new angle calculation values to next Site:
             Site(n+1).angle=acos(M);

        %input site XYZ values:
             M_n = cos(Site(n).angle);
             Site(n+1).XYZ = Site(n).XYZ + M_n*Leng;

        %input site energy values
             Site(n+1).energy = Site(n).energy;     % elastic colision;

        % for inelastic case:
       else

        % determine delta_E using a rand number
             R_Delta_rand = Rand_R_Delta_rand(R_Delta_rand_n);
             R_Delta_rand_n = R_Delta_rand_n + 1;
```

```
        if (Site(n).energy < 9)   % for Mott cross section
            Delta_Emin_index = find(Ratio_all_inelastic(MFP_inelastic_index(1)-1,3:182) >
R_Delta_rand)+2;
            Delta_E_Emin = Ratio_all_inelastic(1,Delta_Emin_index(1)-1) + (R_Delta_rand -
Ratio_all_inelastic(MFP_inelastic_index(1)-1,Delta_Emin_index(1)-1)) *
(Ratio_all_inelastic(1,Delta_Emin_index(1)) - Ratio_all_inelastic(1,Delta_Emin_index(1)-1)) /
(Ratio_all_inelastic(MFP_inelastic_index(1)-1,Delta_Emin_index(1)) -
Ratio_all_inelastic(MFP_inelastic_index(1)-1,Delta_Emin_index(1)-1));

            Delta_Emax_index = find(Ratio_all_inelastic(MFP_inelastic_index(1),3:182) >
R_Delta_rand)+2;
            Delta_E_Emax = Ratio_all_inelastic(1,Delta_Emax_index(1)-1) + (R_Delta_rand -
Ratio_all_inelastic(MFP_inelastic_index(1),Delta_Emax_index(1)-1)) *
(Ratio_all_inelastic(1,Delta_Emax_index(1)) - Ratio_all_inelastic(1,Delta_Emax_index(1)-1)) /
(Ratio_all_inelastic(MFP_inelastic_index(1),Delta_Emax_index(1)) -
Ratio_all_inelastic(MFP_inelastic_index(1),Delta_Emax_index(1)-1));

            Delta_E = Delta_E_Emin + (Site(n).energy -
Ratio_all_inelastic(MFP_inelastic_index(1)-1,1))*(Delta_E_Emax - Delta_E_Emin) /
(Ratio_all_inelastic(MFP_inelastic_index(1),1) - Ratio_all_inelastic(MFP_inelastic_index(1)-
1,1));

        else            % E > 9kev, using the proportional data based on E =9kev
            Delta_index = find(Ratio_all_inelastic(28,3:182) > R_Delta_rand)+2;
            Delta_E_9 = Ratio_all_inelastic(1,Delta_index(1)-1) + (R_Delta_rand -
Ratio_all_inelastic(28,Delta_index(1)-1)) * (Ratio_all_inelastic(1,Delta_index(1)) -
Ratio_all_inelastic(1,Delta_index(1)-1)) / (Ratio_all_inelastic(28,Delta_index(1)) -
Ratio_all_inelastic(28,Delta_index(1)-1));
            Delta_E = Site(n).energy / 9 * Delta_E_9 ;

        end

% using delta E, we could determine polar angle for primary electrons and secondary electrons

        if   (sum(cos(Site(n).angle(:)).^2)==1)
            Arfa = Site(n).angle(1);
            Beta = Site(n).angle(2);
            Garma =Site(n).angle(3);
        else
            COSANGLE=cos(Site(n).angle);
            Angle=acos(COSANGLE./(sum(COSANGLE(:).^2)).^0.5);
            Arfa = Angle(1);
            Beta = Angle(2);
            Garma =Angle(3);
        end

        %setting polar angle here
            Thet = asin((Delta_E / Site(n).energy )^0.5);
            R_Sai = Rand_R_Sai(R_Sai_n);
            R_Sai_n = R_Sai_n + 1;
            Sai    = 2*pi*R_Sai; % using a rand number for Thai angle
```

```
            M = [sin(Thet)*cos(Sai), sin(Thet)*sin(Sai), cos(Thet)]*[sin(Arfa), -
cos(Arfa)*cos(Beta)/(cos(Beta)^2+cos(Garma)^2)^0.5,   -
cos(Arfa)*cos(Garma)/(cos(Beta)^2+cos(Garma)^2)^0.5 ; 0, cos(Garma)*sin(Arfa)+
cos(Arfa)^2*cos(Garma)/(cos(Beta)^2+cos(Garma)^2)^0.5, -cos(Beta)*sin(Arfa)-
cos(Arfa)^2*cos(Beta)/(cos(Beta)^2+cos(Garma)^2)^0.5; cos(Arfa), cos(Beta), cos(Garma)];

        %Set new angle calculation values to next Site:
            Site(n+1).angle=acos(M);

        %input site XYZ values:
            M_n = cos(Site(n).angle);
            Site(n+1).XYZ = Site(n).XYZ + M_n*Leng;

        %input site energy values
            Site(n+1).energy = Site(n).energy - Delta_E;     % elastic collision;

    end

    clear MFP_inelastic_index;
    clear MFP_elastic_index;
    clear Theta_Emin_index;
    clear Theta_Emax_index;
    clear Theta_index;
    clear Delta_Emin_index;
    clear Delta_Emax_index;
    clear Delta_index;


        if ( - S_hole/2 < Site(n+1).XYZ(1) & Site(n+1).XYZ(1) < S_hole/2 )
            X_point_new = Site(n+1).XYZ(1) + (Site(n+1).XYZ(1) -
Site(n).XYZ(1))/abs(Site(n+1).XYZ(1) - Site(n).XYZ(1))*S_hole;
            Y_point_new = Site(n+1).XYZ(2) + (Site(n+1).XYZ(2) - Site(n).XYZ(2)) /
(Site(n+1).XYZ(1) - Site(n).XYZ(1)) * ( X_point_new - Site(n+1).XYZ(1));
            Z_point_new = Site(n+1).XYZ(3) + (Site(n+1).XYZ(3) - Site(n).XYZ(3)) /
(Site(n+1).XYZ(1) - Site(n).XYZ(1)) * ( X_point_new - Site(n+1).XYZ(1));

            Site(n+1).XYZ(1) = X_point_new;
            Site(n+1).XYZ(2) = Y_point_new;
            Site(n+1).XYZ(3) = Z_point_new;
        end


        if   (Site(n+1).XYZ(3) > Z_Au   )   % track the backscattering electrons
            Site(n+1).XYZ      = Site(n).XYZ + M_n*((Z_Au -
Site(n).XYZ(3))/abs(cos(Site(n).angle(3))));
            Site(n+1).angle   = Site(n).angle;
            Site(n+1).energy = Site(n).energy;

            N_ZEP520(n_ZEP520).XYZ(1:2)      = Site(n+1).XYZ(1:2);
            N_ZEP520(n_ZEP520).XYZ(3)      = Site(n+1).XYZ(3)- Z_Au;
            N_ZEP520(n_ZEP520).energy = Site(n+1).energy;
```

```
                    N_ZEP520(n_ZEP520).angle   = Site(n+1).angle;
                    n_ZEP520 = n_ZEP520 + 1;

                    if(abs(Site(n+1).XYZ(1)) < S_hole/2)
                        N_hole_out = N_hole_out + 1;
                        Hole_out (N_hole_out).XYZ =
[Site(n+1).XYZ(1),Site(n+1).XYZ(2),Z_Au,Site(n+1).energy];
                    else
                        N_BE = N_BE + 1;
                        BESite(N_BE).energy = Site(n).energy;
                        BESite(N_BE).angle   = Site(n).angle;
                        BESite(N_BE).XYZ   = Site(n+1).XYZ;
                    end
                    break_sign = 1;
                end

        if break_sign == 1
            break
        end

         n = n + 1 ;     % in order to calculate the site number

    end

 clear Site;

clear Secondary;

end
end


fN_hole_out = Hole_out;
fN = N_ZEP520;
fBESite = BESite;
```

BIBLIOGRAPHY

[1] P. B. Meggs, *A history of graphic design*. Isbn 0-471-291-98-6 (John Wiley & Sons, Inc, 1998).

[2] C. 73. *Litography negative stone and positive paper,* (2006).

[3] N. Howard, *The life story of a technology*. Isbn 031333028x (Greenwood Publishing Group, 2005).

[4] R. C. Jaeger, *"Lithography". Introduction to microelectronic fabrication*. (Upper Saddle River: Prentice Hall, 2002).

[5] K. Jain, C. G. Willson, B. J. Lin, Ultrafast deep uv lithography with excimer lasers. *Electron Device Letters, IEEE* 3, 53-55 (1982).

[6] R. E. Resnick, R., *Quantum physics of atoms, molecules, solids, nuclei and particles* (New York: John Wiley & Sons, ed. 2nd, 1985).

[7] N. W. Parker, A. D. Brodie, J. H. Mccoy, E. A. Dobisz, Ed. (SPIE, Santa Clara, CA, USA, 2000), vol. 3997, pp. 713-720.

[8] L. R. Harriott. (AVS, 1997), vol. 15, pp. 2130-2135.

[9] R. S. Dhaliwal *et al.*, Prevail—electron projection technology approach for next-generation lithography. *IBM Journal of Research and Development* 45, 615-638 (2001).

[10] O. Shinji, Lithographic technologies for future ulsi. *Applied Surface Science* 70–71, Part 2, 603-612 (1993).

[11] K. D. Vora, B. Y. Shew, E. C. Harvey, J. P. Hayes, A. G. Peele, Sidewall slopes of su-8 harmst using deep x-ray lithography. *Journal of Micromechanics and Microengineering* 18, 035037 (2008).

[12] R. Paetzel *et al.*, Y. Anthony, Ed. (SPIE, 2003), vol. 5040, pp. 1665-1671.

[13] S. S. Harilal *et al.*, Spectral control of emissions from tin doped targets for extreme ultraviolet lithography. *Journal of Physics D: Applied Physics* 39, 484 (2006).

[14] N. Koch *et al.*, Radiation induced degradation and surface charging of organic thin films in ultraviolet photoemission spectroscopy. *Thin Solid Films* 391, 81-87 (2001).

[15] J. Hollenshead, L. Klebanoff, Modeling radiation-induced carbon contamination of extreme ultraviolet optics. *Journal of Vacuum Science & Technology B: Microelectronics and Nanometer Structures* 24, 64-82 (2006).

[16] M. H. L. V. D. Velden, W. J. M. Brok, J. J. a. M. V. D. Mullen, V. Banine, Kinetic simulation of an extreme ultraviolet radiation driven plasma near a multilayer mirror. *Journal of Applied Physics* 100, 073303 (2006).

[17] J. J. Biafore *et al.*, M. L. F. Bruno, Ed. (SPIE, 2010), vol. 7636, pp. 76360R.

[18] T. I. Wallow *et al.*, L. H. Clifford, Ed. (SPIE, 2009), vol. 7273, pp. 72733T.

[19] M. J. Wieland *et al.*, J. C. H. Daniel, Ed. (SPIE, 2010), vol. 7637, pp. 76370F.

[20] S. Y. Chou, P. R. Krauss, P. J. Renstrom, Imprint lithography with 25-nanometer resolution. *Science* 272, 85-87 (1996).

[21] M. Colburn *et al.*, A. D. Elizabeth, Ed. (SPIE, 2000), vol. 3997, pp. 453-457.

[22] E. L. Schwartz, J. K. Bosworth, M. Y. Paik, C. K. Ober, D. A. Robert, Ed. (SPIE, 2010), vol. 7639, pp. 76390G.

[23] R. Ruiz *et al.*, Density multiplication and improved lithography by directed block copolymer assembly. *Science* 321, 936-939 (2008).

[24] M. P. Stoykovich *et al.*, Directed self-assembly of block copolymers for nanolithography: Fabrication of isolated features and essential integrated circuit geometries. *ACS Nano* 1, 168-175 (2007).

[25] C. A. Mack, Trends in optical lithography. *Opt. Photon. News* 7, 29-33 (1996).

[26] M. Rothschild, Projection optical lithography. *Materials Today* 8, 18-24 (2005).

[27] R. H. French, H. V. Tran, Immersion lithography: Photomask and wafer-level materials. *Annual Review of Materials Research* 39, 93-126 (2009).

[28] P. R. Choudhury, *Handbook of microlithography, micromachining, and microfabrication*. (SPIE, Bellingham, WA, 1997), pp. Monograph PM39.

[29] R. F. Pease, S. Y. Chou, Lithography and other patterning techniques for future electronics. *Proceedings of the IEEE* 96, 248-270 (2008).

[30] A. E. A. Thompson, X-ray data booklet. (2001).

[31] E. A. Costner, M. W. Lin, W.-L. Jen, C. G. Willson, Nanoimprint lithography materials development for semiconductor device fabrication. *Annual Review of Materials Research* 39, 155-180 (2009).

[32] L. R. Harriott, Scattering with angular limitation projection electron beam lithography for suboptical lithography. *Journal of Vacuum Science & Technology B: Microelectronics and Nanometer Structures* 15, 2130-2135 (1997).

[33] Y. Lu, N. Yoshimizu, A. Lal, Self-powered near field electron lithography. *Journal of Vacuum Science & Technology B: Microelectronics and Nanometer Structures* 27, 2537-2541 (2009).

[34] Y. Lu, A. Lal, Vacuum-free self-powered parallel electron lithography with sub-35-nm resolution. *Nano Letters* 10, 2197-2201 (2010).

[35] Z. J. Ding, R. Shimizu, A monte carlo modeling of electron interaction with solids including cascade secondary electron production. *Scanning* 18, 92-113 (1996).

[36] P. Hovington, D. Drouin, R. Gauvin, D. C. Joy, N. Evans, Casino: A new monte carlo code in c language for electron beam interactions—part iii: Stopping power at low energies. *Scanning* 19, 29-35 (1997).

[37] Z. Tan *et al.*, Electron inelastic interactions in bioorganic compounds in the energy range of 20–10000 ev. *Applied Physics A: Materials Science & Processing* 81, 779-786 (2005).

[38] E. Fermi, Versuch einer theorie der β-strahlen. I. *Zeitschrift für Physik A Hadrons and Nuclei* 88, 161-177 (1934).

[39] P. Venkataramaiah, K. Gopala, A. Basavaraju, S. S. Suryanarayana, H. Sanjeeviah, A simple relation for the fermi function. *Journal of Physics G: Nuclear Physics* 11, 359 (1985).

[40] B. Hahn, D. G. Ravenhall, R. Hofstadter, High-energy electron scattering and the charge distributions of selected nuclei. *Physical Review* 101, 1131-1142 (1956).

[41] Z. Czyzewski, D. O. N. Maccallum, A. Romig, D. C. Joy, Calculations of mott scattering cross section. *Journal of Applied Physics* 68, 3066-3072 (1990).

[42] D. Drouin, P. Hovington, R. Gauvin, Casino: A new monte carlo code in c language for electron beam interactions—part ii: Tabulated values of the mott cross section. *Scanning* 19, 20-28 (1997).

[43] D. Pines, Nozi ères, P., *The theory of quantum liquids*. (New York, 1966).

[44] A. R. Brosi, C. J. Borkowski, E. E. Conn, J. C. Griess, Jr., Characteristics of ni^{59} and ni^{63}. *Physical Review* 81, 391-395 (1951).

[45] B. Budick, J. Chen, H. Lin, Half-life of molecular tritium and the axial-vector interaction in tritium β decay. *Physical Review Letters* 67, 2630-2633 (1991).

[46] L. Schlapbach, A. Zuttel, Hydrogen-storage materials for mobile applications. *Nature* 414, 353-358 (2001).

[47] B. Sakintuna, F. Lamari-Darkrim, M. Hirscher, Metal hydride materials for solid hydrogen storage: A review. *International Journal of Hydrogen Energy* 32, 1121-1140 (2007).

[48] H. Bohlen, J. Greschner, J. Keyser, W. Kulcke, P. Nehmiz, Electron-beam proximity printing: A new high-speed lithography method for submicron structures. *IBM J. Res. Dev.* 26, 568-579 (1982).

[49] G. O. H. Mallory, J. B, *Electroless plating: Fundamentals and applications*. vol. 1. (1990)

[50] 4491628 positive- and negative-working resist compositions with acid generating photoinitiator and polymer with acid labile groups pendant from polymer backbone : Hiroshi ito, carlton willson, jean m frechet assigned to international business machines corporation. *International Journal of Nuclear Medicine and Biology* 12, xxxiv (1985).

[51] D. V. Steenwinckel, J. H. Lammers, T. Koehler, R. L. Brainard, P. Trefonas, Resist effects at small pitches. *Journal of Vacuum Science & Technology B: Microelectronics and Nanometer Structures* 24, 316-320 (2006).

[52] G. Zhou, K. K. L. Cheo, Y. Du, F. S. Chau, An optically interrogated microgyroscope using an out-of-plane lamellar grating. *Sensors and Actuators A: Physical* 154, 269-274 (2009).

[53] P. Gevorkian, *Sustainable energy systems engineering: The complete green building design resource*. (McGraw-Hill Professional, 2007).

[54] Y.-F. Huang *et al.*, Improved broadband and quasi-omnidirectional anti-reflection properties with biomimetic silicon nanostructures. *Nat Nano* 2, 770-774 (2007).

[55] L. Tsakalakos *et al.*, Strong broadband optical absorption in silicon nanowire films. *Journal of Nanophotonics* 1, 013552 (2007).

[56] V. Sivakov *et al.*, Silicon nanowire-based solar cells on glass: Synthesis, optical properties, and cell parameters. *Nano Letters* 9, 1549-1554 (2009).

[57] T. Stelzner *et al.*, Silicon nanowire-based solar cells. *Nanotechnology* 19, 295203 (2008).

[58] B. Tian *et al.*, Coaxial silicon nanowires as solar cells and nanoelectronic power sources. *Nature* 449, 885-889 (2007).

[59] L. Tsakalakos *et al.*, Silicon nanowire solar cells. *Applied Physics Letters* 91, 233117 (2007).

[60] E. C. Garnett, P. Yang, Silicon nanowire radial p−n junction solar cells. *Journal of the American Chemical Society* 130, 9224-9225 (2008).

[61] E. Garnett, P. Yang, Light trapping in silicon nanowire solar cells. *Nano Letters* 10, 1082-1087 (2010).

[62] C. Lin, M. L. Povinelli, Optical absorption enhancement in silicon nanowire arrays with a large lattice constant for photovoltaic applications. *Opt. Express* 17, 19371-19381 (2009).

[63] L. Hu, G. Chen, Analysis of optical absorption in silicon nanowire arrays for photovoltaic applications. *Nano Letters* 7, 3249-3252 (2007).

[64] Z. Yu, A. Raman, S. Fan, Fundamental limit of nanophotonic light trapping in solar cells. *Proceedings of the National Academy of Sciences*, (2010).

[65] A. Chutinan, S. John, Light trapping and absorption optimization in certain thin-film photonic crystal architectures. *Physical Review A* 78, 023825 (2008).

[66] J. Zhu *et al.*, Optical absorption enhancement in amorphous silicon nanowire and nanocone arrays. *Nano Letters* 9, 279-282 (2008).

[67] Y. Lu, N. Yoshimizu, A. Lal. (AVS, 2009), vol. 27, pp. 2537-2541.

[68] E. C. Garnett *et al.*, Dopant profiling and surface analysis of silicon nanowires using capacitance-voltage measurements. *Nat Nano* 4, 311-314 (2009).

[69] J. Zhao, A. Wang, P. Altermatt, M. A. Green, Twenty-four percent efficient silicon solar cells with double layer antireflection coatings and reduced resistance loss. *Applied Physics Letters* 66, 3636-3638 (1995).

[70] Z. Fan *et al.*, Challenges and prospects of nanopillar-based solar cells. *Nano Research* 2, 829-843 (2009).

[71] S. John, Strong localization of photons in certain disordered dielectric superlattices. *Physical Review Letters* 58, 2486-2489 (1987).

[72] S. L. Diedenhofen *et al.*, Broad-band and omnidirectional antireflection coatings based on semiconductor nanorods. *Advanced Materials* 21, 973-978 (2009).

[73] Y. Kim, D. P. Neikirk, Micromachined fabry-perot cavity pressure transducer.

Photonics Technology Letters, IEEE 7, 1471-1473 (1995).

[74] G. Z. Xiao, A. Adnet, Z. Zhang, Z. Lu, C. P. Grover, Fiber-optic fabry-perot interferometric gas-pressure sensors embedded in pressure fittings. *Microwave and Optical Technology Letters* 42, 486-489 (2004).

[75] K. Ohtaka, Energy band of photons and low-energy photon diffraction. *Physical Review B* 19, 5057-5067 (1979).

[76] A. Lohfink, P. C. Eccardt, Linear and nonlinear equivalent circuit modeling of cmuts. *Ultrasonics, Ferroelectrics and Frequency Control, IEEE Transactions on* 52, 2163-2172 (2005).

[77] S. T. a. S. Woinowsky-Kreiger, *Theory of plates and shells*. (McGraw-Hill Higher Education, New York, ed. 2nd, 1964).

[78] M. Xu, L. V. Wang, Photoacoustic imaging in biomedicine. *Review of Scientific Instruments* 77, 041101 (2006).

[79] F. J. M. Harren, G. Cotti, J. Oomens, S. T. L. Hekkert, in *Encyclopedia of analytical chemistry*. (John Wiley & Sons, Ltd, 2006).

[80] B. Ilic, S. Krylov, K. Aubin, R. Reichenbach, H. G. Craighead, Optical excitation of nanoelectromechanical oscillators. *Applied Physics Letters* 86, 193114 (2005).

[81] R. P. G. Klaasse, H. Ac. Tilmans in *Proc. SeSens.*, pp. 631. (2002)

[82] Y. Lu, A. Lal, High-efficiency ordered silicon nano-conical-frustum array solar cells by self-powered parallel electron lithography. *Nano Letters* 10, 4651-4656 (2010).

[83] M. Olfatnia, T. Xu, L. S. Ong, J. M. Miao, Z. H. Wang, Investigation of residual stress and its effects on the vibrational characteristics of piezoelectric-based multilayered microdiaphragms. *Journal of Micromechanics and Microengineering* 20, 015007 (2010).

[84] M. Li, H. X. Tang, M. L. Roukes, Ultra-sensitive nems-based cantilevers for sensing, scanned probe and very high-frequency applications. *Nat Nano* 2, 114-

120 (2007).

[85] T. P. Burg *et al.*, Weighing of biomolecules, single cells and single nanoparticles in fluid. *Nature* 446, 1066-1069 (2007).

[86] J. L. Arlett, E. B. Myers, M. L. Roukes, Comparative advantages of mechanical biosensors. *Nat Nano* 6, 203-215 (2011).

[87] B. Ilic *et al.*, Enumeration of DNA molecules bound to a nanomechanical oscillator. *Nano Letters* 5, 925-929 (2005).

[88] N. V. Lavrik, P. G. Datskos, Femtogram mass detection using photothermally actuated nanomechanical resonators. *Applied Physics Letters* 82, 2697-2699 (2003).

[89] B. F. Godley *et al.*, Blue light induces mitochondrial DNA damage and free radical production in epithelial cells. *Journal of Biological Chemistry* 280, 21061-21066 (2005).

[90] J. Yang, T. Ono, M. Esashi, Surface effects and high quality factors in ultrathin single-crystal silicon cantilevers. *Applied Physics Letters* 77, 3860-3862 (2000).

[91] S. S. Verbridge, D. F. Shapiro, H. G. Craighead, J. M. Parpia, Macroscopic tuning of nanomechanics: Substrate bending for reversible control of frequency and quality factor of nanostring resonators. *Nano Letters* 7, 1728-1735 (2007).

[92] T. M. Herne, M. J. Tarlov, Characterization of DNA probes immobilized on gold surfaces. *Journal of the American Chemical Society* 119, 8916-8920 (1997).

[93] D. M. H. Cameron, *Good vibrations: Vibrating circular membrane and bessel functions*. (2000).

[94] K. L. Ekinci, Y. T. Yang, M. L. Roukes, Ultimate limits to inertial mass sensing based upon nanoelectromechanical systems. *Journal of Applied Physics* 95, 2682-2689 (2004).

[95] K. A. Marx, Quartz crystal microbalance: A useful tool for studying thin polymer films and complex biomolecular systems at the solution−surface interface.

Biomacromolecules 4, 1099-1120 (2003/09/01, 2003).

[96] I. Kozinsky, H. W. C. Postma, O. Kogan, A. Husain, M. L. Roukes, Basins of attraction of a nonlinear nanomechanical resonator. *Physical Review Letters* 99, 207201 (2007).

[97] I. Kozinsky, H. W. C. Postma, I. Bargatin, M. L. Roukes, Tuning nonlinearity, dynamic range, and frequency of nanomechanical resonators. *Applied Physics Letters* 88, 253101 (2006).

[98] S. N. Cha *et al.*, Fabrication of a nanoelectromechanical switch using a suspended carbon nanotube. *Applied Physics Letters* 86, 083105 (2005).

[99] J. S. Aldridge, A. N. Cleland, Noise-enabled precision measurements of a duffing nanomechanical resonator. *Physical Review Letters* 94, 156403 (2005).

[100] E. Buks, B. Yurke, Mass detection with a nonlinear nanomechanical resonator. *Physical Review E* 74, 046619 (2006).

[101] S. H. Kellert, *In the wake of chaos: Unpredictable order in dynamical systems*. (University of Chicago Press, 1993).

[102] J.-J. Lou, S.-J. Zhu, L. He, X. Yu, Application of chaos method to line spectra reduction. *Journal of Sound and Vibration* 286, 645-652 (2005).

[103] S. W. Yoon, S. Lee, N. C. Perkins, K. Najafi, Analysis and wafer-level design of a high-order silicon vibration isolator for resonating mems devices. *Journal of Micromechanics and Microengineering* 21, 015017 (2011).

[104] S. W.-K. S. P. Timoshenko, *Theory of plates and shells*. (New York: McGraw-Hill, 1959).

[105] M. Olfatnia, V. R. Singh, T. Xu, J. M. Miao, L. S. Ong, Analysis of the vibration modes of piezoelectric circular microdiaphragms. *Journal of Micromechanics and Microengineering* 20, 085013 (2010).

[106] C. Touzé, O. Thomas, M. Amabili, Transition to chaotic vibrations for harmonically forced perfect and imperfect circular plates. *International Journal of*

Non-Linear Mechanics 46, 234-246 (2011).

[107] A. Sharma, V. Patidar, G. Purohit, K. K. Sud, Effects on the bifurcation and chaos in forced duffing oscillator due to nonlinear damping. *Communications in Nonlinear Science and Numerical Simulation* 17, 2254-2269 (2012).

[108] J. P. Owen, W. S. Ryu, The effects of linear and quadratic drag on falling spheres: An undergraduate laboratory. *European Journal of Physics* 26, 1085 (2005).

[109] C. Touzé, S. Bilbao, O. Cadot, Transition scenario to turbulence in thin vibrating plates. *Journal of Sound and Vibration* 331, 412-433 (2012).

[110] J. S. Mitchell, K. Najafi, in *Solid-State Sensors, Actuators and Microsystems Conference, 2009. TRANSDUCERS 2009. International*. (2009), pp. 841-844.

[111] S. H. Lee *et al.*, in *Micro Electro Mechanical Systems, 2009. MEMS 2009. IEEE 22nd International Conference on*. (2009), pp. 753-756.

[112] C. Junseok, J. M. Giachino, K. Najafi, Fabrication and characterization of a wafer-level mems vacuum package with vertical feedthroughs. *Microelectromechanical Systems, Journal of* 17, 193-200 (2008).

[113] R. N. Candler *et al.*, Long-term and accelerated life testing of a novel single-wafer vacuum encapsulation for mems resonators. *Microelectromechanical Systems, Journal of* 15, 1446-1456 (2006).

[114] R. Duggirala, H. Li, A. Lal, High efficiency beta radioisotope energy conversion using reciprocating electromechanical converters with integrated betavoltaics. *Applied Physics Letters* 92, 154104 (2008).

[115] M. V. S. Chandrashekhar, R. Duggirala, M. G. Spencer, A. Lal, 4h sic betavoltaic powered temperature transducer. *Applied Physics Letters* 91, 053511 (2007).

[116] M. V. S. Chandrashekhar, C. I. Thomas, H. Li, M. G. Spencer, A. Lal, Demonstration of a 4h sic betavoltaic cell. *Applied Physics Letters* 88, 033506 (2006).

[117] H. Cember, *Introduction to health physics*. (Pergamon, New York, 1983).

[118] H. V. Klapdor, J. Metzinger, T. Oda, Beta decay half lives of nuclei far from stability. *Zeitschrift für Physik A Hadrons and Nuclei* 309, 91-92 (1982).

[119] Y. Yang, L. Qian, J. Tang, L. Liu, S. Fan, A low-vacuum ionization gauge with hfc-modified carbon nanotube field emitters. *Applied Physics Letters* 92, 153105 (2008).

[120] A. K. Wong, *Resolution enhancement techniques in optical lithography*. (SPIE Alfred Kwok-Kit, 2001).

[121] G. Palasantzas, J. T. M. Dehosson, Surface roughness influence on the pull-in voltage of microswitches in presence of thermal and quantum vacuum fluctuations. *Surface Science* 600, 1450-1455 (2006).